Design of Cardiac Valve Scaffolds from Various Polymeric Biomaterials and Assessment of Dynamic Performance

by

Drake Dalton Pedersen

Bachelor of Science, University of Pittsburgh, 2015

Submitted to the Graduate Faculty of the

Swanson School of Engineering in partial fulfillment

of the requirements for the degree of

Doctor of Philosophy

University of Pittsburgh

2023

UNIVERSITY OF PITTSBURGH

SWANSON SCHOOL OF ENGINEERING

This dissertation was presented

by

Drake Dalton Pedersen

It was defended on

October 5, 2023

and approved by

Antonio D'Amore, PhD
Associate Professor, Departments of Surgery and Bioengineering, University of Pittsburgh

Harvey Borovetz, PhD
Distinguished Professor, Department of Bioengineering; Robert L. Hardesty Professor, Department of Surgery; Professor, Department of Chemical and Petroleum Engineering, Clinical Translational Science Institute; Deputy Director of Artificial Organs and Medical Devices, McGowan Institute for Regenerative Medicine, University of Pittsburgh

Steven Abramowitch, PhD
W.K. Whiteford Professor, Department of Bioengineering; Professor, Clinical Translational Science Institute, University of Pittsburgh

Jacqueline Kreutzer, MD, FACC, FSCAI
Endowed Chair, Pediatric Cardiology, University of Pittsburgh Medical Center; Co-Director, Heart Institute, University of Pittsburgh Medical Center Children's Hospital of Pittsburgh; Professor, Department of Pediatrics, School of Medicine, University of Pittsburgh

Dissertation Director: William R. Wagner, PhD
Distinguished Professor, Departments of Surgery, Chemical Engineering, and Bioengineering

Design of Cardiac Valve Scaffolds from Various Polymeric Biomaterials and Assessment of Dynamic Performance

Drake Dalton Pedersen, PhD

University of Pittsburgh, 2023

Cardiac valve replacement has a long history of clinical practice, yet to this day that practice is marred by suboptimal outcomes and has become a sequence of palliative measures. At the same time, the advent of tissue engineering as a concept to restore native tissue function through cell repopulation of degradable scaffolds has caused a paradigm shift in approach to cardiac valve engineering, particularly for growing valves in young patients. However, applying tissue engineering principles to the cardiac valves has not been straightforward. From the earliest attempts until even recent clinical trials of these tissue engineered heart valves, a great deal has remained unknown, such as biological mechanisms of cell infiltration and neotissue formation as well as optimal valve design considerations for recreating native-like mechanical deformation and dynamic functional performance.

Therefore, it was the objective of this dissertation to further elucidate some of these unknowns, namely the material properties and geometry and their influence over structural and fluid mechanics. Additionally, comparing the functional performance of valve scaffolds sized for both adults and children was a crucial component. The experimental efforts reported herein identified two key design parameters, namely material stiffness and valve geometry, that could be modified toward optimization of valve scaffolds. Among the two primary variables tested here, the geometric configuration played a relatively more significant role than material stiffness in determining valve function and mechanical properties. Specifically, while valve performance generally diminished with increasing stiffness, extending the free edge length proved to be a

significantly greater modification, contributing to a significant reduction in strain concentrations throughout the leaflet surface as well as reduced fluid jet velocity. Additionally, the electrospinning process used to fabricate valve scaffolds was tuned to allow for tightly controlled polymer deposition patterns in both adult- and pediatric-scale scaffolds. Future study may use this research as groundwork for iteration on valve design coupling experimental validation to computational modeling, as well as optimizing additional design features to improve both mechanical and host responses to degradable valve scaffolds on the road towards clinical translation.

Table of Contents

1.0 Introduction 1

1.1 Significance 1

1.2 Past and Current Treatment Strategies 3

1.2.1 Mechanical Valves 3

1.2.2 Bioprosthetic Valves 5

1.2.3 Transcatheter Valves 7

1.2.4 Polymeric Valves 9

1.3 Tissue Engineered Heart Valves 11

1.3.1 Material Selection 11

1.3.2 Polymer Processing 13

1.3.3 Structural Mechanics of Heart Valve Scaffolds 17

1.3.4 Fluid Mechanics of Heart Valve Scaffolds 19

1.3.5 Cell Source & Tissue Growth 21

1.3.6 Current Preclinical Models and Translational Potential 25

1.4 Pediatric Valve Replacement 27

1.4.1 Congenital Defects Afflicting the Cardiac Valves 27

1.4.2 Specific Challenges of the Pediatric Population 30

1.4.3 Pediatric Cardiac Valve Scaffold Development 32

1.5 Objectives 37

1.5.1 Objective 1 – Interrogate the Influence of Polymer Stiffness and Geometric Design on Structural Mechanics in Tissue Engineered Pulmonary Valve Scaffolds 38

1.5.2 Objective 2 – Interrogate the Influence of Polymer Stiffness and Geometric Design on Fluid Mechanics in Tissue Engineered Pulmonary Valve Scaffolds 38

1.5.3 Objective 3 – Strategy for Miniaturization of Valve Scaffold Design for Pediatric Use 39

2.0 Cardiac Valve Scaffold Design: Implications of Material Properties and Geometric Configuration on Performance and Mechanics 40

2.1 Introduction 40

2.2 Materials and Methods 42

2.2.1 Cardiac Valve Scaffold Design 42

2.2.2 Polymer Processing and Scaffold Fabrication 42

2.2.3 Scaffold Material Properties 43

2.2.4 Mock Circulatory Loop 44

2.2.5 Dynamic Strain Mapping 46

***2.2.5.1 Image Acquisition* 46**

***2.2.5.2 3D Image Correlation* 47**

***2.2.5.3 Strain Calculation* 48**

2.2.6 Statistical Analysis 48

2.3 Results 49

2.3.1 Valve Scaffold Characterization 49

***2.3.1.1 Electrospun Valve Scaffold Designs* 49**

2.3.1.2 Valve Scaffold Thickness 49

2.3.1.3 Polymer Microstructure 49

2.3.1.4 Mechanical Characterization 50

2.3.2 Valve Scaffold Pulmonary Performance 52

2.3.3 Strain Mapping 54

2.3.3.1 Overall Mean Strain 54

2.3.3.2 Regional Mean Strain – Stiffness Effect 55

2.3.3.3 Regional Mean Strain – Geometric Effect 58

2.4 Discussion 60

2.5 Conclusions 66

3.0 Influence of Polymer Stiffness and Cardiac Valve Geometry on Fluid Mechanics in Tissue Engineered Pulmonary Valve Scaffold 67

3.1 Introduction 67

3.2 Materials and Methods 68

3.2.1 Valve Scaffold Design and Fabrication 68

3.2.2 Mock Circulatory Loop 70

3.2.3 Particle Image Velocimetry 72

3.2.4 Statistical Analysis 75

3.3 Results 75

3.3.1 Scaffold Fabrication 75

3.3.2 Valve Scaffold Functional Performance 76

3.3.3 Flow Visualization 78

3.4 Discussion 85

3.5 Conclusions 90

4.0 Strategy for Miniaturization of Valve Scaffold Design for Pediatric Use 91

4.1 Introduction 91

4.2 Materials and Methods 93

4.2.1 Pediatric Valve Scaffold Design and Fabrication 93

4.2.2 Scaffold Microstructure and Mechanics 95

4.2.3 Pediatric Valve Scaffold Functional Performance 95

4.2.4 Statistical Analysis 96

4.3 Results 96

4.3.1 Scaffold Properties 96

4.3.2 Scaffold Mechanics 97

4.3.3 Pediatric Pulmonary Valve Scaffold Performance 98

4.4 Discussion 99

4.5 Limitations 102

4.6 Conclusions 103

5.0 Continued Research and Future Directions 104

5.1 Design Optimization of Cardiac Valve Scaffolds 104

5.1.1 Computational Modeling of Cardiac Valve Performance 104

5.1.2 Material Thickness 108

5.1.3 Microstructural and Mechanical Biomimicry 109

5.2 Calcification Mitigation Strategies 111

5.3 Implementation of Fully-Degradable Stented Valve Scaffold for Transcatheter Delivery 113

5.4 Endogenous Tissue Growth *In-Vivo* 114

6.0 Final Conclusions 116

Appendix A *In Vivo* Assessment of Stented, Degradable Polymeric Valves in an Ovine Model 121

Appendix A.1 Introduction 121

Appendix A.2 Materials and Methods 122

Appendix A.2.1 Polymer Valve Scaffold Preparation 122

Appendix A.2.2 Surgical Pulmonary Valve Replacement in an Ovine Model 123

Appendix A.2.3 Explant Analysis 124

Appendix A.3 Results 125

Appendix A.3.1 Ovine Pulmonary Valve Replacement Model 125

Appendix A.3.2 Gross Morphological Assessment, 30-day Explants 126

Appendix A.3.3 Gross Morphological Assessment, 90-day Explants 127

Appendix A.3.4 Histological Assessment, 30-day Explants 128

Appendix A.3.5 Histological Assessment, 90-day Explants 130

Appendix A.4 Discussion 132

Bibliography 136

List of Tables

Table 4-1. Fabrication Parameters for Pediatric Valve Scaffolds..... 94

Table 4-2. Fabrication Parameters for Adult Valve Scaffolds 94

List of Figures

Figure 1-1. Representative evolution of mechanical heart valve design. 3

Figure 1-2. Representative evolution in bioprosthetic heart valve design. 6

Figure 1-3. Example of a transcatheter aortic valve replacement..... 8

Figure 1-4. Development of biostable polymer valve replacements. 11

Figure 1-5. Typical electrospinning setup for producing degradable valve scaffolds. 14

Figure 1-6. Variation of electrospinning parameters demonstrates tunability in porous microfiber network. 16

Figure 1-7. Various approaches to tissue engineering heart valve scaffolds. 21

Figure 1-8. Valve scaffold regeneration schematic. 23

Figure 1-9. Congenital heart defects requiring valve replacement. 29

Figure 1-10. Acellular, polymeric pediatric pulmonary valved conduit. 34

Figure 1-11. Decellularized ECM-based pediatric pulmonary valved conduit. 35

Figure 2-1. Geometric configurations of double-component deposition electrospinning collectors 41

Figure 2-2. Schematic of mock circulatory loop 45

Figure 2-3. Schematic of stereoscopic camera setup..... 47

Figure 2-4. Mechanical data..... 51

Figure 2-5. Valve performance for all four PCUU/PCL blends and both geometric configurations. 52

Figure 2-6. Averaged strain maps during peak systole for Mk1 valve scaffold geometry (n=5/group). 53

Figure 2-7. Averaged strain maps during peak systole for Mk2 valve scaffold geometry (n=5/group). 54

Figure 2-8. Averaged strain maps during diastole for Mk1 valve scaffold geometry (n=5/group). 56

Figure 2-9. Averaged strain maps during diastole for Mk2 valve scaffold geometry (n=5/group). 57

Figure 2-10. Still images of valve scaffolds from all PCUU/PCL blends 59

Figure 3-1. Multi-phase electrospinning fabrication. 69

Figure 3-2. Particle image velocimetry experimental setup. 72

Figure 3-3. Representative image of a velocity field 73

Figure 3-4. Figure 4. Valve scaffold mock circulatory loop performance metrics. 77

Figure 3-5. Velocity field metrics from particle image velocimetry results at peak systole for Mark 1 (Mk1) and Mark 2 (Mk2) valve scaffold geometric designs. 79

Figure 3-6. Velocity magnitudes from particle image velocimetry timepoints ranging from 125 ms before peak systole to 125 ms after peak systole. 81

Figure 3-7. Representative averaged velocity magnitudes at peak systole. 82

Figure 3-8. Representative averaged viscous shear stress at peak systole. 83

Figure 3-9. Representative averaged vorticity at peak systole. 84

Figure 3-10. Representative averaged turbulent kinetic energy at peak systole 85

Figure 3-11. Representative averaged Reynolds shear stress at peak systole. 85

Figure 4-1. Adult and pediatric valve comparison. 94

Figure 4-2. Adult vs. pediatric scaffold characterization. 97

Figure 4-3. Functional performance of pediatric valve scaffolds. 99

Figure 5-1. Micro-scale topographical definition of heart valve mandrel. 111

Appendix Figure 1. Pre-Implant and intraoperative photos of stented valve scaffold. 124

Appendix Figure 2. 30-day valve scaffold explants..... 127

Appendix Figure 3. 90-day valve scaffold explants..... 128

Appendix Figure 4. Histology of tissue overgrowth in 120 µm valve explant. 129

Appendix Figure 5. Histological assessment of 30-day 240 µm valve explant..... 130

Appendix Figure 6. Histological assessment of 90-day 120 µm valve explants. 131

Appendix Figure 7. Histological assessment of 90-day 240 µm valve explants. 132

Preface

As I reflect on the completion of the work that would become this dissertation, I often perceived it to be a Sisyphean task, with repetitious failure marking the first several years of experimental effort. Neither was there a breaking of the log jam with a flood of data streaming forth. Instead, progress was made in a drawn-out series of small successes that led to several iterations of valve fabrication and data collection, each round improved upon the last. Despite my wishes to the contrary, however, the experience and expertise I gained over the last several years, I believe, has improved my skills as a scientist, engineer, researcher, and writer beyond what would have been possible without the difficulty of these tasks. So, in an ironic way, I am grateful to the challenges this work has posed, and I am more prepared for the many challenges that will come next.

There were certainly a great many people to whom I am indebted for their scientific and professional support over these years. The first mention has to be my advisor, Dr. William R. Wagner. It was, in fact, his mentorship that helped me to confront the many challenges faced, offering advice but allowing me also to contribute to the solutions independently, and which I credit as having advanced my skillset as a researcher and engineer. In near equal measure is the mentorship of Dr. Antonio D'Amore, without whose incredibly deep knowledge on any valve or mechanics related question I would have been even longer in completing this dissertation. The remaining members of my committee, Dr. Harvey Borovetz, Dr. Steven Abramowitch, and Dr. Jaqueline Kreutzer, have each contributed to this work in a variety of ways. From Dr. Kreutzer providing insight on pediatric valve dimensions and physiological parameters to Dr. Abramowitch directing me to use FEBio Studio (a program I likely would never have found on my own and

saved many hours of programming in Matlab) to Dr. Borovetz offering advice on particle image velocimetry. There were also several colleagues who aided in accomplishing this work. Seungil Kim is perhaps the most important, devoting many hours of synthesizing polymer for me, without which none of my experiments would have been possible. Francesco Madonia stands out as a highly competent assistant in initially developing the strain mapping protocol. Ben Leslie, of all the undergraduate students I have trained, was the most dedicated, and helped with many of the valve fabrications used in these experiments. I also have to express deep gratitude to the machinists—Brian Frankowski and Dan McKeel—who not only built all of the devices I designed for actually executing these experiments, but also helped me become a better engineer by changing my perspective on how to actually design parts.

The list of personal connections who have supported me for these past several years is long, and to write each of them an anecdote would be to write a second dissertation. So, to my friends, in particular all those who have PhD's and have been through this process, there are so many instances where your support and encouragement have helped me. I would, however, like to extend a special thanks to Grayson Bourne, Derek Bates, Ken Hovis, and Andrew Stockdale for your pastoral support and mentorship. To my parents, Mom and Dad, your unwavering support has always been appreciated especially in moments of frustration, even though I never tell you enough.

To my wife, Megan Pedersen, you have weathered this storm with me, through every episode of frustration and despair at the seemingly never-ending train of failures and shortcomings. You have been beside me through all of it, enduring patiently until this moment. I hope and pray that in the years looking forward I will be able to repay your kindness and grace for the undying support you have for me and my ambitions. Even in the midst of this journey, we have welcomed two wonderful children, Lucy and Martin, into this world. I hope to be able to provide for all of

you, now and always, in every way like I promised I would. This entire work is dedicated to the three of you.

As a final note of reflection, I stand humbled by the ability to say that I have finally completed this task. From the beginning of this process until now, my faith in Jesus Christ has been the foundation and bulwark of my soul. I have seen Him at work in many ways in my life through this process, growing me to be more humble, patient, and self-controlled. I want to thank everyone who lifted up prayers on my behalf. This arduous process has been a tool of His kindness and mercy. “I have learned the secret of facing plenty and hunger, abundance and need. I can do all things through Him who strengthens me.” (Phil. 4:12-13).

1.0 Introduction

1.1 Significance

Valvular heart disease (VHD) encompasses several pathophysiologies that may be either congenital or acquired. Valve replacement procedures affect approximately 130,000 patients per year in the United States alone [1]. Replacements of the aortic valve represent the vast majority of all replacement procedures conducted at about 83%, with transcatheter aortic valve replacement (TAVR) comprising more than half of those. Mitral valve replacements make up about 13%, while tricuspid and pulmonary valves make up the remainder. In most cases, VHD of the valves on the left side of the heart occur in patients greater than 50 years of age for acquired, degenerative VHD, while right-sided VHD, especially of the pulmonary valve, typically occur in childhood or adolescence [2].

Development of valve replacement therapies has been an ongoing pursuit since the 1950's with the early pioneering work of Charles Hufnagel, Alain Carpentier, Albert Starr, and Lowell Edwards. Modern options for valve replacement comprise four broad categories: biological grafts, mechanical, bioprosthetic, and polymeric. The designs and materials of mechanical heart valves (MHVs) have changed dramatically since the 1950's, but most contemporary mechanical valves utilize a bileaflet structure and are fabricated from pyrolytic carbon. Biological heart valve replacements have been sourced from a wide variety of tissues and species. From the initial xenotransplantation of porcine valves, sophisticated strategies have been developed of decellularization and cryopreservation of allografts and xenografts and calcification-mitigating fixation therapies for bovine pericardial bioprosthetic heart valves (BHVs), extending most

recently to minimally-invasive transcatheter technology. Polymer valves have an unfortunately troubled clinical history, but ongoing benchtop and preclinical study of new polymer formulations has led to a resurgence of these valves, some of which are currently in clinical trials. The relative usage of each type of prosthesis has shifted over the past two decades to heavily favor BHVs, which now account for >80% of all valve replacements [3]. This number includes the dramatic rise of transcatheter valve replacements which, since their approval for low- and medium-risk patients by the U.S. Food and Drug Administration (FDA) [4], [5], are now the single largest category of valve replacement [6].

The drawbacks of MHVs and BHVs are well-documented and appropriate selection of valve replacement for optimal patient outcome is a balancing act of patient-specific considerations, leading to professional debate [7]–[10], as well as clinical practice guidelines by the American College of Cardiologists/American Heart Association [11]. One drawback for all current types of valve replacements is their shared inability to grow with the patient and respond to the dynamic biological environment of native cardiovascular tissue. This has generated motivation for several research groups to apply principles of tissue engineering to valve replacement. These tissue engineered heart valves (TEHVs) vary broadly in their design and fabrication, but the common approach is to implement an artificially-produced scaffold that will promote endogenous tissue growth and restoration with the overall goal of producing valves comprised of native tissue, mitigating sequelae and the need for secondary treatments.

1.2 Past and Current Treatment Strategies

1.2.1 Mechanical Valves

The introduction of the Hufnagel caged ball valve in 1952 represented the first successful clinical implementation at replacing diseased heart valves [12]. Since then, MHVs have taken on quite a broad array of different designs and materials (Figure 1-1), but most contemporary mechanical valves utilize a bileaflet structure and are fabricated mainly from pyrolytic carbon [13]. The principal benefit of MHVs is their longevity. Being constructed from durable artificial materials, MHVs rarely fail due to loss of mechanical integrity. Instead, the main limitation of MHVs are flow patterns that significantly deviate from anatomically-inspired valves and generate blood trauma.

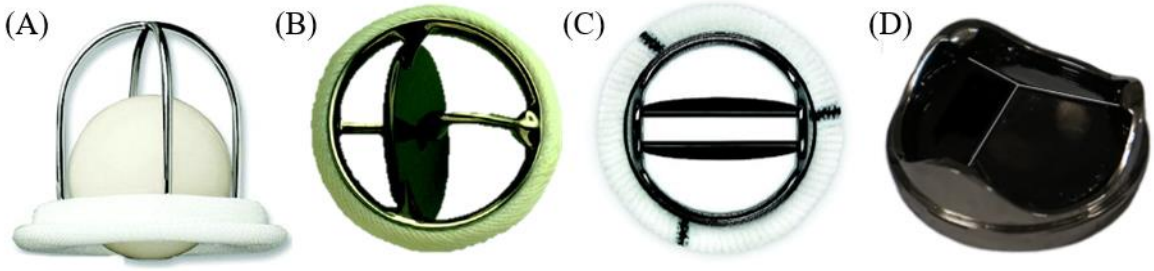

Figure 1-1. Representative evolution of mechanical heart valve design. (A) Starr-Edwards caged ball valve, (B) Medtronic Hall monoleaflet valve, (C) St. Jude bileaflet valve, (D) Triflo experimental trileaflet valve. (A)-(C) Adapted from Pibarot et al. [7] with permission from Wolters Kluwer Health Inc. (D) Reproduced from Li et al. [14] with permission from the American Society of Mechanical Engineers (ASME).

Flow fields surrounding bileaflet valves in the aortic position have been thoroughly characterized through computational methods and experimental validation, specifically with the goal of elucidating the mechanisms underlying platelet activation and hemolysis. The analysis of the mechanisms within these flow fields that create an environment favorable to platelet activation and aggregation is complex, but vortex shedding from the tips of the leaflets during systole as well as leakage flow during diastole have been identified as regions able to produce high enough shear stress and exposure time to initiate platelet activation and promote aggregation [15]–[18]. Clinically, this is counteracted through secondary treatment with an anticoagulant regimen, which in turn produces a risk of bleeding [7].

Selection of MHV over BHV is generally recommended for patients under 50 years of age, according to the ACC/AHA guideline [11]. This is the population which is assumed to be most capable of tolerating anticoagulation therapy and is most at-risk for requiring reintervention due to BHV deterioration. While outcomes with MHVs depend on anticoagulation therapy, progressive iterations on the bileaflet design are currently seeking to decrease this dependence [19]. Specifically, the On-X® MHV (Artivion, Inc., Kennesaw, GA, USA) has made minor changes to the bileaflet design with the intent of significantly reducing thromboembolic events compared to the widely used St. Jude Medical™ MHV. At 5-years follow-up, the researchers found similar rates of thromboembolic events between both MHVs. Taking a new approach, the Triflo valve (Novostia SA, Epalinges, Switzerland) implements a trileaflet MHV design with leaflets fabricated from pyrolytic carbon. *In vitro* study of the Triflo valve demonstrated a flow profile of the systolic jet more closely aligned with that of the native valve compared to a typical bileaflet design [14]. Preclinical study of the most up-to-date Triflo design has not yet been published, but initial results

have been presented at a conference that demonstrate successful implantation in the aortic and pulmonary valve positions with no anticoagulation therapy necessary [20].

1.2.2 Bioprosthetic Valves

The advent of BHVs came shortly after MHVs, beginning in 1965 with the pioneering of porcine xenotransplanted aortic valves by the team of Alain Carpentier [21]. Over the past 60 years, there have not been many modifications to the overall design of BHVs. Modifications have included variations in geometric profile of valve leaflets, tissue source, biological fixation treatments, and stented vs. stentless valves (Figure 1-2). The most significant development of BHV technology has been the advent of transcatheter valves mounted on wire stents which are implanted in minimally-invasive procedures. This specific category will be discussed in its own section below. Most surgically-placed BHVs implanted today are sourced from bovine pericardial tissue and mounted on a three-pronged stent, giving it a trileaflet structure. While their trileaflet design gives BHVs the advantages of a physiological flow profile, the main drawback is structural valve deterioration (SVD) that necessitates reoperation. While ACC/AHA guidelines recommend BHVs for patients 65 and older [11], the desire to avoid anticoagulation therapy and the increasing simplicity of reoperations with the advent of transcatheter procedures, has led to an increase in implantations in younger populations. This despite long-standing knowledge that BHV durability is inversely correlated with age at implantation. For patients under the age of 60 receiving the industry-leading BHV, freedom from SVD or reoperation ranged between 38% and 55% at 20-year follow-up [22], [23].

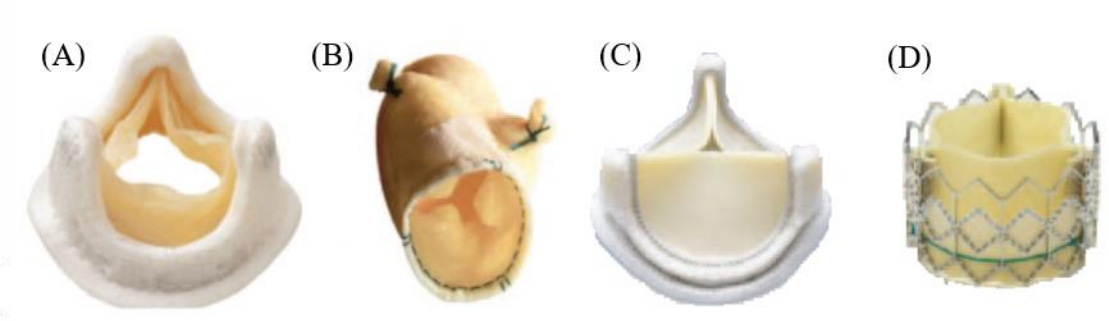

Figure 1-2. Representative evolution in bioprosthetic heart valve design. (A) Medtronic Mosaic stented porcine valve, (B) Medtronic Freestyle stentless porcine heart valve, (C) Edwards MagnaEase stented bovine pericardial heart valve, (D) Edwards Sapien stented bovine pericardial transcatheter heart valve. Adapted from Pibarot et al. [7] with permission from Wolters Kluwer Health, Inc.

Implanting biological tissues treated with chemical cross-linking agents such as glutaraldehyde was initially demonstrated to improve surgical outcomes by suppressing native immune response to xenograft valves [24], and has become the preferred method of xenogeneic tissue processing for BHV manufacturers. However, it has been repeatedly demonstrated that collagen cross-linking using glutaraldehyde leads to SVD and failure of BHVs through a complex array of proposed mechanisms centering on a biological incapacity to repair or alter the chemically fixed cellular and extracellular structures [25], [26]. The main pathway is thought to derive from the non-homeostatic valvular interstitial cells (VICs) of the xenograft, the phospholipid membranes of which may serve as a nidus for hydroxyapatite-like crystal formation with circulating calcium. Additionally, calcium mineralization seems to initiate in regions of high stress, possibly due to the permanently altered mechanical properties of the cross-linked collagen network [27]–[29].

More recent efforts to improve longevity of BHVs have taken several pathways including limiting residual phosphate and aldehyde groups by covalent-bonding [30], [31], and removing

specific antigens, principally galactose-α1,3-galactose, thought to be responsible for favored targeting by immune cells to propagate calcification [32]. Some of these strategies are newer, meaning clinical data at timepoints relevant for SVD are not yet available, but early-stage preclinical tests have demonstrated promising results [33]–[35]. Despite the substantial ongoing research efforts to identify all causes of SVD and calcification-related failure and develop mitigation strategies aimed at improving longevity of BHVs, replacement of natural valves with xenografts will continue to present challenges, and there is reasonable doubt as to whether such treatments will ever achieve a status as the ideal scaffold [36].

1.2.3 Transcatheter Valves

The increasing popularity of transcatheter valve replacements (TVRs) has made them the single largest category for all valve replacements, accounting for about 73,000 TAVRs in 2019 alone [6]. By contrast, TVRs for the other three cardiac valves are far lower in number. Transcatheter pulmonary valve replacement (TPVR) procedures, according to one meta-analysis, were performed just over 1,000 times in a 10-year period between 2007-2017 [37]. While no treatment options are currently FDA-approved for transcatheter tricuspid valve replacement (TTVR), several devices have demonstrated early feasibility and safety, and have been used in a handful of cases, typically as compassionate use [38]. Likewise, no valve prosthesis is currently FDA-approved for use in transcatheter mitral valve replacement (TMVR), and uptake of TMVR has been particularly slow despite the high number of cases of mitral regurgitation warranting intervention. This is attributed to the technical difficulty of accessing and placing a prosthetic mitral valve, as well as the relatively good outcomes of mitral valve repair as opposed to replacement [39].

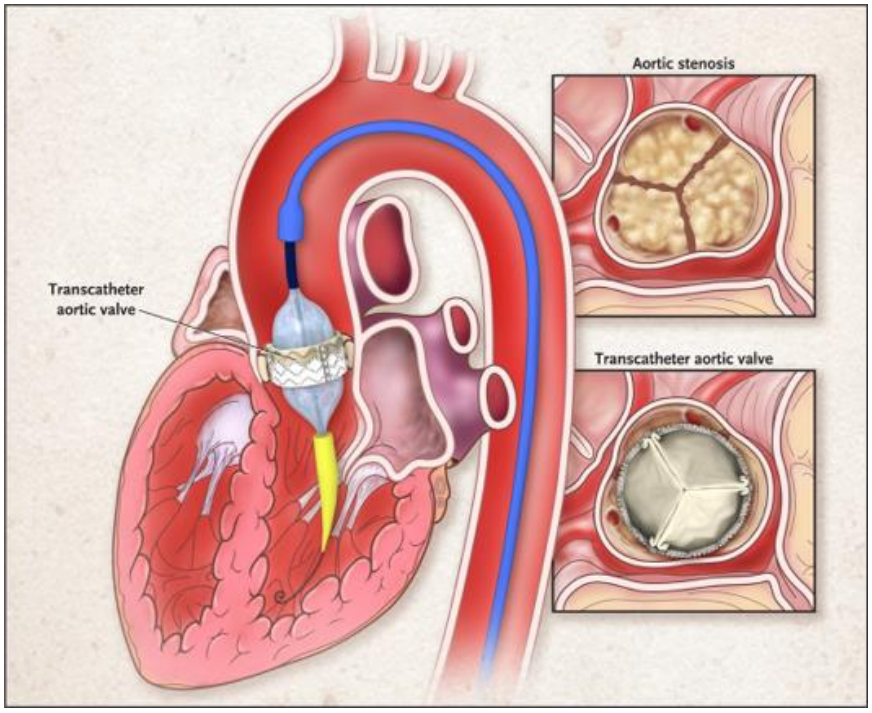

Figure 1-3. Example of a transcatheter aortic valve replacement. Stented valves are mounted on collapsible stents, crimped down to fit into a catheter, and delivered to the site of the diseased aortic valve (most often through the femoral artery). Valves are expanded either by balloon or radial force of the stent. Reproduced with permission from [40], Copyright Massachusetts Medical Society.

The main benefit of TVRs derives from their minimally-invasive implantation (Figure 1-3), allowing patients to circumvent a highly-invasive open surgical procedure. Younger patients who would typically have been directed towards MHVs have increasingly opted for BHVs despite the prospect of BHV failure and reintervention 15-20 years post-implantation, at which time they may be at an advanced age that would categorize them as too high-risk for an invasive procedure. The advent of minimally-invasive TVR implantation has led to the possibility of replacement of a failed BHV in patients who would naturally have a higher surgical risk profile, in a procedure known as valve-in-valve (ViV) implantation. Clinical data between ViV-TVR and traditional

surgical valve replacement (SVR) for failed BHV reintervention are difficult to compare given the typical use of TVR in higher risk patients as opposed to SVR for lower risk patients, but there seems to be a significant reduction in early mortality in ViV-TVR procedures [41]. While there is still a lack of long-term data comparing outcomes of ViV-TVR to SVR, it is clear that ViV-TVR will be an important procedure as BHV usage and TVR technology rapidly accelerate.

1.2.4 Polymeric Valves

When biostable polymers were first used as synthetic valve replacements in the 1960s, it was thought that they might overcome the issues of durability with BHVs while still providing the benefit of non-thrombogenicity. Unfortunately, it was discovered early on that polymers intended to remain durable quickly deteriorated and caused substantial clinical complication. This phenomenon launched a major effort into understanding the mechanisms of biological interaction with these polymers, which has been thoroughly reviewed elsewhere [42]. While there are currently no biostable polymeric valves that are widely used as valve replacements, they do have a relevant history of clinical use and are currently experiencing a resurgence of research and development. Clinical use of durable polymeric valves is limited to only a handful of materials including silicone, poly(tetrafluoroethylene) (PTFE), and polyurethane. Early results in humans with PTFE valves saw high rates of complications such as leaflet stiffening, tearing, and calcification [43]. Early research of polyurethane valve replacements in humans has only documented a couple of cases, in which one of the patients survived at least 2 months [44]. Later *in vitro* study of polyurethane valves and preclinical research using ovine and bovine models demonstrated the formation of cracks and calcification [45]–[47]. Evidence of calcification in these early studies led to a preference of BHVs over trileaflet valves fabricated from artificial materials.

Thereafter, this resulted in clinical use of polymer valves being mainly limited to ventricular assist devices for temporary mechanical circulatory support.

However, a handful of research groups have continued polymer valve development by taking advantage of technological advancements in polymer chemistry and processing, attempting to create newer generations of durable polymer valves that can resist mechanical failure, degradation, and calcification. Specifically, much of the development has focused on chemical modification of the polyether-based soft segment polyurethanes traditionally used for valve fabrication. It was discovered that polyether-based polyurethanes resulted in cracking and calcification from hydrolytic and oxidative stress at higher rates than polyurethanes based on polycarbonate [48] or polydimethylsiloxane [49] soft segments. Alternatively, pendant chemistry modifications, such as polyhedral oligomeric silsesquioxane nanocomposites, have been added to polycarbonate-based polyurethane (POSS-PCU), and have been demonstrated to enhance oxidative resistance of polyurethanes [50]. Other recently developed polymer platforms have also been used in the fabrication of durable polymer valves such as hyaluronan-impregnated low-density polyethylene [51], cross-linked poly(styrene-block-iso-butylene-block-styrene) (xSIBS) [52], [53], poly(styrene-block-ethylene/propylene-block-styrene) (SEPS) and poly(styrene-block-ethylene/butylene-block-styrene) (SEBS) [54].

As the work of these research groups seeks to translate this polymer technology into applicable surgical and transcatheter valve replacements (Figure 1-4), some have already published large animal studies [55]–[57], and one has already completed a prospective clinical trial that showed results comparable to BHVs at 1-year follow-up [58]. While the lack of long-term data in this new generation of biostable polymer valves is a concern that cannot be understated,

the revival of this technology to supplement the current armamentarium of valve replacements is encouraging.

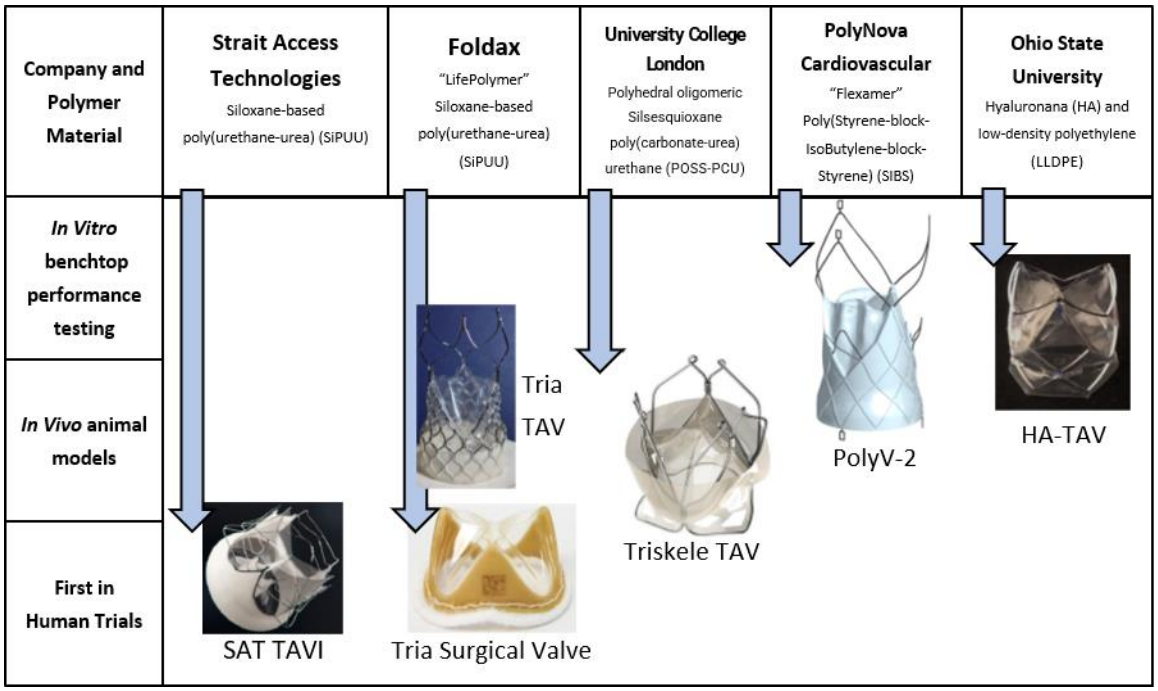

Figure 1-4. Development of biostable polymer valve replacements. Various polymer chemistries and designs are being developed to overcome the degradation of previous generations of polyurethane valves. Reproduced from Kovarovic et al. [53] with permission from ASME.

1.3 Tissue Engineered Heart Valves

1.3.1 Material Selection

Ever since the conceptualization of tissue engineering, researchers have sought to capitalize on the inclination of biological systems to naturally degrade implanted materials. Many of the weaknesses in the aforementioned polymer valves, principally their inability to live up to

their designation as “biostable,” have been seen as possible strengths in what was a paradigm shift to leverage biodegradation as a means toward tissue regeneration [59]. As such, profound efforts, as broad as they are deep, have been undertaken in the field of biomaterials science to identify useful and optimal materials from which to design and build the structures that would serve as scaffolds to facilitate the reconstruction of native tissue.

The first attempt at creating artificial scaffolds for use as heart valves utilized polyglycolic acid (PGA) sheets, seeded with cells harvested from sheep arterial tissue, as a replacement for a single leaflet of the pulmonary valve in a juvenile ovine model [60]. Since then, a broad variety of naturally-derived and artificial materials have been employed in the fabrication of degradable valve scaffolds. Decellularized valves, from either allogeneic or xenogeneic tissue sources, that are re-seeded with autologous cells were initially thought to be a simple and obvious route to produce autologous valves, and were even tested clinically [61]–[63]. However, allogeneic valves lack the supply for sufficient production scaling and xenogeneic valves suffered the same drawbacks as BHVs. Thus, alternative efforts have sought to artificially generate natural polymer scaffolds using fibrin gel molded into a valvular structures [64], [65], or by stimulating ECM production into sheets that can then be mounted on a trileaflet stent [66]. Artificial materials have the advantage of broad customization in terms of biocompatibility, biofunctionalization, mechanical properties, and degradation profiles. Degradable valve scaffolds fabricated from synthetic materials have included poly(carbonate urethane)urea [67], bis-urea modified polycarbonate [68], [69], poly(4-hydroxybutyrate) and gelatin mixtures [70], poly(ε-caprolactone) [71], and hybridized poly(ethylene glycol) and polyurethane [72].

Overall, the selection of material for degradable valve scaffolds is dependent upon the performance requirements of the demanding, dynamic environment of the native heart valves.

Until recently, very few degradable valve scaffolds have been implemented in clinically-relevant large animal models. While biological response to these scaffolds may ultimately be paramount, it is the ability of the material to mechanically withstand perpetual loading cycles that is the principal test. For these reasons, the high tunability of synthetic materials, coupled with their shelf stability and relative ease of synthesis, has made them the more popular choice for fabrication of degradable valve scaffolds.

1.3.2 Polymer Processing

Several of the success criteria for synthetic polymers in serving as degradable scaffolds can be met in the method of polymer processing. As the ultimate goal of these degradable scaffolds is to promote cellular infiltration, a variety of processing techniques have been developed that create interconnected, porous scaffolds. In addition to cellular infiltration, polymer processing techniques can be leveraged to impart specific mechanical or degradation profiles to the scaffold [73]. Given the importance of collagen in the mechanical integrity of heart valves, methods generating a fibrous microstructure seeking to replicate the highly fibrous nature of the valve ECM structure have been favored. The technique used most frequently today to achieve that goal is electrospinning, while other less frequently employed methods have included jet-spinning and melt-electrowriting.

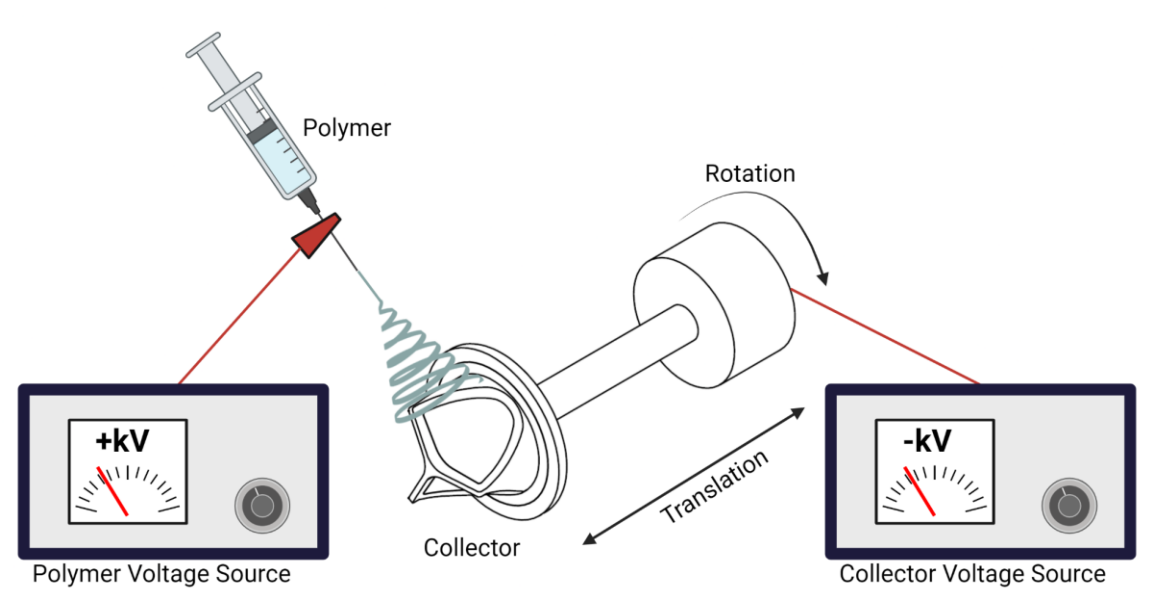

Figure 1-5. Typical electrospinning setup for producing degradable valve scaffolds. Created with BioRender.com.

Electrospinning is a process by which polymer, typically dissolved in a volatile organic solvent, is electrically charged and accelerated through an electric field toward an electrically grounded collecting target (Figure 1-5). The time-of-flight of the solubilized polymer toward the collector allows the volatile solvent to evaporate, creating a bending instability in the solidifying polymer that leads the polymer stream to develop a chaotic, fast-moving whipping motion that stretches the polymer stream into micro-scale fibers as it hits the collecting target. Over time, the micro-scale fibers build up on the collecting target to create a porous, interpenetrating network of fibers. The complex electrohydrodynamic process of electrospinning has been mathematically described [74], and fiber deposition on simple collecting targets has been modeled [75].

Compared to some other polymer processing techniques, electrospinning has a moderately high barrier to entry given the requirement of specialized and costly equipment such as high voltage generators and relevant safety equipment to prevent exposure from volatile organic

compounds. Most conventional electrospinning setups comprise a metallic collecting target, syringe and syringe pump to advance the dissolved polymer, a metal spinneret from which the polymer is ejected, and DC voltage generators connected to spinneret and collecting target. Specific to heart valve scaffold fabrication, the electrospinning fabrications conducted by our group utilize collecting targets custom-built to be geometrically similar to each of the native heart valves, comprising a combination of metallic and insulating components to selectively direct polymer deposition [67]. The collecting target is rotated and translated throughout the fabrication process to ensure complete coverage, finally resulting in a 3D construct resembling the macro-scale geometry and micro-scale fibrillar architecture of the native heart valve.

An aspect of electrospinning that has been the subject of several reviews is the large number of variables that may influence the resultant microfiber morphology. Ramakrishna [76] separates over a dozen of these variables into three broad categories encompassing: (1) polymer solution properties, (2) processing conditions, and (3) ambient conditions. Controlling each of the conditions to maintain adequate repeatability in fiber network morphology, or for isolation of single parameter changes, are significant challenges that often cannot be completely achieved without the implementation of very sophisticated (and thus expensive) equipment. For instance, industrial equipment used to elevate medical devices fabricated by electrospinning to meet the FDA standards of “Current Good Manufacturing Practices” (CGMPs) defined in ISO 13485:2016 has only been achieved by a handful of companies (e.g., Bioinicia, Vivolta).

However, the manipulability of these parameters, and their flexibility in tuning scaffold microstructure, is quite often leveraged to tailor scaffolds to unique applications. In one case involving fabrication of electrospun valve scaffolds, D’Amore et al. [67] was able to manipulate the processing conditions to achieve a polymer structure that closely resembled the native collagen

architecture of the cardiac valves (Figure 1-6). Additional manipulations to the electrospinning process have been very broad, and are extensively reviewed by Xue et al. [77]. In the context of cardiac valve fabrication, electrospinning is being increasingly employed in preclinical and clinical application. As more is learned about the mechanical forces and biological factors influencing valve function and neotissue formation, the high tunability of the electrospinning method—especially when conducted in highly-controlled environments—may situate electrospinning as the most capable fabrication method to recreate optimal conditions for endogenous tissue restoration.

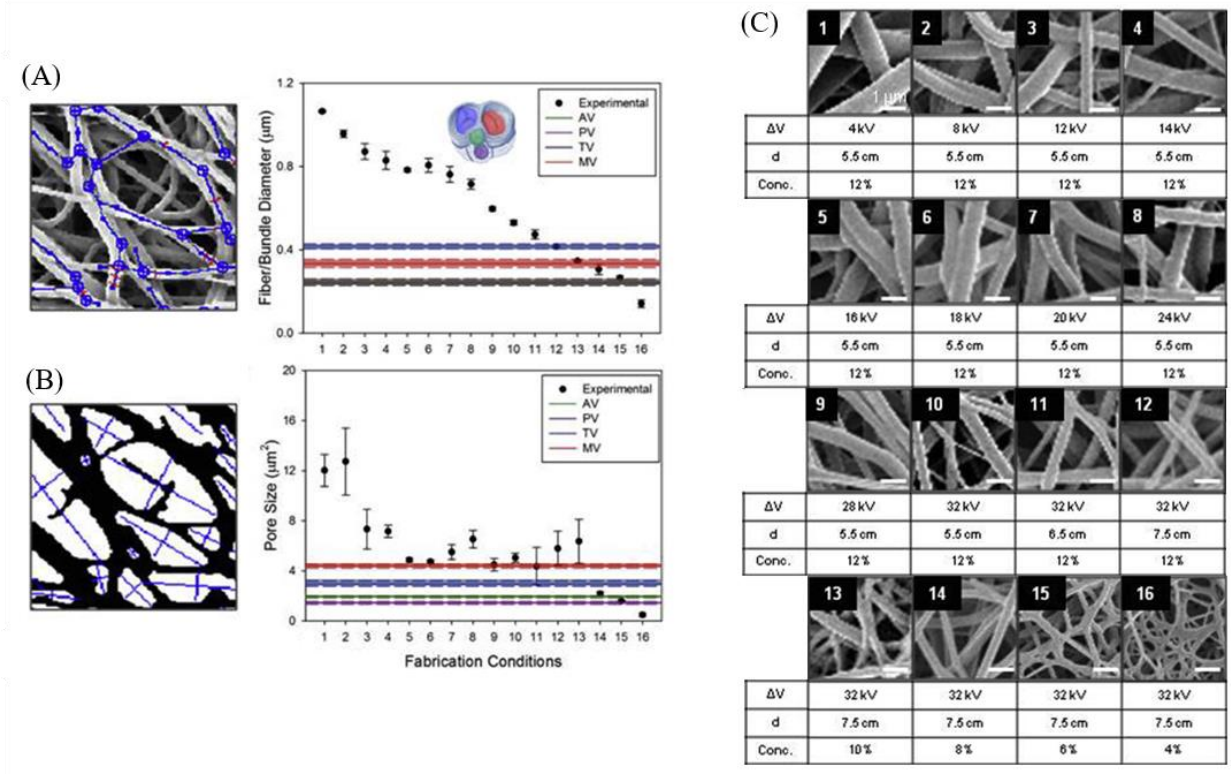

Figure 1-6. Variation of electrospinning parameters demonstrates tunability in porous microfiber network. (A) Example scanning electron micrographs of polymer fiber networks obtained by varying voltage, gap distance, and polymer concentration to demonstrate their influence over fiber morphology. Quantitative assessment of electrospun network morphology shows a trend of decreasing fiber diameter (B) and pore size (C) over a range of fabrication conditions. Adapted from D'Amore et al. [67] with permission from Elsevier.

Jet-spinning, a process to fabricate microfibrous scaffolds used less frequently than electrospinning, does so by centrifugally ejecting a polymer solution from rotating head at rapid speeds [78]. As the polymer is ejected, the inertial forces coupled with the centrifugal trajectory stretch the polymer stream as the volatile solvent evaporates, in a mechanism similar to electrospinning but in the absence of electrostatic forces. A collecting target can be placed in the plane of the polymer ejection to accumulate a bed of highly-aligned, micro- or sub-micron scale fibers. This technique has been employed to fabricate heart valve scaffolds from either a poly(4-hydroxybutyrate)/gelatin mixture [70] or poly(L-lactide-co-ε-caprolactone) [79], having been acutely tested in an ovine model in the latter example.

Melt-electrowriting (MEW), another less common method employed in the production of microfibrous scaffolds, involves the deposition of electrically-charged, molten polymer onto an electrically-grounded collector plate. The plate can be translated in an XYZ coordinate system by computer-controlled motors to build a 3D construct. The nature of MEW deposition allows for a high-degree of control over the structure of the deposited fibers, but is mainly limited by an inability to generate sub-micron scale features the way both electrospinning and jet-spinning can. The macro-sized pores resulting from MEW make these scaffolds unusable without further modification. Attempts at generating heart valve scaffolds using this technique have used MEW to create a skeleton scaffold from poly(ε-caprolactone) (PCL) and fill in the large pores with fibrin gel [71] or elastin-like recombinamer hydrogel [80], but have thus far only been studied *in vitro*.

1.3.3 Structural Mechanics of Heart Valve Scaffolds

In addition to material and processing technique, the structural mechanics of valve scaffolds have a profound impact not only on immediate performance, but also on regenerative

potential. Valve leaflet deformation from shear-mediated forces during systole and pressure-mediated forces during diastole are determinants of the health of the cells inhabiting the scaffold [81]. It has been well-documented that mechanobiological cues influence the health of VICs, valvular endothelial cells (VECs), and ECM. Specifically, under physiological pressure- and shear-mediated mechanical loads of the cardiac cycle, VICs and VECs inhabiting a healthy native valve are able to maintain homeostasis and remain in a quiescent state [81]. However, when mechanical loads diverge from this physiological pattern, either through pathological disease progression or geometric abnormalities such as bicuspid aortic valve, VECs undergo endothelial-mesenchymal transition and VICs are coaxed into an inflammatory and osteogenic state [82].

Study of the structural mechanics of native heart valves has been fairly extensive, particularly for the aortic and mitral valves, at all levels. Macro-scale deformation of the whole valve structure has been studied *in vivo* using radiopaque markers placed on the surface of a single leaflet [83], *in vitro* using stereophotogrammetry to track 3D positions of fiducial markers on a leaflet surface [84]–[87], and *in silico* using sophisticated modeling approaches incorporating comprehensive material parameters developed from experimental measurements [88], [89]. At the cellular level, several studies have sought to understand disease progression and propagation of phenotypic changes within VICs and VECs, caused in part by mechanobiological cues, which have been neatly reviewed by several groups [81], [90].

Due to the importance of mechanics on valvular homeostasis, a number of factors have to be considered in the design of degradable valve scaffolds from a mechanical perspective. Replication of native mechanics is the ideal to which valve scaffolds should aim. Major factors influencing the structural mechanics of designed valves are the overall geometry and the microstructural organization of the fibrillar architecture. In native valves and BHVs, there has been

a substantial amount of research aimed at recreating, and even attempting to optimize, valve geometry in terms of minimizing mechanical stress [91]–[96]. Unfortunately, relatively little comparative study has been conducted for degradable valve scaffolds. As previously noted, a wide variety of both natural and synthetic materials have been used in the fabrication of degradable valve scaffolds, most having only reported on bulk mechanical properties using simple mechanical tests such as uniaxial or biaxial tension. An understanding of a material's bulk mechanical properties is not sufficient as a predictor of mechanical integrity of that material fashioned into valve leaflets, but requires further study into how the geometry and microstructural organization disperses the mechanical load. To this end, only a handful of studies have been conducted, confirming that geometry and microstructure must be accounted for prior to testing of scaffolds as engineered valves [97], [98].

1.3.4 Fluid Mechanics of Heart Valve Scaffolds

The most important aspect of any valve is its ability to not impede forward flow and completely prevent backward flow. Success at this task is directly related to the structural mechanics of valves, namely its ability to easily deflect based on hemodynamic forces. As such, the same parameters governing the solid mechanics (e.g., material properties, processing technique, geometry, microstructural organization) will largely determine the properties of fluid moving through the valve. A great deal of effort has gone into studying fluid mechanics of native valves, BHVs, MHVs, and even biostable polymer valves [12], [51], [99]–[103] using *in vivo* methods, such as 4D-magnetic resonance imaging (MRI), and *in vitro* methods, most often particle image velocimetry (PIV), that generate flow field data in 2- or 3-dimensions. However, as in the preceding section, comprehensive study of degradable valve scaffolds has not yet been undertaken.

There is an obvious difference in flow profiles through MHVs given their unique designs as opposed to the typically trileaflet structure of BHVs and polymer valves. This difference, and the relative values of fluid velocity, shear stress, and turbulence, are drivers of anticoagulation therapy necessitated by MHVs. However, each case of degradable valve scaffold development thus far has been modeled after the native valve design, and is typically assumed to produce physiologically normal flow profiles. To date, only one *in vitro* examination of fluid velocity field has been conducted with degradable valve scaffolds [104]. Given the number of parameters in valve design that influence mechanical deformation of the solid structure, thereby influencing fluid properties, a more detailed investigation interrogating multiple design elements is warranted. Additionally, as computational models of degradable valve scaffolds incorporating structural mechanics, fluid mechanics, and fluid-structure interactions are developed, the output of such models will need to be thoroughly validated experimentally.

1.3.5 Cell Source & Tissue Growth

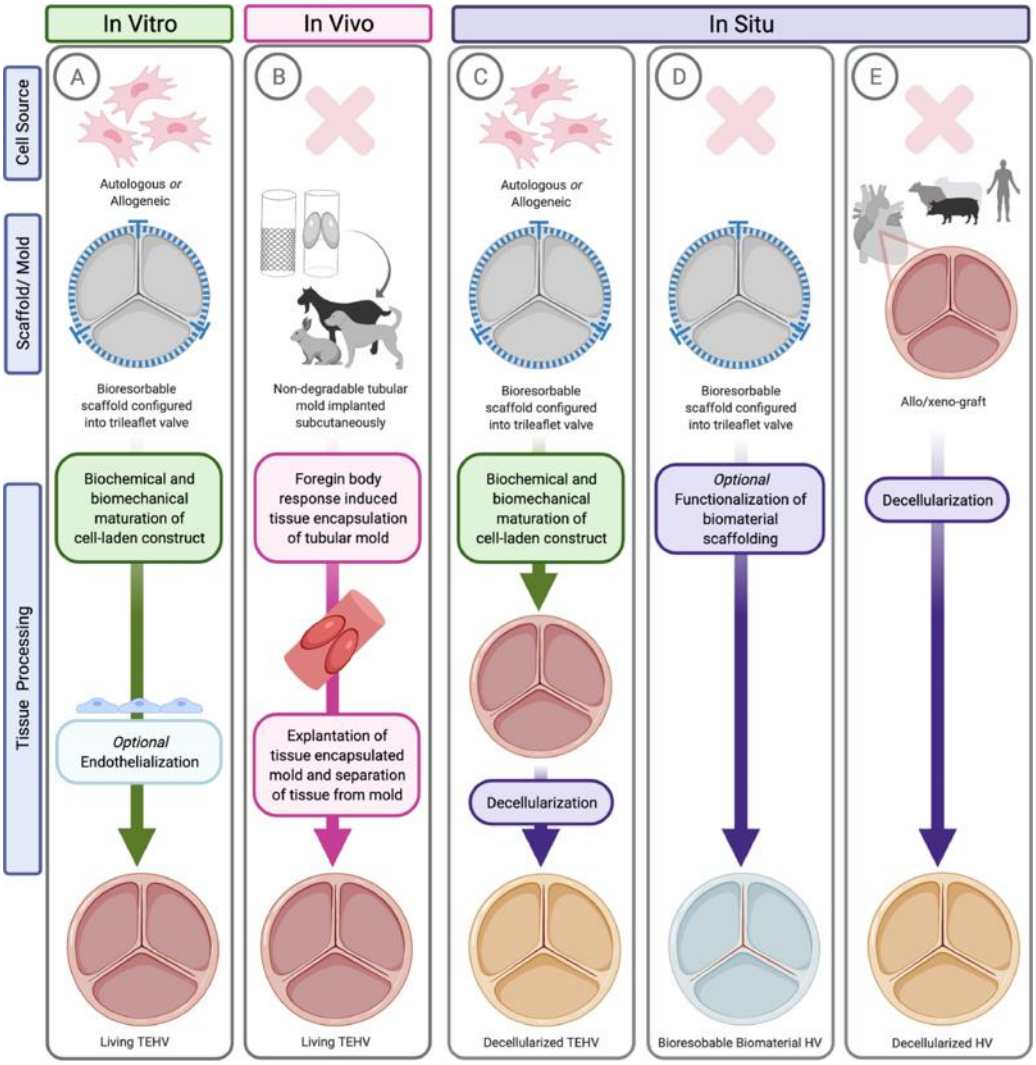

Figure 1-7. Various approaches to tissue engineering heart valve scaffolds. The three common approaches to tissue engineered heart valve application—*in vitro*, *in vivo*, and *in situ*—are so named for the cell source used to repopulate the resorbable scaffolds. (A) *In vitro* tissue engineering cultures cells onto the scaffold in a laboratory setting, typically in a dynamic bioreactor. (B) *In vivo* tissue engineering is the least commonly applied approach, but implants a mold into a living host, typically an animal, until a dense tissue matrix encapsulates the mold. (C-E) *In situ* tissue engineering implants acellular scaffolds, depending on the body's own capacity for cell repopulation and endogenous tissue growth. Reproduced from Mirani et al. [105] with permission from Elsevier.

The goal of tissue engineering to assimilate degradable scaffolds into native tissue has spurred the development of multiple strategies: *in vitro*, *in vivo*, and *in situ*, so named according to the site where tissue growth actually occurs (Figure 1-7). Application of each of these approaches to TEHVs has been reviewed by several research groups in recent years [105]–[107]. The traditional concept of tissue engineering, one that was employed very early on in TEHV development, is to generate a scaffold from either artificial or synthetic material, pre-seed the scaffold with cells, and then implant the cultured scaffold to its intended site [60], [64], [108]–[116]. This approach is now often referred to as *in vitro* tissue engineering for its application of the tissue engineering process in a laboratory environment. Applications of *in vitro* tissue engineering to TEHVs have isolated cells from variety of sources. Cell types most often used are typical of vascular anatomy: fibroblasts, smooth muscle cells, and endothelial cells, sourced from carotid or femoral arteries and jugular veins [64], [109]–[112]. Other cell types, such as bone-marrow mononuclear cells and mesenchymal cells [113], [116]–[118] or amniotic fluid cells [108] have also been used.

A variation on this technique often used in the development of TEHVs includes conditioning the pre-seeded scaffold in a bioreactor to generate the mechanobiological cues to stimulate tissue growth and ECM production in the seeded cells. In fact, a sizable body of research has been devoted to developing and refining designs of suitable bioreactors for TEHVs [119]–[124]. However, *in vitro* heart valve tissue engineering in a bioreactor proved not to be straightforward [125], demonstrated by the diversity in approaches of mechanical stimulation provided. Despite the successful demonstrations of tissue growth *in vitro*, many these valves suffered leaflet thickening and shortening *in vivo* [64], [114], [115], leading to valvular

insufficiency, a common mode of failure in TEHVs. This failure, coupled with costly and time-consuming protocols for cell isolation, expansion, seeding, and culturing, have led many in the field to seek alternative strategies.

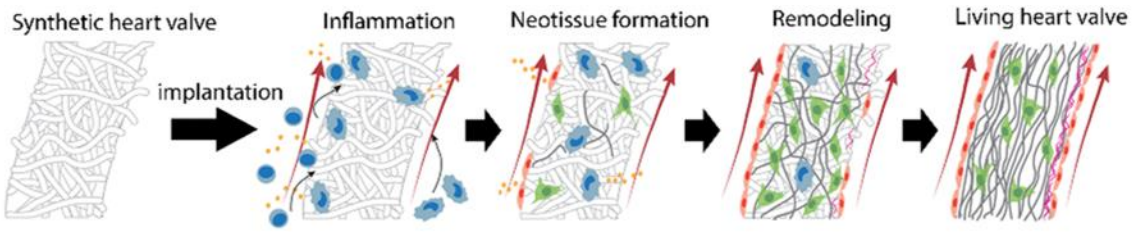

Figure 1-8. Valve scaffold regeneration schematic. The hypothetical process of endogenous tissue regeneration in an acellular scaffold involves a multi-step process of endothelialization, cellular infiltration, and ECM deposition. Reproduced from Kluin et al. [68].

Rather than pre-seed cells onto valve scaffolds and culture them in a bioreactor that attempts to recreate biological conditions, several research groups are moving toward utilizing the body itself as a bioreactor, either by implanting the scaffold material subcutaneously and allowing cellular ingrowth to occur, a process distinguished as *in vivo* tissue engineering, or by implanting an acellular scaffold directly into the valvular position, known as *in situ* tissue engineering, and relying on cells in peripheral tissue and in the circulation to populate the scaffold (Figure 1-8). Use of *in vivo* TEHV development has thus far been limited to a single research group from Japan, and broadly involves the subcutaneous implant of a silicone mold until abundant connective tissue encapsulates the mold, after which the excess is trimmed away and fashioned into a trileaflet valve [126]. The authors have reported successful implantation as aortic replacements in beagle [127] and goat models [128], as well as appropriate *in vitro* function under pulmonary conditions [129]. The longest reported *in vivo* study was 84 days in a beagle model [127], in which they

demonstrated good endothelialization of valve leaflets and conduit and the presence of elastic fibers and α-SMA-presenting cells within the conduit. Despite this reported success, no longer term reports have been yet been published to establish the efficacy of this method, and other groups have raised a variety of concerns that have yet to be addressed [106].

Increasing in popularity in recent years is the *in situ* method of tissue engineering [68]–[70], [79], [98], [130]–[144]. Additionally, the first-in-human application of a synthetic valve uses an acellular scaffold (clinicaltrials.gov ID: NCT03022708). Two main strategies have been developed and implemented in large animal models using this method. The first and more straightforward has been the implantation of an acellular, synthetic polymeric scaffold without prior modification [68]–[70], [79], [130], [132], [136], [137], [139], [144]. The synthetic polymers used in this strategy have been selected based primarily on their mechanical and biological responses, specifically given the high tunability of scaffold mechanics, porosity, degradation profile, etc. from synthetic polymers [106]. The alternative strategy is a hybridization of the *in vitro* and *in situ* methods, where all the steps of the *in vitro* method are followed, including cell seeding onto a natural or synthetic polymer scaffold and conditioning in a bioreactor, with the additional step of decellularizing the scaffold prior to implantation [98], [131], [133]–[135], [138], [140]–[143]. Whether completely synthetic or decellularized ECM, this method has reportedly shown efficacy in animals at long time points between 6 months and 2 years, with some evidence of calcification and leaflet shortening leading to valvular insufficiency [68], [69], [132], [138], [139], [143]. Follow-up studies to the failure mechanisms have shown that computationally-derived, anatomically-inspired geometry has a profound impact on leaflet stretch and tissue remodeling [98], [133], [145]. An advantage that the *in situ* method has over other methods of TEHV production is a reduction in immune reaction to xenogeneic or allogeneic cells and tissues.

Additional advantages, particularly in the case of fully synthetic, degradable polymer valve scaffolds, is lowered production costs due to the lack of cells and culturing, extended shelf stability, and a potentially simpler regulatory pathway to market. Despite these advantages and the mostly successful implementations of the *in situ* tissue engineering method, complete scaffold degradation and tissue remodeling has not yet been achieved, and so the usefulness of *in situ* TEHVs is still unknown.

1.3.6 Current Preclinical Models and Translational Potential

Historical debate over the most appropriate large animal model for preclinical testing of heart valve replacements has now settled to a near-consensus view favoring the ovine model. While canine, swine, caprine, and non-human primate models have been used in the past, the preclinical studies of TEHV implantation cited in the previous section used sheep >90% of the time. There are a variety of reasons owing to this favoring of the ovine model, ranging from anatomical to logistically practical. While this section will summarize the various considerations in choosing an appropriate animal model for TEHV implantation, this is a topic that has been extensively reviewed by other experts in the field [146]–[149].

In the development of TEHVs, regulatory approval requires evidence of safety and effectiveness in preclinical *in vivo* study. To date, preclinical investigation of TEHVs has been nearly exclusively conducted in large animal models, with the primary consideration being similarity in heart size and anatomy to humans. However, there are a number of additional categories to consider when selecting an appropriate animal model for valve scaffold research, including hemorheological similarity to humans, animal behavior, growth rate, and logistics of animal care. While there is no ideal replacement for a human model in which to conduct short-

and long-term preclinical trials, non-human primates would be the closest anatomical and physiological match. Unfortunately, major drawbacks of non-human primates, such as prohibitively high cost and the very strict regulation surrounding their use due to ethical concerns, have precluded their wide-spread use as models for cardiac valve replacement. Instead, the ovine model has become the gold standard of preclinical testing of valve scaffolds by adequately balancing all of the relevant criteria. For example, while cardiac anatomy and hemorheology of pigs more closely resemble that of humans, ovine hearts and blood still share a high degree of similarity [150]–[152]. Pigs, additionally, are relatively the same cost as sheep and have little comparative ethical concern, but have a faster growth rate which can lead to valve size mismatch in longer term studies and can have more difficult husbandry [146], [149]. Dogs, like non-human primates, have garnered greater ethical concerns in the past few decades and higher associated costs, and so are not often chosen for *in vivo* studies any longer. Sheep, on the other hand, present with similar cardiovascular and hemorheological anatomy, are widely available, typically easily handled, relatively low-cost for a large animal, have similar adult size to humans and a slower growth rate than some other mammals.

One area of dissimilarity in sheep is their naturally higher propensity for calcification [153]. The cause for this is not fully understood, but is potentially related to differences in valvular morphology, expression of VIC markers, and immune reaction upon valve implantation [154]–[156]. Regardless, since the primary failure mode of tissue valves involves calcification, some researchers have actually seen this not as a disadvantage of the sheep model, but as a "worst-case-scenario" proving grounds for potential TEHV testing [156]. Additionally, higher levels of circulating calcium in juvenile animals make these models, primarily sheep, desirable for three reasons: to accelerate the process of calcification (weeks to months in sheep, as opposed to years

in humans) [157], [158], to test anti-calcification treatment strategies [31], [159], [160], and to test viability of designed valve scaffolds for pediatric application [138], [143].

While the sheep model is the currently accepted standard for preclinical testing of cardiac valves, in some instances its shortcomings have led to disastrous results upon clinical translation to humans [61], [161]. This has led some to seek alternative models. One possible alternative is the specific breeding of miniature pigs. Since the major drawbacks of typical pig breeds (e.g., widely available feed-stock breeds such as the Yorkshire pig) are rapid growth rate and large adult size, some groups argue that mini-pig breeds overcome those issues and allow researchers to take advantage of the closer cardiac and hemorheological similarity for longer-term *in vivo* studies [162]. However, the mini-pig model has only rarely been used with TEHVs, and has not yet produced convincing long-term data [163]. While search for a better alternative animal model is ongoing, for the present, the sheep model remains the best available model for preclinical study of cardiac valves.

1.4 Pediatric Valve Replacement

1.4.1 Congenital Defects Afflicting the Cardiac Valves

There is a wide range of congenital heart defects (CHD) afflicting one or multiple valves. Most cases of CHD affecting the cardiac valves are asymptomatic and will either remain undetected or go untreated unless they become symptomatic, which may not occur until later in life. The most common example is that of the bicuspid aortic valve. However, other forms of CHD may cause critical or severe stenosis, typically of the aortic or pulmonary valves, and require

immediate intervention in the days and weeks following birth. The aim of this section is to provide a brief overview of common congenital defects that create the conditions necessitating valve repair or replacement and the preferred treatment methods. Thorough anatomical descriptions, developmental mechanisms, and comparative outcomes of each of these conditions and their surgical management lie beyond the scope of this section and can be found elsewhere [164]–[168].

Congenital stenosis is generally caused by obstruction of the ventricular outflow tract, narrowing of the great vessels, or malformation of the valve cusps. In the aortic position, failure of cusp separation during development resulting in either unicuspid, a rare condition, or bicuspid aortic valve may result in critical stenosis [169]–[171]. Pulmonary valve stenosis can occur in isolation or in combination with other defects such as in tetralogy of Fallot (TOF) (Figure 1-9A,B) [172], [173]. The gold standard of treatment for both aortic and pulmonary stenosis is either balloon or surgical valvotomy to increase orifice area, with the former being the preferred method. Success using this palliative treatment is very good, with survival >85% at 10 years for aortic valves [168] and >90% at 25 years for pulmonary valves [172]. A common complication with either approach, for both aortic and pulmonary valves, is late regurgitation that can require valve replacement. Pulmonary valve replacement after initial valvotomy is not typically necessary until these patients are well into adulthood, with reports of 20-33 years post-intervention on average [174], [175]. On the other hand, need for aortic valve replacement is unavoidable for some pediatric patients, with only 55% freedom from valve replacement at 20 years being reported after initial intervention [170]. For these patients, the Ross procedure is usually performed [167], in which the native aortic valve is removed and replaced with a pulmonary autograft and the pulmonary valve is subsequently replaced with a cryopreserved or decellularized allograft (Figure 1-9C) [176].

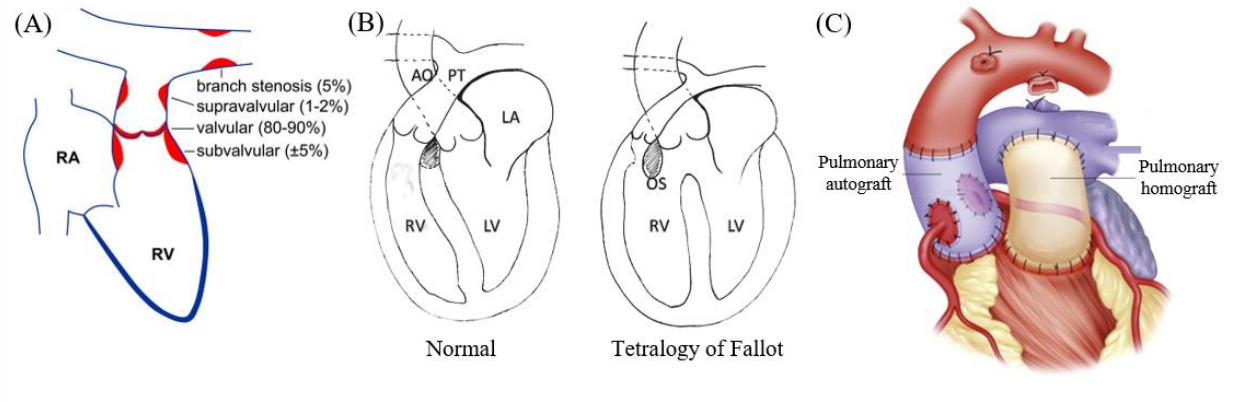

Figure 1-9. Congenital heart defects requiring valve replacement. Pulmonary stenosis, occurring either in isolation (A) or in combination with other congenital defects, as in tetralogy of Fallot (B) may be severe enough to warrant intervention, occasionally requiring valve replacement. Congenital defects of the aortic valve are often remedied by the Ross procedure (C), whereby the native pulmonary valve is used as an autograft, and is subsequently replaced from an external source. (A) Reproduced from Cuypers et al. [172] with permission from BMJ Publishing Group Ltd. (B) Reproduced from Griselli et al. [164] with permission from Springer. (C) Adapted from Henaine et al. [177] with permission from Elsevier.

While cases of CHD causing critical stenosis are the most prevalent cases requiring valve repair or replacement in children, there are several other rare conditions that may necessitate intervention. Examples include Ebstein's anomaly causing tricuspid valve regurgitation [178], mitral valve prolapse either in isolation or following atrioventricular septal defect repair [179], and truncal arteriosus causing regurgitation in the congenitally-deformed truncal valve [180]. As with the conditions described in the previous paragraph, given the particular challenges following valve replacement in the pediatric population, this treatment option is usually deferred in favor of repair when possible.

1.4.2 Specific Challenges of the Pediatric Population

Although valve replacement is avoided and deferred as long as possible in the pediatric population, there are still several cases in which replacement is the only viable option [177], [181]. In these instances, clinicians face specific challenges unique to the pediatric population. Because there has not yet been any practical surgical intervention or valve prosthesis that singularly resolves all of these issues, treatment course is generally agreed upon in only a few scenarios, while some others may still be controversial.

The major challenge in replacing valves in children is their natural state of growth. Prosthesis-patient mismatch is a chief concern when replacing native valves with alternatives that carry no growth capacity. Placement of a valve that a pediatric patient will outgrow can lead to deterioration of ventricular function due to increased ventricular load, necessitating one or more reoperations [167]. On a cellular level, the biological milieu of children in a growth state is dramatically different than the adult or elderly population. Indeed, the rapid progression of calcification and degeneration of BHVs and allografts in younger patients is a well-known phenomenon. While the exact culprits for accelerated degeneration have yet to be fully identified, a recent study by Xue et al. quantified calcification and collagen cross-linking in BHV tissue samples after incubating in human blood serum from pediatric and adult volunteers [182]. The main finding was that higher concentrations of calcium, phosphate, alkaline phosphatase, and advanced glycation end products in the serum samples of young volunteers very likely resulted in the higher quantity of calcium deposition and disruption of the collagen network in the BHV samples. Alternatively, MHV replacement requires strict adherence to anticoagulation therapy, which clinicians are reluctant to prescribe to children given their increased activity state and potential lack of compliance [183].

In high income countries such as the United States, valve disease requiring intervention in the pediatric population predominantly stems from CHD affecting the cardiac valves. By contrast, there is a comparatively greater global burden of rheumatic heart disease (RHD) necessitating valve intervention [184]. Infection with acute rheumatic fever usually manifests as RHD in adulthood, but low- and middle-income countries still see an unfortunately high number of pediatric cases [185]. Among other symptoms, RHD may cause inflammation of the valves, most frequently the mitral valve, eventually leading to mitral valve regurgitation requiring intervention [184]. Most of the challenges with performing valvular intervention on children with RHD are the same as those described in the preceding paragraph. However, the greatest challenge specific to successfully treating RHD in low- and middle-income countries is lack of access to sophisticated cardiac surgical centers with enough experience to successfully operate cardiac valves [186], [187]. Looking at a registry of RHD cases in Uganda, Zimmerman et al. found that, of 612 pediatric cases, only 73 (12%) received cardiac intervention, and only 11 of those were performed in-country [188]. Additionally, adequate follow-up with these patients is especially challenging [186], [189].

Ongoing efforts in the treatment of pediatric patients, both with CHD and RHD, have been continually progressing over the past several decades. Survival rates of CHD have dramatically improved even in the past three decades thanks to advancements in imaging modalities, prenatal diagnosis, and surgical approaches [190]. However, these children still require regular follow-up into and through adulthood, and reintervention is often still necessary. The same may be said for pediatric RHD patients requiring valve repair or replacement, with the added challenges of lack of access to comprehensive care. In the ongoing goal of providing an ultimate solution to pediatric valve disease, there are many who hope that the development of TEHVs designed specifically for

the pediatric population will encourage native repopulation of the implanted scaffold, giving it the capacity for somatic growth [105], [191].

1.4.3 Pediatric Cardiac Valve Scaffold Development

Suboptimal outcomes from valve repair and replacement in children, given their unique set of challenges, has inspired the development of a valve capable of both acceptable performance and growth. Particular interest has been paid to two parallel pathways: TEHVs and decellularization and preservation methods for allografts and xenografts. Cryopreserved allografts and xenografts have been used as both aortic and pulmonary valve replacements extensively for decades, but have a high rate of reintervention even just a few years after initial placement in children, typically brought about by immune reaction to residual cellular material leading to valve calcification and degeneration [192]–[194]. As a response, allografts stripped of cells and DNA through a variety of decellularization protocols have been used in juvenile large animal studies and human trials. Cebotari et al. repopulated decellularized allografts with endothelial progenitor cells *in vitro* prior to pulmonary valve replacement in two children, and reported increased PV annular diameter at 3.5-year follow-up [62]. However, other studies with larger cohort sizes have reported equivocal results on valve growth [195], [196]. Multiple preclinical reports of decellularized allografts and xenografts being implanted into the aortic and pulmonary positions of lambs and minipigs have repeatedly shown some degree of, albeit incomplete, host cell repopulation, minimal calcification, and *de novo* ECM deposition [197]–[199]. Although long-term data on growth accommodation are unfortunately lacking, sourcing allograft tissue is difficult, xenograft immunogenicity still remains a problem [61], [200], and the pre-processing methods are expensive, there is some

optimism that decellularization of allografts and xenografts may prove an effective treatment strategy for pediatric valve replacement.

Valve scaffolds intended for degradation and resorption have represented more recent attempts at providing an optimal solution for pediatric patients that accommodates growth. The most advanced efforts at engineering pediatric valve scaffolds come from the Netherlands-based company Xeltis and the Tranquillo research group at the University of Minnesota. The Xeltis pulmonary valve conduit (XPV) is an acellular, polymeric scaffold currently in clinical trials (clinicaltrials.gov ID: NCT03022708) for RVOT reconstruction (Figure 1-10). At 24-month follow-up, five patients receiving the XPV developed severe regurgitation and five more developed moderate regurgitation [201]. The authors speculated early mechanical failure of the valve cusp. To address this, the valve design was updated and, with the exception of 1 graft failure that the authors speculate was related to hyperimmune response, has reported good success in six additional patients at 12-month follow-up [202].

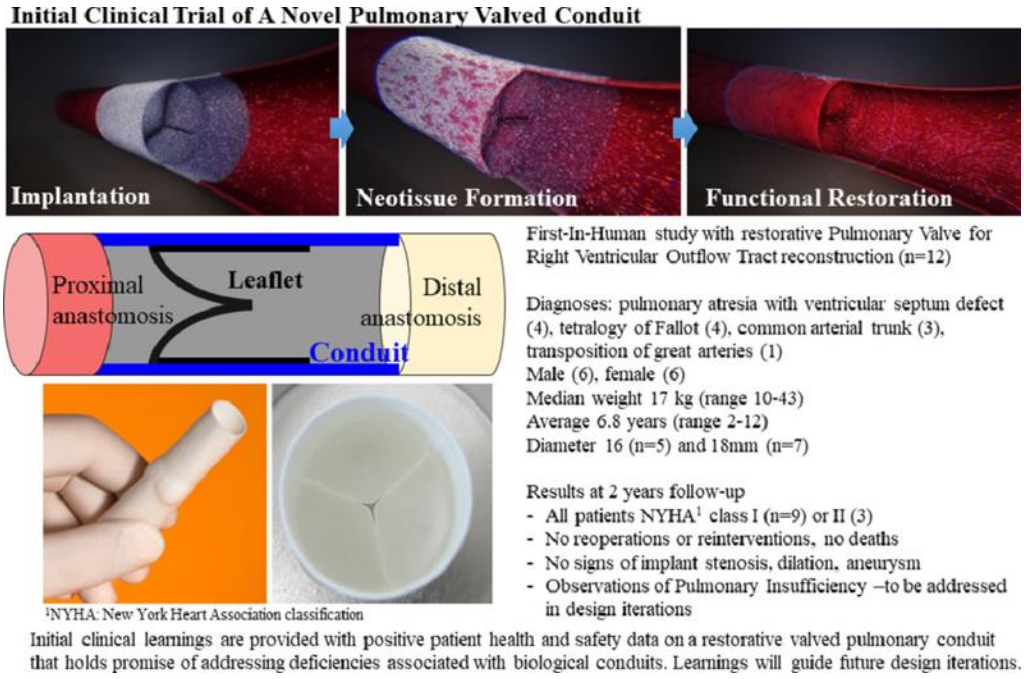

Figure 1-10. Acellular, polymeric pediatric pulmonary valved conduit. Fabricated by electrospinning from supramolecular 2-ureido-4[1H]-pyrimidone (bottom panel), the valved conduit scaffold uses the in situ tissue engineering approach (top panel). It is inserted proximally at the right ventricular outflow tract and is anastomosed distally to the pulmonary artery (middle panel). Reproduced from Prodan et al. [201] with permision from Elsevier.

The Tranquillo group also uses the *in situ* approach, but instead fabricates a valved conduit from decellularized ECM sheets produced by *in vitro* cell culture [65]. In their most recent report, two iterations of valved conduit scaffold design were implanted in the pulmonary position in a growing lamb model and followed for one year (Figure 1-11) [138]. The first-generation design resulted in excessive dilatation in 2 of 3 conduits implanted, leading to severe regurgitation. To remedy this, the authors reinforced the conduit with an additional tube of ECM material in their second-generation design. Despite moderate regurgitation in 1 of 3 second-generation conduits, they claim to have resolved the major issue of dilatation in the pulmonary root. Additionally, all of the second-generation scaffolds showed abundant recellularization, absence of leaflet

thickening and shortening, and minimal calcification (compared to BHV control group). While there is still much developmental work that must be done to improve consistency of outcome with these scaffolds, there is no doubt that the preclinical results reported in Syedain et al. [138] are positive and represent a major step forward for this TEHV approach.

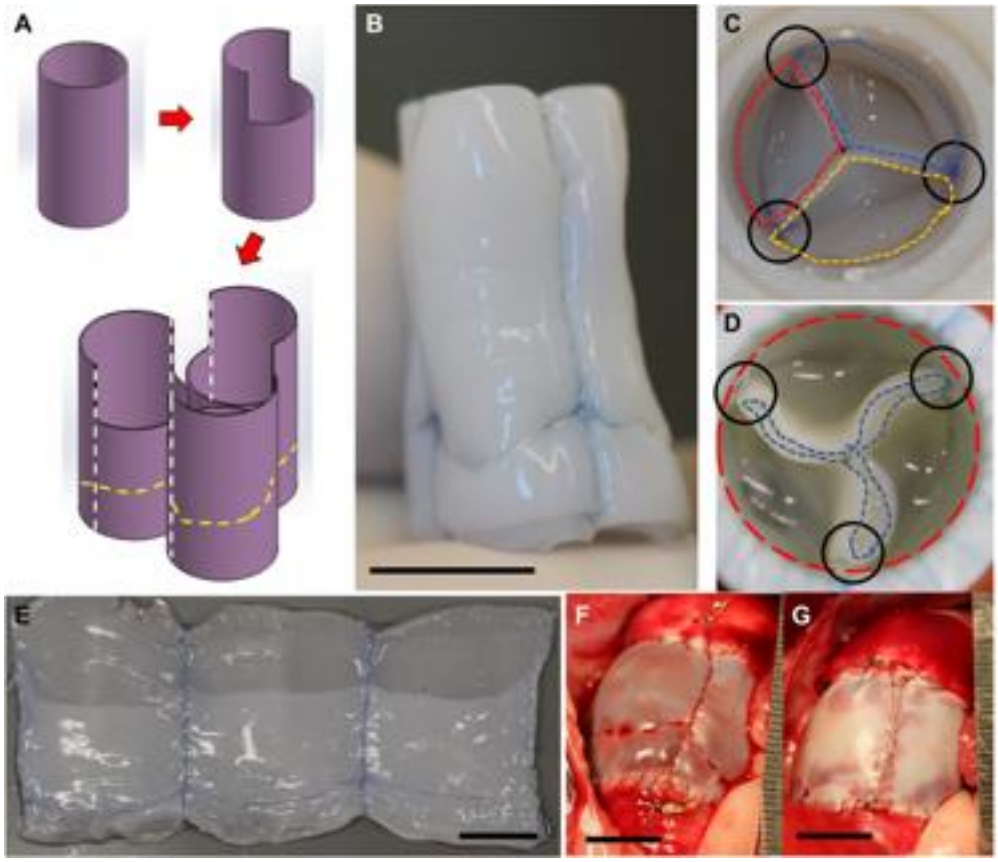

Figure 1-11. Decellularized ECM-based pediatric pulmonary valved conduit. (A,B) Construction of valved conduit by suturing three ECM tubes. (C,D) Comparison of second and first generation designs, respectively. (E) Open view of valved conduit. (F,G) First and second generation valved conduits *in situ*, respectively. Reprinted from Syedain et al. [138] with permission from AAAS.

There are still a few other research groups working toward the goal of developing growing valves. Our own group has attempted implantation of valve scaffolds mounted on totally

degradable magnesium alloy stents in an adult swine model [136]. Despite the acute nature of the study and its limitations, degradable metallic stents incorporating degradable polymeric valves are an area of great interest for pediatric application, and further development of degradable metallic stents useful for mounting valve scaffolds is a continuing effort [203].

Although the most advanced modes of accommodating growth in pediatric patients all leverage the native capacity for cell repopulation and endogenous tissue growth in degradable valve scaffolds, there are still some novel endeavors to create non-degradable valves that, though they do not have a natural capacity for growth, are designed with the capability of expansion. The most well-known is the Melody valve (Medtronic), a glutaraldehyde-treated bovine jugular vein valved conduit mounted on a platinum-iridium stent [204]. Despite being FDA approved exclusively for pulmonary valve replacement, it was discovered that the design of the venous valve lends itself to progressive balloon dilatation without compromising valve cusp coaptation, leading to off-label use in progressive expansion of the conduit diameter to accommodate growth in multiple valve positions, most notably the mitral valve [205]. However, it has been repeatedly noted that the Melody valve, as with any other BHV, suffers early degradation and is not a permanent solution, but the main advantage instead lies in delaying the need for reintervention until the valve annulus reaches adult size [206]. One other expandable, non-growing valve currently under development is the low-force expandable/adaptable pediatric (LEAP^{TM}) valve. Produced by the non-profit Charles Stark Draper Laboratory, Inc., the expansion mechanism is meant to apply an outward force onto the arterial wall, allowing stent expansion as arterial diameter increases. Not much technical information has been made publicly available, but preclinical trials are reportedly ongoing [207].

While no ideal valve replacement has presented itself for this urgent unmet clinical need, the degree of innovation has been encouraging, especially understanding the proper context of the number and difficulty of the challenges that pediatric valve replacement poses. Indeed, the technological developments even within the past five years have produced potential alternatives to the standard options that may revolutionize pediatric valve repair and replacement.

1.5 Objectives

As thoroughly described in the preceding sections, current state-of-the-art valve technology is only successful insofar as it extends life expectancy for patients with either congenital or acquired valvular heart disease, yet with significant limitations for quality of life. While the body of work conducted on cardiac valve development has been extensive, ranging from mechanical, bioprosthetic, polymeric, allo/xenogeneic, and tissue engineered, there is still no optimal valve replacement that serves as an enduring and uncomplicated solution. Additionally, pediatric patients requiring valve replacements are left with options nearly guaranteed to fail, only expected to serve as palliative care until fully grown. The broader goal of the work reported here would ideally be a realized, clinically-translated TEHV to serve recipients with the regenerative capacity for whom this technology would be most beneficial. As an iterative step toward that goal, it has been the objective of this work to characterize both structural and fluid mechanical effects of design iterations and material variation of degradable polymeric cardiac valve scaffolds.

1.5.1 Objective 1 – Interrogate the Influence of Polymer Stiffness and Geometric Design on Structural Mechanics in Tissue Engineered Pulmonary Valve Scaffolds

Valve scaffolds having an array of material stiffness values, modulated by adding incremental amounts of poly(ε-caprolactone) into poly(carbonate urethane) urea, and two distinct valve geometries, inspired by either clinically-used transcatheter valves or derived from anatomically "optimized" valves, were fabricated via electrospinning. Valve scaffold microstructural and mechanical properties were quantified using SEM, uniaxial, and biaxial tension. A custom mock circulatory loop was developed to test valve functional performance—measuring pressure gradient, orifice area, and regurgitant fraction—and dynamic structural mechanics. An array of markers was affixed to all valve scaffolds and images were acquired at peak systole and mid-diastole. Using an image of the markers in an unloaded state as a reference, strain profiles of valve leaflet surfaces were generated.

1.5.2 Objective 2 – Interrogate the Influence of Polymer Stiffness and Geometric Design on Fluid Mechanics in Tissue Engineered Pulmonary Valve Scaffolds

Valve scaffolds with the same array of material stiffness and geometries as in Objective 1 were placed into a custom mock circulatory loop, where valve functional performance was again measured. The fluid mechanical properties were quantified at 25 ms intervals throughout the cardiac cycle using particle image velocimetry (PIV). Mathematical decomposition of the resultant fluid velocity fields was then used to quantify stress and turbulence downstream of the valve scaffolds caused by increasing material stiffness and differing geometry.

1.5.3 Objective 3 – Strategy for Miniaturization of Valve Scaffold Design for Pediatric Use

To assess the capacity for scaling down the valve scaffold manufacturing technique, a geometrically similar electrospinning mandrel with annular diameter of 16 mm (downscaled from 23 mm) was manufactured. Polymer microstructure and biaxial mechanics of adult- and pediatric-sized scaffolds were measured to quantify any differences imparted due to changes in collector mandrel design. Pediatric scaffold functional performance was then assessed in a mock circulatory loop to quantify pressure gradient, orifice area, and regurgitant fraction.

2.0 Cardiac Valve Scaffold Design: Implications of Material Properties and Geometric Configuration on Performance and Mechanics

2.1 Introduction

(Note: this chapter was previously published as: D. D. Pedersen, S. Kim, A. D'Amore, and W. R. Wagner, "Cardiac valve scaffold design: Implications of material properties and geometric configuration on performance and mechanics," J. Mech. Behav. Biomed. Mater., vol. 146, no. July, Jul. 2023, doi: 10.1016/j.jmbbm.2023.106043.)

Design of an optimal scaffold for heart valve replacement has thus far been elusive. Of the many design parameters, two that could be thought of as relatively simple are the inherent material stiffness and overall scaffold geometric configuration. However, even these are not so trivial. Material stiffness of native valve structures is highly anisotropic and non-linear, imparted by the organization of the collagen network. Additionally, material mechanics are subject to change over time with cyclic loading [27], [89], [208]. Valve geometry has an obvious effect on blood flow, and designing a scaffold for tissue engineering that recreates the native valve geometry has been a common objective. Yet, there are several differing approaches of how best to model valve scaffolds given the dynamic and complex nature of native heart valves, which are succinctly reviewed elsewhere [209].

These two design parameters, material stiffness and geometric configuration, both influence the mechanical response of the valve scaffold, but another factor that requires consideration is the degree to which each of these variables affects overall performance and

specific mechanical behavior under dynamic conditions. Therefore, the objective of this study was to design a series of valve scaffolds, manipulating material stiffness and geometric configuration, and measure both valve performance and leaflet strain under pulsatile flow. Specifically, incrementally blending elastomeric poly(carbonate urethane)urea (PCUU) with relatively stiffer poly(ε-caprolactone) (PCL) grants a high degree of control over the material properties. Additionally, two geometric configurations based on either a clinically-available pericardial valve [210] or a structurally "optimized" valve [91] are compared. The mechanical aspect of this study aims to observe magnitudes of mechanical strain experienced in the valve scaffolds and identify trends as material stiffness or geometry changes, all while comparing to overall scaffold performance using typical clinical metrics (e.g., orifice area, transvalvular pressure gradient).

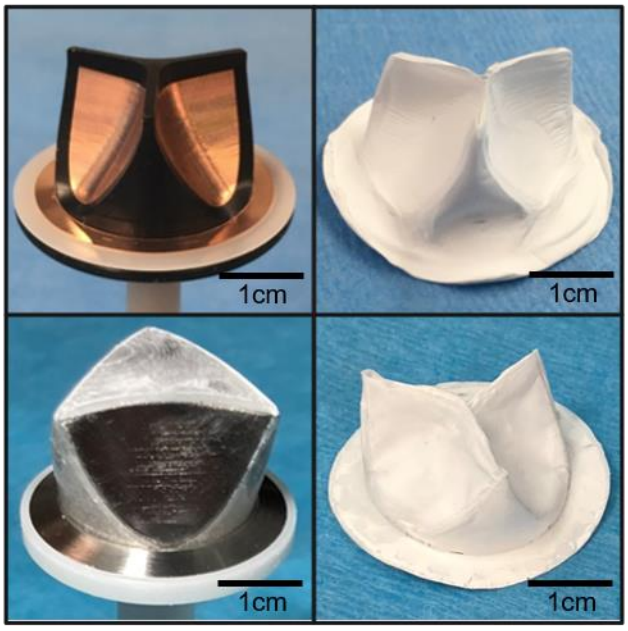

Figure 2-1. Geometric configurations of double-component deposition electrospinning collectors based on parametrization of pericardial bioprosthesis (Mark 1 Design; top left) and "optimized" Thubrikar valve, with modifications (Mark 2 design; bottom left) with resultant electrospun valve scaffolds (top right and bottom right, respectively).

2.2 Materials and Methods

2.2.1 Cardiac Valve Scaffold Design

The two cardiac valve scaffold architectures used in this study were designed according to different sources. The first leaflet geometry (Figure 2-1, top), designated Mark 1 (Mk1), was designed based on a parametrization of a clinically-available pericardial bioprosthetic valve [210]. The second leaflet geometry (Figure 2-1, bottom), designated Mark 2 (Mk2), was based on the design by Thubrikar [91], with modifications. Specifically, the overall leaflet height, the leaflet free edge length, and the leaflet surface area were preserved from the original CAD rendering of the Thubrikar model and translated into a 3-sided flat-faced structure that served as a target for polymer deposition by electrospinning.

Leaflet profiles of both Mk1 and Mk2 geometric configurations were manufactured into double-component deposition mandrels for electrospinning, in the manner of D'Amore et al. [67]. The two-component mandrels comprise a conductive metallic material making up the leaflet portion of the valve geometries and an insulating plastic material covering corners and points of charge concentration (Figure 2-1).

2.2.2 Polymer Processing and Scaffold Fabrication

Cardiac valve scaffolds were fabricated from blends of poly(carbonate urethane) urea (PCUU) and poly(ε-caprolactone) (PCL). PCUU was synthesized using previously reported protocols [211]. PCL was used as purchased (Mn=80kDa; Sigma-Aldrich). Four different blends were used to interrogate the effect of material stiffness on valve performance according to

PCUU/PCL weight ratios. These groups are hereafter referred to by their relative percent PCL weight content: PCL5, PCL15, PCL25, PCL35. PCUU/PCL blends were dissolved in 1,1,1,3,3,3-hexafluoroisopropanol (HFIP) at 12% (w/v) and electrospun on either Mk1 or Mk2 geometries. The electrospinning fabrication was separated into a four-stage process, each targeted to distinct locations designed to produce scaffolds of even thickness across the entire surface of the DCD mandrels. Electrospinning parameters shared across all four stages were as follows: polymer flow rate of 1.5mL/hr, polymer charge of either +7kV (Mk1)/+6kV (Mk2), mandrel charge of either -6kV (Mk1)/-5kV (Mk2), polymer-mandrel gap distance of 5cm, conditional mandrel rotation of 10rpm, and conditional translation of 1cm/sec. The first stage focused fiber deposition onto annular sewing ring with mandrel rotation and no translation for 12min. The second stage focused fiber deposition onto leaflet surfaces for either 5min (Mk1) or 7min (Mk2) per leaflet surface with translation but no mandrel rotation. The third stage was general deposition over the entire surface for either 13min (Mk1) or 17min (Mk2) with mandrel rotation and translation. The fourth stage focused deposition on commissures for 6min with translation but no mandrel rotation. Target average leaflet thickness for all electrospun valve scaffolds was 250μm, which was measured at 15 locations on the leaflet surface using a dial indicator pocket gage (1010MZ, Starrett).

2.2.3 Scaffold Material Properties

Material stiffness was characterized primarily through uniaxial tension to failure. Tensile tests were conducted on a 2kN force capacity loader (MTS Insight 2 SL, MTS Systems) using a 100N load cell and extension rate of 10mm/min, as in Hong et al. [211], on dog-bone cutouts from the circumferential direction of valve leaflets. Additionally, 10x10mm specimens from the belly region of valve leaflets were loaded biaxially to 500kPa tension on using previously established

protocols [212], [213]. A common approach to quantify material properties using biaxial loading data has been to calculate the tangent modulus from the linear region of both axes [214]. Comparisons between the secant modulus at 10% strain of uniaxial experiments and tangent moduli of biaxial experiments were performed. Finally, fiber microstructure was quantified by image analysis of scanning electron micrographs (SEM; JSM 6335F, JEOL) using an established custom Matlab program to programmatically calculate variables of interest [215].

2.2.4 Mock Circulatory Loop

To test valve scaffolds under dynamic conditions, a mock circulatory loop was constructed according to specifications found in ISO 5840-2:2021 (Figure 2-2). The mock circulatory loop consisted of trapped air compliance chamber and gate valve which could be tuned to emulate physiological pulmonary compliance and resistance. The working fluid was 41% glycerin in water to simulate the kinematic viscosity of blood in large vessels (measured kinematic viscosity, ν=3.48cSt). Pulsatile flow was provided by a servo cylinder (Model A1NZ9B, Ultra Motion) compressing a fluid-filled bellows at a rate of 72bpm and stroke length of 6.5cm (yielding stroke volume of 70mL and cardiac output of 5 L/min). The servo cylinder was not mechanically attached to the bellows, permitting passive filling of the ventricular portion of the mock circulatory loop during the diastolic phase of the cardiac cycle. A non-degradable polyurethane valve taken from a BVS 5000 blood pump (Abiomed) served in the atrioventricular valve position between the reservoir and ventricular portion of the pump.

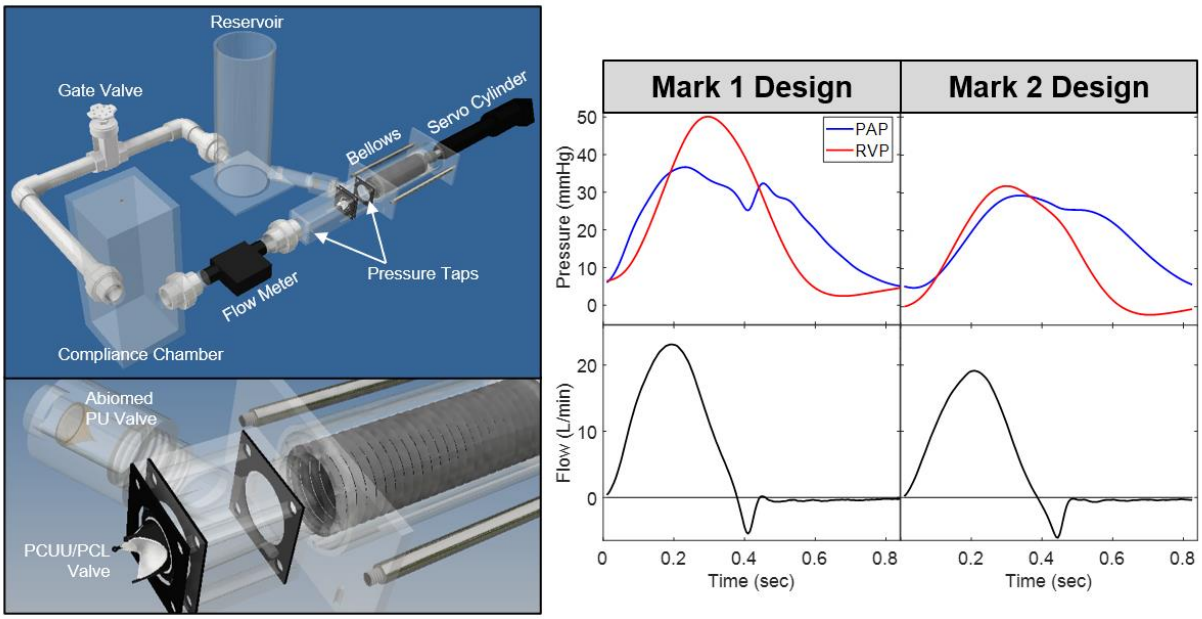

Figure 2-2. Schematic of mock circulatory loop showing all components (top left) including resistance element (gate valve), compliance element (trapped air compliance chamber), reservoir, and servo cylinder pump. (Bottom left) Highlight of the ventricular chamber showing Abiomed polyurethane valve, compressible bellows, and electrospun trileaflet valve scaffold. (Right) Representative plots of pressure and flow waveforms of valve scaffolds from both Mk1 and Mk2 designs. PAP=pulmonary arterial pressure, RVP=right ventricular pressure

Given the emergence of initial clinical trials of tissue engineered valves in the pulmonary position, valve scaffolds from all groups used in this study were mounted on a custom stent and tested under physiological pulmonary conditions (Figure 2-2). Two pressure transducers (Model 1501A12EZ5V5GPS, PCB Piezoelectrics) were used to measure pulmonary arterial pressure (PAP) downstream of the valve and right ventricular pressure (RVP) upstream of the valve. Resistance and compliance levels were set to produce a PAP ranging between 25-30mmHg during systole and 5-10mmHg during diastole. A 25mm diameter in-line flow probe (ME25PXN, Transonic) connected to a TS410 flow meter (Transonic) was used to measure instantaneous flow.

Pressure and flow waveforms were recorded using a custom LabView program. Pressure and flow waveforms averaged over 10 cardiac cycles were then used to calculate flow performance metrics identified in ISO 5840-2:2021. These included the mean transvalvular pressure gradient (ΔP)—defined as the mean difference between PAP and RVP during the positive differential pressure period, and the regurgitant fraction—defined as the ratio of regurgitant (backward) flow to forward flow. Also calculated was the effective orifice area (EOA) which is defined by Equation 2-1 where QRMS is the root-mean-square forward flow during the positive differential pressure period, ΔP is the mean transvalvular pressure gradient, and ρ is the fluid density.

$$EOA = \frac{Q_{RMS}}{51.6\sqrt{\frac{\Delta P}{\rho}}} \tag{2-1}$$

A CMOS camera (MU300, AmScope) was positioned perpendicular to the flow direction through the valve to capture short-axis video of valve operation, which was then used to directly measure geometric orifice area (GOA), defined as the area encompassed by the perimeter of the valve free edge, in a custom Matlab program.

2.2.5 Dynamic Strain Mapping

2.2.5.1 Image Acquisition

To measure strain in valve scaffolds, a grid of markers spaced 1.6mm apart in black ink was positioned on the surface of one leaflet (Figure 2-3C). Two identical CCD cameras (Manta G504-B, Allied Vision Technologies) with adjustable focal length lenses (EF-S 18-55mm, Canon) were positioned below the valve, angled 30 degrees below the horizontal plane and oriented 12.5 degrees from the longitudinal line of the valve scaffold (Figure 2-3A,B). Before pump operation, images of the markers were first obtained with the fluid in a static state and then used as unloaded,

reference positions in strain calculations. During pump operation, images were simultaneously acquired from both CCD cameras at timepoints coinciding with peak systole and mid-diastole triggered by an external synchronizer (LaserPulseTM Model 610036, TSI Inc.).

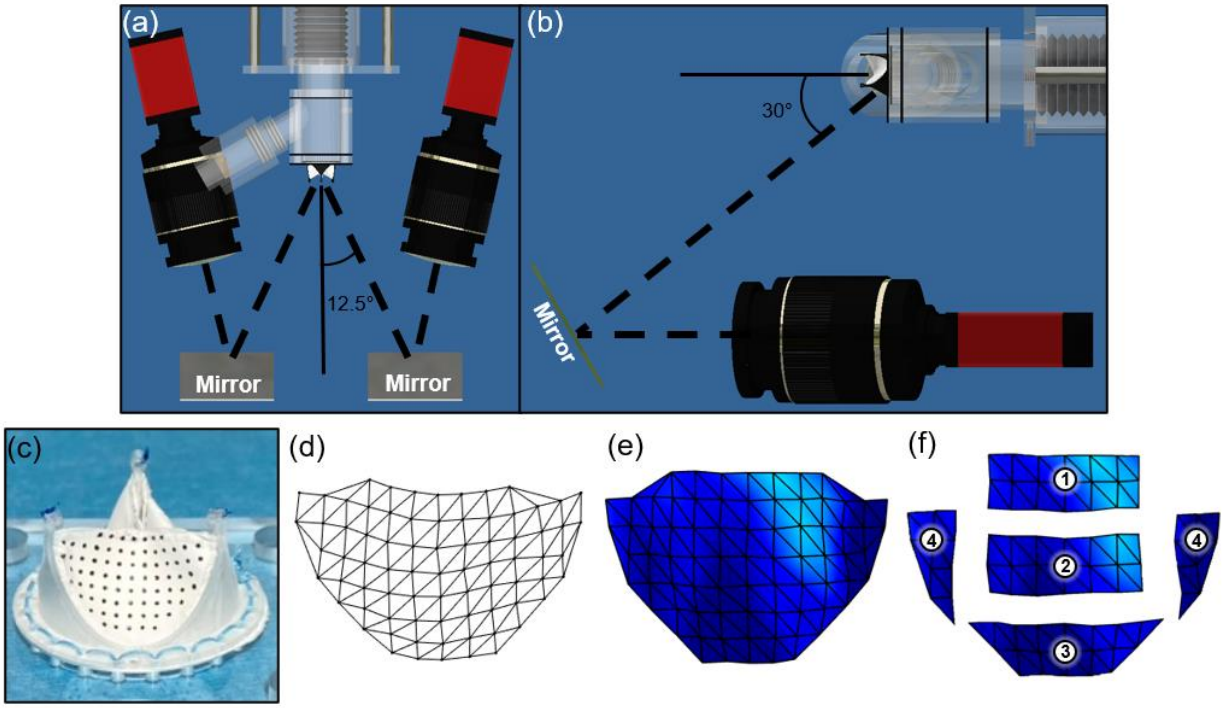

Figure 2-3. Schematic of stereoscopic camera setup showing (A) horizontal and (B) vertical angles of both cameras to valve scaffold. (C) Marker grid placed on leaflet surface used to reconstruct leaflet surface in (D) 3D space. (E) Representative image of strain mapped onto 3D reconstructed surface and (F) broken into 4 distinct regions: (1) leaflet free edge, (2) belly, (3) base, and (4) commissures.

2.2.5.2 3D Image Correlation

Prior to valve scaffold data collection, approximately 20 images of a checkerboard calibration grid (10x7 black and white squares, 1.27mm square length) being randomly translated and rotated up to 45 degrees within the field of view of both cameras were acquired. 3-dimensional spatial calibration of acquired images was performed using a built-in Matlab application Stereo Camera Calibrator, which is an implementation based on framework by Zhang [216] and Heikkila

and Silven [217], to track intersections of white and black squares on the checkerboard grid. The application corrects for radial lens distortion and calculates overall mean reprojection error, a description of the distance between the measured point in 2D images and the projected point in 3D space, which across all calibration images was 1.50 pixels.

After stereo camera calibration, the camera parameters were applied to images of valve leaflet markers in a custom Matlab program to obtain 3D spatial coordinates of all markers placed on valve leaflets at all three positions—static, peak systole, and diastole (Figure 2-3D).

2.2.5.3 Strain Calculation

Spatial coordinates of the marker grid were fit with a Delaunay triangulation prior to strain calculation. Subsequently, static valve position and each loaded valve position were imported into FEBio Studio, a software tool designed for biomechanical calculations using finite element analysis, where Green-Lagrange strain was calculated from the triangulation. Strain tensors were separated into circumferential (CD) and radial directions (RD) for both systolic and diastolic loads. Overall mean and peak strains are reported in addition to regional mean strains in four quadrants, as shown in Figure 2-3F: (1) free edge, (2) belly region, (3) base, (4) commissures. The overall mean strains and regional strains were compared across both stiffness and geometric variables.

2.2.6 Statistical Analysis

Results are presented as mean ± standard error of the mean. All experiments conducted comprised n=5 specimens per group. Comparisons between the four stiffness groups for mechanical testing, SEM analysis, and strain mapping were made using One-Way ANOVA with

Tukey's test for post-hoc analysis. Comparisons across the two geometric configurations were made using Student's t-test.

2.3 Results

2.3.1 Valve Scaffold Characterization

2.3.1.1 Electrospun Valve Scaffold Designs

The principal difference in the geometric designs of the two electrospinning collectors was the free edge length. The free edge length of the Mk1 design was 21.9mm compared to 26.1mm in the Mk2 design. The leaflet surface areas were nearly identical at 305.2mm2 for Mk1 and 304.2mm2 for Mk2. Likewise, the commissure heights were similar at 14.8mm for Mk1 and 14.9mm for Mk2. Both Mk1 and Mk2 geometries were designed with a 23mm annular diameter.

2.3.1.2 Valve Scaffold Thickness

The thickness of the valve scaffolds after fabrication was measured before use in further experiments. Thickness maps generated from direct measurements are provided in Supplementary Figure S1. Overall mean thicknesses ranged between 239µm and 263µm, and were all within one standard deviation of the target thickness of 250µm.

2.3.1.3 Polymer Microstructure

Quantitative analysis of SEM images yielded microstructural features such as mean fiber diameter, mean pore size, and fiber orientation index. These were of particular interest due to their

influence over macro-scale mechanical behavior of the scaffold [218]. Across all four groups of differing PCL content, no significant differences were found in any of these three metrics. Results are displayed in Supplementary Table 1, and representative SEM images from each stiffness group are shown in Supplementary Figure S2.

2.3.1.4 Mechanical Characterization

Analysis of uniaxial tension showed increase in material stiffness as PCL content incrementally increased. Given the non-linear behavior of the PCUU/PCL blends, secant modulus at 10% strain was calculated as the determination of material stiffness. A stress-strain plot of uniaxial tension up to 50% strain is shown in Figure 2-4A, with the solid line representing stress-strain curves and dashed line representing secant modulus.

Biaxial tension up to 500kPa showed similar results for both CD and RD of the valve leaflet. PCL5 was the most compliant group, reaching 12.0% and 19.9% strain in CD and RD, respectively. While incrementally raising PCL content from 5% to 35% decreased maximum strain reached, its effect appeared to have diminishing returns. PCL15 reached 4.76% and 7.77%, PCL25 reached 1.62% and 2.35%, and PCL35 reached 1.14% and 1.81% in CD and RD, respectively. Significant differences of peak strain at maximum stress were observed between all groups except PCL25 and PCL35 in both directions. Plots of biaxial stress-strain are shown in Figure 2-4B for both RD (top) and CD (bottom).

Comparisons between secant moduli and tangent moduli for all PCL content groups are shown in the graph in Figure 2-4C. A significant difference in secant modulus was found between all four stiffness groups. In all PCL content groups except for PCL5, the secant modulus was significantly lower than the tangent modulus in CD. The secant modulus ranged from 3.30MPa in

PCL5 to 12.9MPa in PCL35, while the tangent modulus in CD ranged from 4.18MPa in PCL5 to 44.5MPa in PCL35.

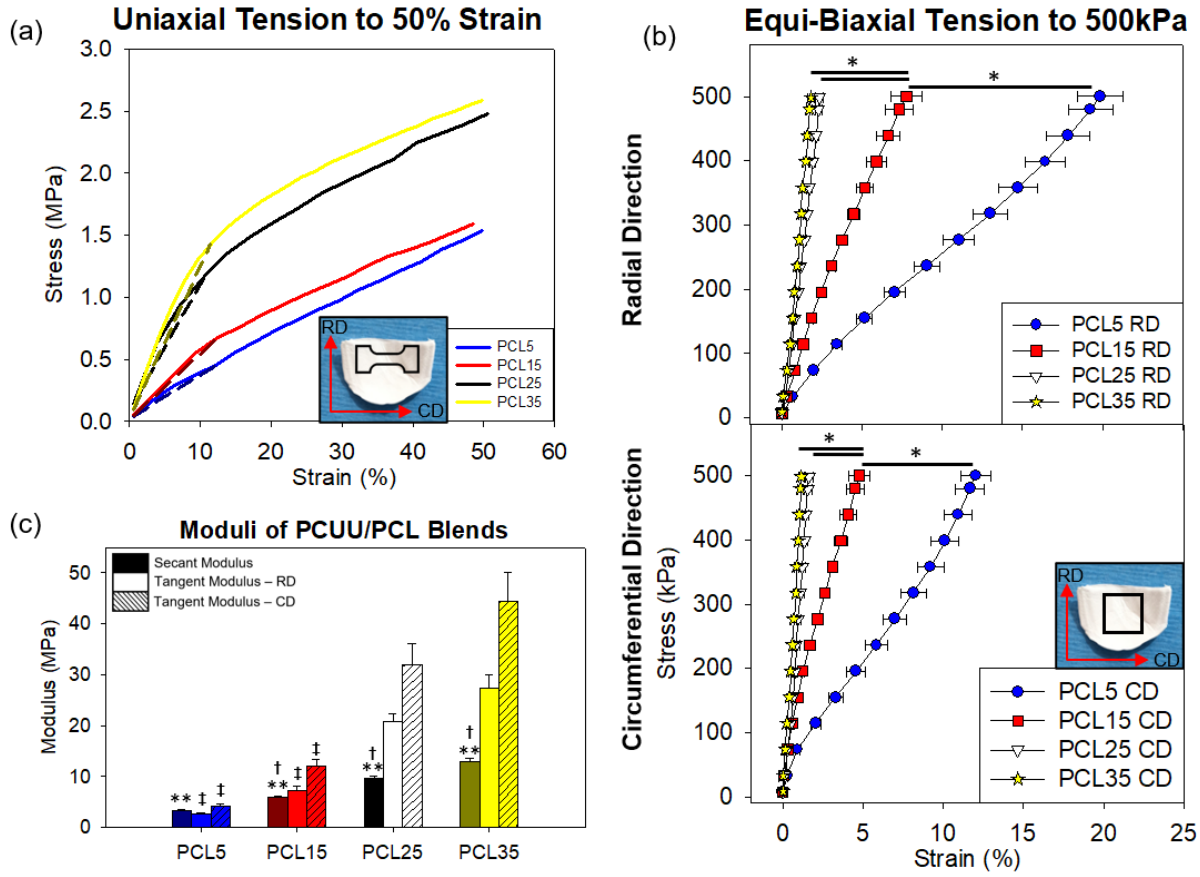

Figure 2-4. Mechanical data from (A) uniaxial tension to failure and (B) equi-biaxial tension to 500kPa for all four PCUU/PCL blend groups. (C) Comparison of secant moduli, calculated from uniaxial tensile tests, and tangent moduli, calculated from both circumferential and radial directions of biaxial tensile tests. All plots show mean ± standard error (n=5) for all groups. *Indicates significant difference ($p<0.05$) between groups indicated with bars. **Indicates significant difference ($p<0.05$) between all other secant moduli. †Indicates significant difference ($p<0.05$) between secant modulus and circumferential tangent modulus within the same group. ‡Indicates significant difference ($p<0.05$) from PCL25 and PCL35 groups. RD = radial direction; CD = circumferential direction.

2.3.2 Valve Scaffold Pulmonary Performance

Performance of scaffolds as valves in the pulmonary position was addressed by obtaining and analyzing pressure-flow curves and video of valve dynamics. Comparisons among the stiffness groups for both Mk1 and Mk2 geometries showed broad trends toward increasing ΔP and decreasing EOA and GOA as PCL content increased, with the Mk2 geometry showing the trend more clearly (Figure 2-5). However, despite the consistent trends, in all but a few cases, the differences remained largely insignificant.

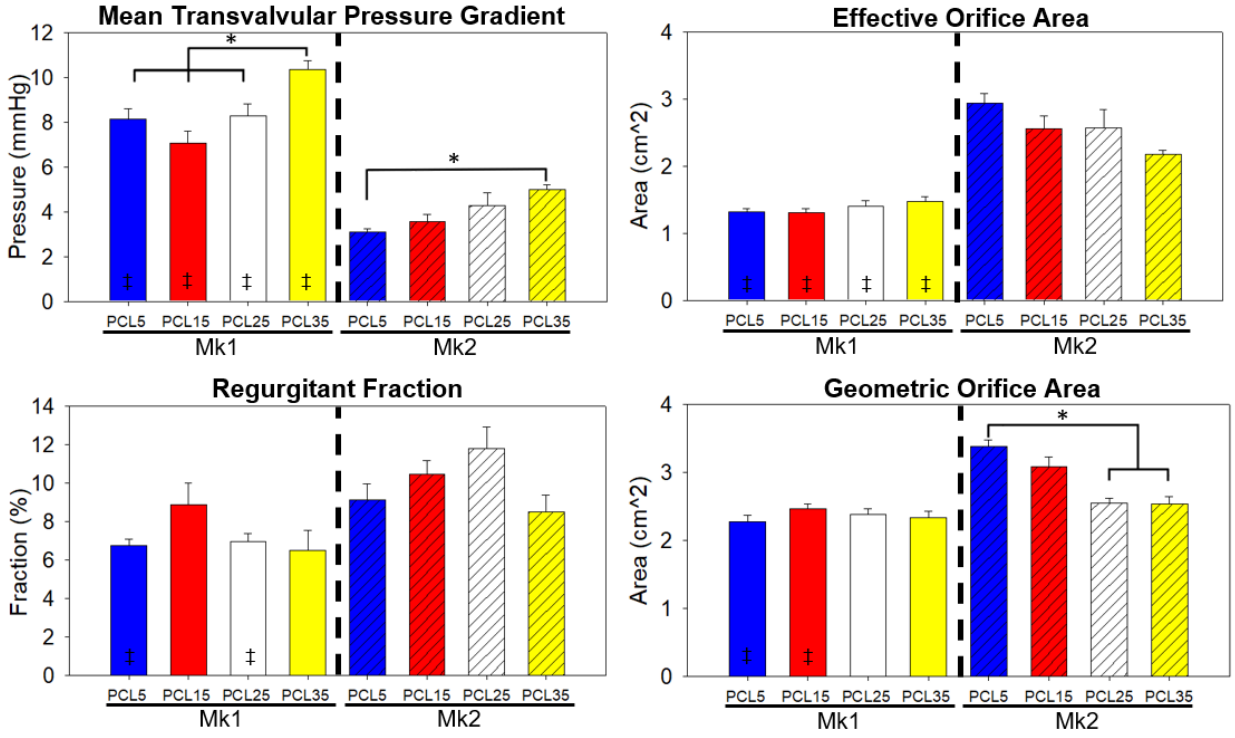

Figure 2-5. Valve performance for all four PCUU/PCL blends and both geometric configurations. Plots show averages (mean ± standard error; n=5 for all groups) of mean transvalvular pressure gradient (top left), effective orifice area (top right), geometric orifice area (bottom right), and regurgitant fraction (bottom left). *Indicates significant difference ($p<0.05$) among PCL content groups. ‡Indicates significant difference ($p<0.05$) between Mk1 and Mk2 geometries.

Contrasting the polymer composition groups across the two geometric configurations, Mk1 and Mk2 geometries showed a significant difference for nearly every metric at all PCL contents. EOA was significantly reduced among Mk1 valve scaffolds compared to Mk2 valve scaffolds for all PCL contents, while ΔP was significantly increased. GOA was significantly reduced for the Mk1-PCL5 and Mk1-PCL15 valve scaffolds, but not for PCL25 and PCL35 groups. Interestingly, regurgitant fraction in Mk2-PCL5 and Mk2-PCL25 were significantly higher than their Mk1 counterparts.

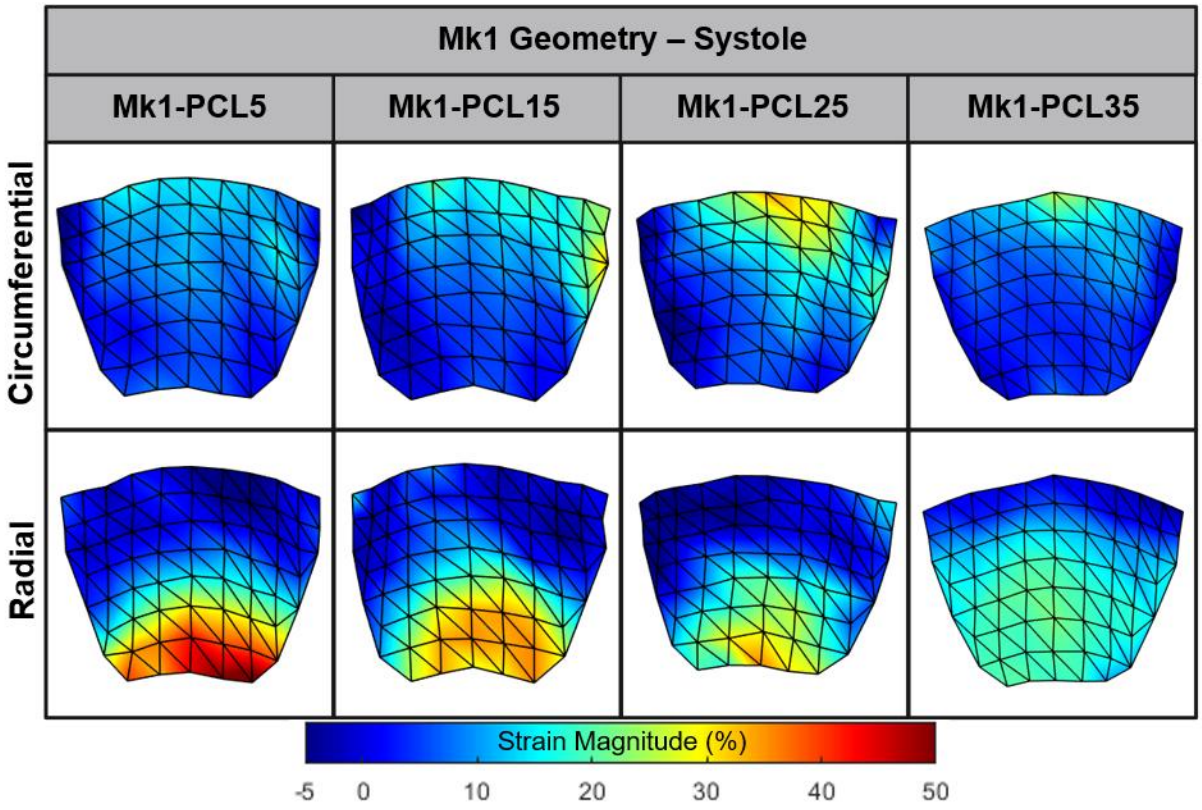

Figure 2-6. Averaged strain maps during peak systole for Mk1 valve scaffold geometry (n=5/group).

2.3.3 Strain Mapping

Uncertainties in strain calculations due to the reprojection error of the stereo camera calibration were calculated on a series of markers of known distance and yielded an average strain uncertainty of 3.2%. Averaged strain maps for peak systole in the CD and RD for Mk1 and Mk2 geometries are shown in Figs. 6 and 7, respectively. Similar strain maps for diastole are shown in Figs. 8 and 9, respectively.

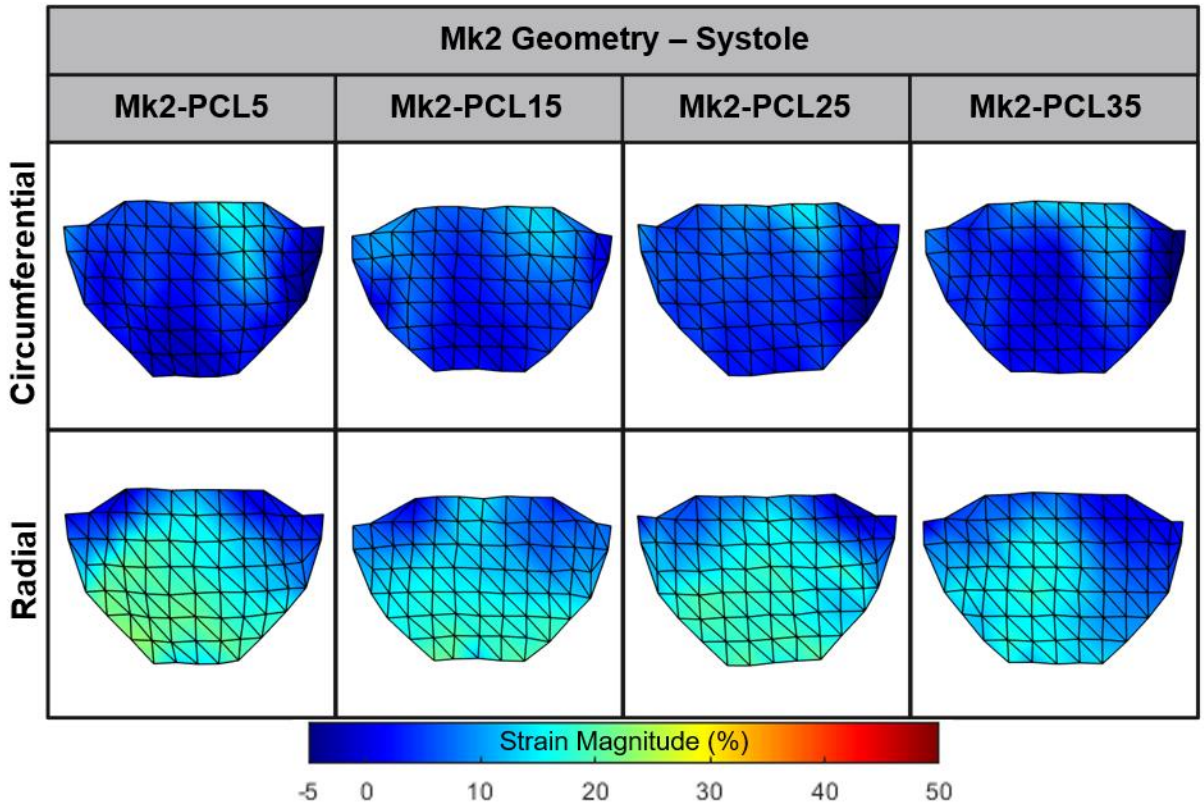

Figure 2-7. Averaged strain maps during peak systole for Mk2 valve scaffold geometry (n=5/group).

2.3.3.1 Overall Mean Strain

Overall mean strains were calculated as the average strain over all nodes making up the surface of the valve scaffold. Comparing Mk1 to Mk2 valves, the overall mean strain magnitudes

were largely similar, but strain was more evenly distributed over the surface of valves in Mk2 valves. While strain concentrations can clearly be seen in strain maps of the valve during systole, no significant differences were found across the stiffness groups in overall mean strain during systole in either Mk1 or Mk2 geometries. Overall mean strain during diastole showed nearly the same results with the exception of Mk2-PCL5-CD and Mk2-PCL35-CD, where the overall mean strain decreased significantly from 2.67% to 0.473%.

Valves experienced higher strain magnitudes in RD compared to CD at all stiffness groups, and for both geometric configurations. This effect was particularly evident during systole, where overall mean strain for Mk1 valves during systole ranged from 7.48% to 11.7% in RD and from 6.51% to 9.23% in CD. Overall strain for Mk2 valves during systole ranged from 9.74% to 13.1% in RD and from 3.62% to 5.63% in CD. Overall mean strain during diastole was near zero for all groups in both CD and RD. The overall mean strain of Mk1 valves ranged from -1.42% to 0.877% in RD and 1.22% to 2.00% in CD. Overall mean strain of Mk2 valves ranged from -2.49% to -1.20% in RD and 2.66% to 0.473% in CD. This is demonstrated in Figs. 8 and 9 by the reduction of the scale bar to a maximum of 15% strain, as opposed to the maximum of 50% for systolic strain maps.

2.3.3.2 Regional Mean Strain – Stiffness Effect

Breaking up the valve leaflet surface into distinct regions (Figure 2-3F) gave a clearer description of strain analysis. The free edge, belly, and base regions consist each of three rows of markers from top to bottom of the valve leaflet, while the commissure region is made up of the three columns of markers on both sides of the valve leaflet. Mean strains were calculated based on the nodes included in each region.

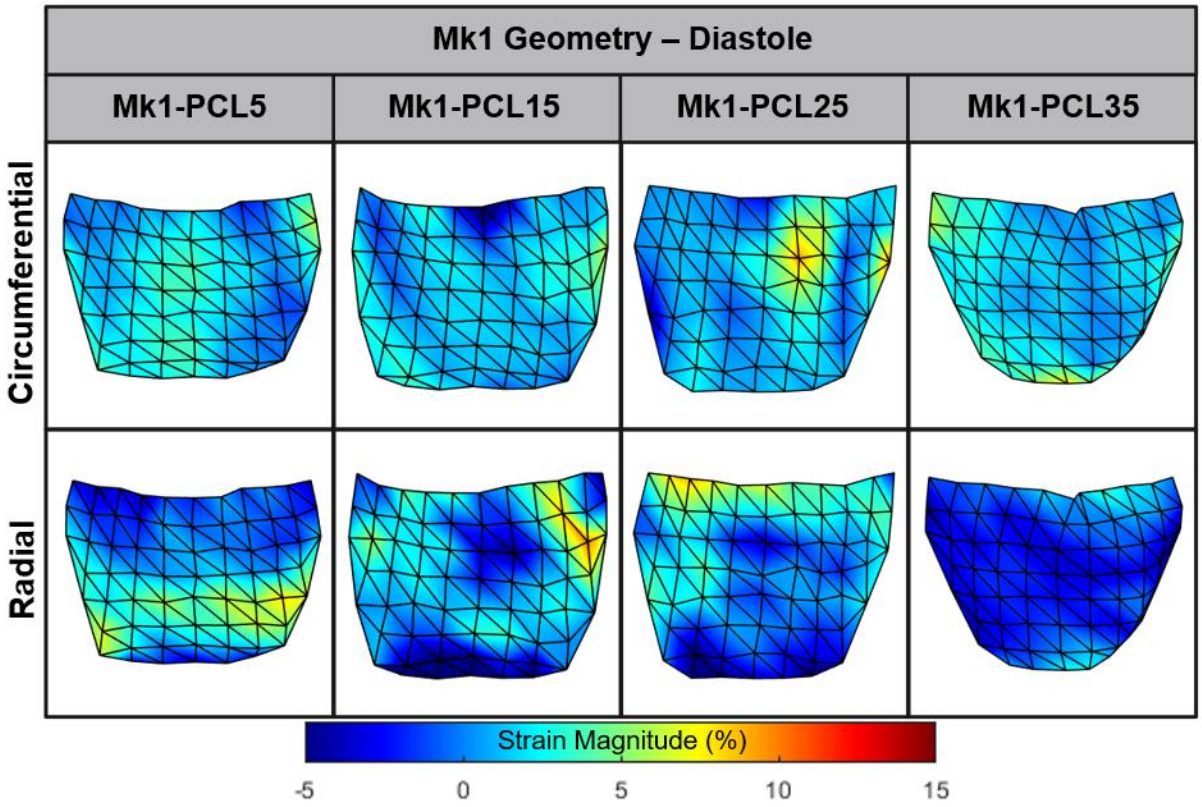

Figure 2-8. Averaged strain maps during diastole for Mk1 valve scaffold geometry (n=5/group).

The highest strain magnitudes found in all valves were concentrated in the base region of Mk1 valves during systole in RD, with Mk1-PCL5 valve scaffolds reaching 34.2% strain. This strain concentration diminished as material stiffness increased, with Mk1-PCL15 at 27.8% strain, Mk1-PCL25 at 20.8%, and Mk1-PCL35 at 18.2%, representing a significant reduction. Another strain concentration in the Mk1 valves was evident along the free edge portion during systole in CD. Mean strain along the free edge of Mk1-PCL5 was 12.2% and increased to 13.7% in Mk1-PCL15,

and 22.3% in Mk1-PCL25. This trend did not continue to Mk1-PCL35 valves, which had a mean strain of 13.4% along the free edge, though Mk1-PCL35 notably was not fully open during systole (Supplementary Video S4). This strain concentration in Mk1-PCL25 valves was a

significant increase over the Mk1-PCL5 and Mk1-PCL35 valves. Mk1 valves did not differ greatly during diastole. However, RD strain in the belly region of Mk1-PCL5 valves was 1.99%, which was significantly greater than the -2.26% of Mk1-PCL35.

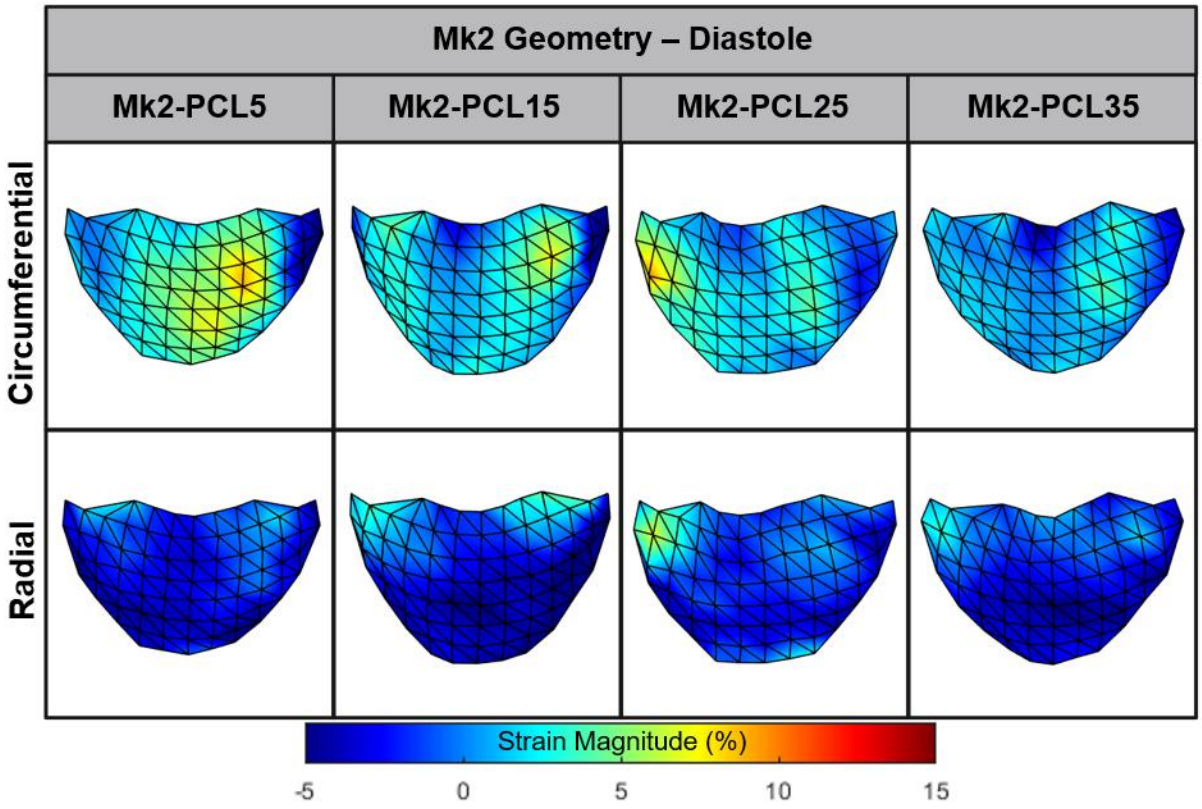

Figure 2-9. Averaged strain maps during diastole for Mk2 valve scaffold geometry (n=5/group).

Strain in Mk2 valves remained relatively static across all stiffness groups. Like the trend in Mk1 valves, strain magnitudes across Mk2 valve polymer groups seemed to diminish inversely with PCL content, but to a lesser degree. Strain in RD at the base of Mk2-PCL5 valves was 19.3% during systole, decreasing to 17.8% in Mk2-PCL15, 17.4% in Mk2-PCL25, and 13.2% in Mk2-PCL35. The differences were not significant. In fact, increasing valve stiffness revealed no significant differences in any region of Mk2 valves during systole for either RD or CD. Only during diastole did Mk2-PCL5 valves have a higher concentration of strain than Mk2 valves of

other stiffnesses. CD strain in the free edge and belly regions of Mk2-PCL5 was significantly higher than Mk2-PCL35, at 3.75% and 5.16% versus -0.06% and 1.32%, respectively.

2.3.3.3 Regional Mean Strain – Geometric Effect

There was an obvious reduction in strain magnitudes of Mk2 valves versus Mk1 valves. The main concentrations in RD and CD of systolic strain that were evident in Mk1 valves appear relatively dissipated and diffused over a greater percentage of the leaflet surface in Mk2 valves. Specifically, systolic RD strain in the base region, the area of highest strain concentration, showed a significant reduction from 34.2% in Mk1-PCL5 to 19.3% for Mk2-PCL5. The trend was similar in PCL15 valves of both Mk1 and Mk2. However, RD strain at the base of PCL25 and PCL35 valves from Mk1 and Mk2 geometries were similar. The free edge region of Mk2 valves also had a slight increase in CD strain above the overall mean, but was still significantly reduced compared to strain concentrations in Mk1 valves, and also remained relatively stable across all stiffness groups.

Diastolic strain was typically greater in magnitude for CD in the Mk2 valves, whereas Mk1 valves experienced higher strain in RD. Regionally, Mk2-PCL5 valves experienced significantly greater strain in the free edge region in CD than Mk1-PCL5, and significantly lower strain in the belly and base regions in RD. As material stiffness increased, the difference between geometric configurations diminished. However, there were still some significant differences. RD strain in the belly region of Mk1-PCL15 and the free edge region of Mk1-PCL25 valves were significantly elevated over Mk2 valves. Aside from PCL5, no significant differences were found in CD strain between the geometric configurations.

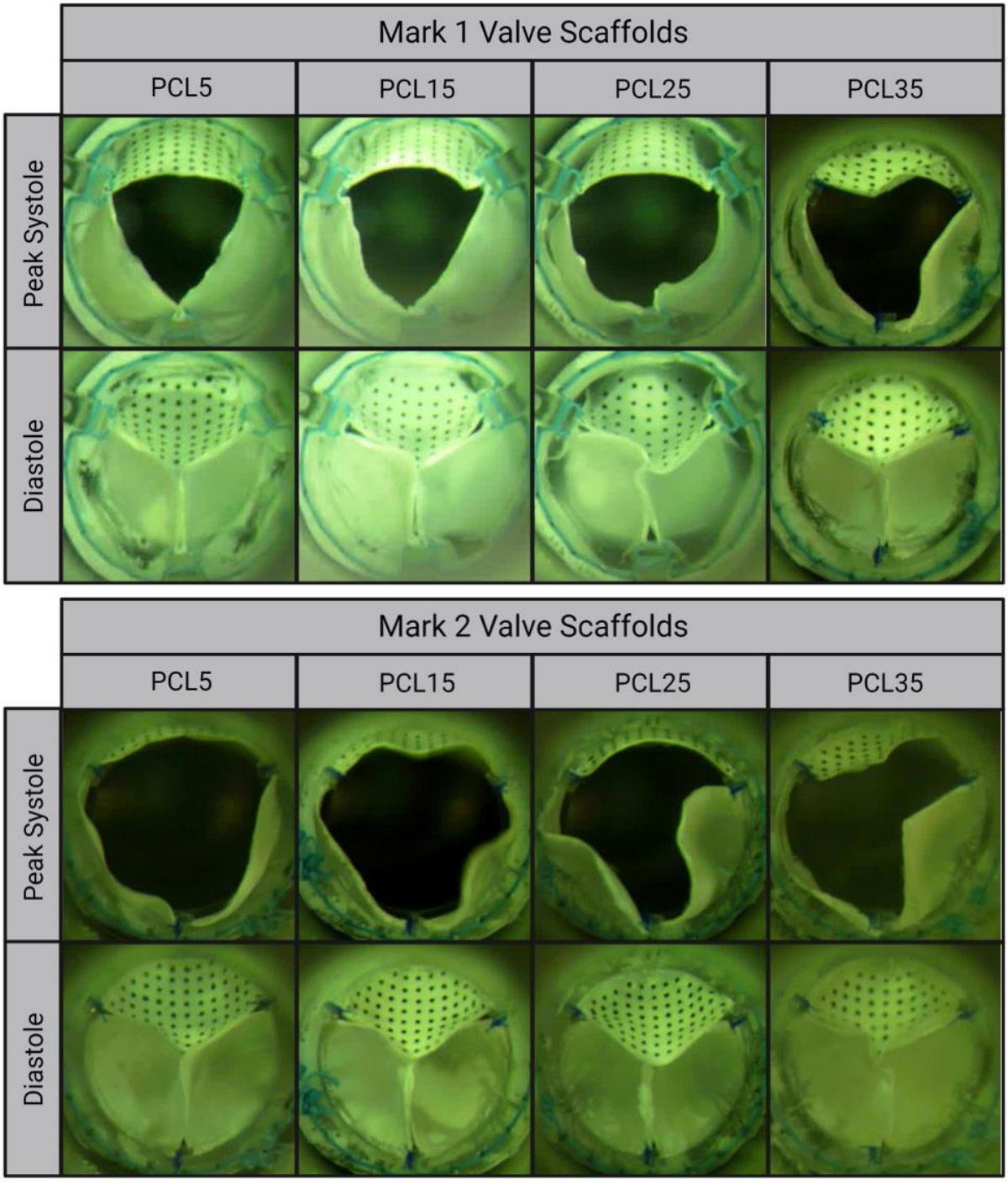

Figure 2-10. Still images of valve scaffolds from all PCUU/PCL blends of Mk1 design (top graphic) and Mk2 design (bottom graphic). Images taken at peak systole (top row of each graphic) show shape of orifice perimeter during systole as well as incomplete/asymmetric opening of the stiffer valve scaffold groups. Images taken from mid-diastole (bottom row of each graphic) show complete or near-complete coaptation of valve scaffolds.

2.4 Discussion

The clinical translation of cardiac valve scaffolds with a capacity for endogenous tissue restoration is on the horizon. The increasing number of extended pre-clinical reports have documented both good success and remaining hurdles, particularly in the longer-term as cells colonize the scaffold and form neotissue. Solutions to these challenges are being approached from engineering design perspectives to mediate short- and long-term mechanical responses. We have previously demonstrated a capacity to fabricate microfibrillar scaffolds by electrospinning deposition onto collectors shaped into cardiac valve geometries [67], and tuning scaffold mechanical properties by manipulating fabrication parameters [213], [219], [220]. In this work, we have reported an ability to influence scaffold mechanics, and subsequently valve performance, by manipulating polymer chemistry or collector design. While the primary result was to interrogate the effect of each variable on strain magnitude and distribution, a secondary outcome was the revelation of the relatively greater effect of scaffold geometry over material stiffness. The range of stiffness imparted by PCUU/PCL blending studied here was originally thought to sufficiently characterize a broad range of materials used in valve replacement. The smaller relative effect of material stiffness could indicate a hierarchy of design parameters. Taken in a broader context, design of a new generation of valve scaffold, which is certain to be founded on ever-advancing computational simulation, recently reviewed by [209], should consider the relative importance of variables influencing the structure-function relationship. The advantage of computational simulation over the study designed here is the ability to change design parameters, such as material stiffness and geometric perturbations, extending their range well beyond what can be easily achieved experimentally. That said, experimental determination of model parameters and

validation of key design parameters will continue to be an indispensable tool in the pursuit of updated engineered valve scaffolds.

Choosing the material from which valve scaffolds are produced has been the subject of great interest. Of the many criteria that should be met for tissue engineered valve scaffolds to be successful, the two broad categories that dominate interest in material choice are mechanics and biological role in endogenous tissue growth, with the latter being principal. Due to the perceived superseding nature of endogenous tissue growth in scaffold material choice, justification of material mechanics in most recent reports hinges on comparison of broad scope mechanical tests (e.g., uniaxial tension to failure) to native tissue and *in silico* models of stress/strain. Here too, we showed that bulk mechanical properties of PCUU/PCL blended scaffolds were comparable to native tissue and applicable clinical materials. The moduli in CD for the reported PCUU/PCL blends ranged from 3.3MPa for PCL5 up to 12.9MPa for PCL35 (compare to native ovine pulmonary valve in CD, and glutaraldehyde-treated bovine vein valve in CD, reported in [138]). The reason for reporting both uniaxially-derived secant modulus and biaxially-derived tangent modulus was for comparison to multiple sources. Although not strictly a comprehensive definition of directional stiffness, tangent modulus calculated from biaxial loading has been an often-reported metric of valve material stiffness, usually in isolation from uniaxially-derived modulus [68], [221], [222]. The range of tangent moduli, particularly in CD, reported here spanned a greater range than previously reported values. The 4.18MPa of PCL5 is comparable to both native human pulmonary valve tissue [222], and the bis-urea modified polycarbonate valve tested in Kluin et al. [68]. PCL35 had a tangent modulus of 44.5MPa, which is approximately 8x and 4x stiffer than the reported value for native tissue and fixed bovine jugular vein, respectively [138].

In reporting the material-level mechanics of the PCUU/PCL blends used here, it is worth noting the shape of the uniaxial curve remains relatively linear which deviates from the typical J-shape of most native tissues, including the cardiac valves. The lack of a transition to a high stiffness region dependent on strain levels could prove to be a limitation of this class of materials as currently presented. However, simple modifications to polymer processing techniques, such as concurrently electrospraying aqueous medium [218], are capable of tweaking the material mechanics to more native-like biaxial responses, and could be utilized in future iterations of strain mapping polymeric valve scaffolds.

While mimicking the material-level mechanical properties of native tissue is a desirable goal, spatial distribution and regional concentration of strain might be a more significant indicator of long-term survival of the TEHV [98]. This report showed that PCL content influenced bulk mechanical properties and reduced strain magnitudes and concentrations. However, increasing PCL content had a deleterious effect on overall valve performance, causing an increase in ΔP and decrease in orifice area. The increased mechanical stiffness of higher PCL content caused at least one leaflet on those valve scaffolds to open asymmetrically and incompletely (Figure 10, Supplementary Videos 4, 7, and 8). Which leaflet(s) had abnormal deformation during systole was not consistent and was possibly caused by small variations in thickness across all leaflets. Because markers were randomly assigned to one leaflet of each valve scaffold tested, leaflets deforming asymmetrically were randomly included in the strain analysis. Interestingly, the effect of increased stiffness causing asymmetric leaflet opening has been observed before by Sugimoto and Sacks [223]. They posited that the increased stiffness leads to abnormal dynamic motion, which could be a precursor to early valve failure.

Contrasted with PCL content, manipulating geometric aspects of the valve scaffolds had more significant implications on nearly every metric tested, from performance in the mock circulatory loop to strain magnitude and concentration. For instance, the free edge length of Mk1 valve scaffolds was not large enough to allow adequate opening during systole. The orifice perimeter during systole took on a somewhat triangular shape (Figure 10, Supplemental Videos 1-4), as opposed to a typical circular cross-section. As a result, it is theorized that this limitation in valve dynamics created an inhibition of flow, leading to locally increased pressure at the base of the valve, causing the strain concentrations seen there, most notably in the more distensible PCL5 valves. The significant reduction in RD strain in Mk2 valves can be seen as evidence supporting this claim, given the greater free edge length of the Mk2 design. However, further experiments quantifying fluid dynamics would be needed to definitively prove that fluid causes the strain concentration.

The implications that valve geometry has on valve performance are already well-stated in the literature. There is no shortage of reports from groups who have sought to model valve geometry, typically by using numerical and computational methods to parametrize valve geometry based on medical imaging data or clinically-available valve designs [92], [210], [224], [225]. Although computational modeling of valve structural mechanics, fluid mechanics, and fluid-structure interaction (FSI) have become valuable tools that are bound to improve implementation of heart valve scaffolds, there are a number of hurdles that are yet to be overcome. While there are an increasing number of advanced modeling techniques that employ isogeometric analysis that incorporate material mechanics and FSI models [88], [225], [226], most *in silico* optimization efforts focus on either minimization of stress in valve leaflets or geometric deformation in systole and diastole by manipulating a subset of variables, typically optimizing only a few geometric

features or boundary conditions [93], [95]–[97], [227], [228]. Additionally, simulated stress response to physiological loading conditions has typically not been experimentally validated, instead comparing to results reported from either past experiments or relying on results of other authors. While those models coupling material mechanics and simulated results have generally shown good agreement for bioprosthetic materials [84], models of tissue engineered valve scaffolds have yet to be fully developed and thus will require extensive experimental validation in terms of both mechanical response and kinematics under physiological conditions.

One unexpected result presented here was the greater magnitude of strain during systole than diastole. Diastolic strain magnitudes of all groups were near zero, indicating no influence of the applied load on scaffold deformation. While some strains were reported as negative (up to -2.49%), suggesting some compression of the scaffold, it should be noted that this strain level was within the strain uncertainty of 3.2%, and thus compression of the scaffold was not clearly observed. It has been shown that there is greater deformation during diastole for native tissue and bioprosthetic valves in the aortic position [86]. The simplest explanation for the contradictory results of in study could be due to the fabrication method of polymer valve scaffolds. The scaffolds tested here were fabricated such that, when mounted, their resting conformation would be in a coapted state, and thus would be less prone to deformation during diastole. Additionally, valve scaffolds experience a much lower transvalvular pressure gradient in the pulmonary position than in the aortic position. It is possible that the predominantly shear-mediated deformation during systole could create greater strain fields in the material than the pressure-mediated load during diastole. However, not enough research has been conducted on the relative strain magnitudes experienced in native pulmonary valves to verify the relative strain magnitudes observed here. Other explanations that warrant further investigation could be the mismatch of the polymer

microstructure and mechanical properties to the native valve ECM structure. While the valve scaffolds used in this study showed some degree of anisotropic behavior, the microstructure did not accurately mimic the same degree of anisotropy as in native valve tissue. As previously noted, tuning microstructural and mechanical properties of valve scaffolds has been studied at length [213], [219], [229]. As such, future endeavors in characterizing the mechanical response of these valve scaffolds should seek to optimize microstructural organization of electrospun fibers.

Several limitations to this study need to be addressed. Precision of data collection could be improved through a variety of methods. Reprojection error of 1.5pixels and a spatial resolution of 0.025mm/pixel resulted in strain uncertainty of 3.2%. Additionally, strain calculations were implemented through spatial tracking of fiducial markers on the leaflet surface. While the current method of data collection has been used often in the literature [83], [84], [86], [87], more sophisticated imaging techniques such as 3D digital image correlation using speckle patterned leaflets could improve spatial resolution and minimize uncertainty of strain magnitudes calculated from leaflet deformation. Likewise, the accuracy of the current method could be further validated by acquiring well-tested, clinically-available bioprostheses or native valves and running strain mapping experiments at both aortic and pulmonary physiological conditions. Another obvious limitation is the dynamics of leaflet mechanics tested in the current setup. The flow channel employed here was a straight, cylindrical channel of 35mm diameter, as per ISO 5840-2. A more accurate model incorporating appropriate sinus morphology, as in similar studies [223], might influence fluid mechanics and therefore load distributions in valve leaflets. Lastly, the scope of this current study was limited to only two of many variables that influence valve behavior. For instance, scaffold fabrications were based on the polymer platform (PCUU) with which we have the most experience. As such, material mechanics could be varied further by comparing PCUU-

based polymer blends to other TEHV scaffold materials [138], [139]. Additionally, the thickness of valve leaflets, as well as ECM organization, plays an integral role in strain distribution, and in native valve tissue is not uniform. Improving the design of these valve scaffolds through biomimicry would undoubtedly change the strain experienced in the valve leaflets, with the goal of recreating a more natural strain magnitude and distribution.

2.5 Conclusions

There are a number of important questions that remain unanswered for TEHV performance as the technology moves toward broad human use. The spatial strain profile of new synthetic valves is as yet untested, despite its profound implications for scaffold survival and cell recruitment in endogenous tissue growth. Strain maps of a variety of polymeric valve scaffolds are presented here for pulmonary physiological loading conditions. The outcome of manipulating design parameters of material stiffness and geometric configuration revealed a greater effect of geometric configuration on strain distribution than stiffness. The revelation of relative importance in this limited window could be expanded by manipulating other variables, from micro- to macroscale, in future iterations of scaffold designs. Additionally, computational models aimed at further improving tissue engineered heart valves and predicting mechanical and remodeling response will require extensive experimental framework, which we begin to present here. Of the many design variables important to tissue engineered valve scaffolds, the data presented in this report also serve as a call for more work to be done in this line of engineering to transition TEHVs toward the clinic.

3.0 Influence of Polymer Stiffness and Cardiac Valve Geometry on Fluid Mechanics in Tissue Engineered Pulmonary Valve Scaffold

3.1 Introduction

Some effort has been made in recent years to design valve scaffolds by utilizing computational models interrogating either structural mechanics, computational fluid dynamics (CFD) or, increasing in popularity, fluid-structure interaction (FSI). Though not an exhaustive list, several studies [95]–[97], [230] have implemented computational models with the goal of comparative analysis of different valve geometries or tweaking design parameters to optimize at least one geometric variable. In-depth review of this field, which has principally been concerned with the aortic valve, has been presented elsewhere [209]. Computational modeling offers relatively quick and more precise control over design iterations, and will doubtless be crucial to future valve scaffold design. However, despite the fact that tissue engineered pulmonary valves are advancing towards clinical translation, interest in pulmonary valve design has been limited [133]. Additionally, the major drawback preventing implementation of this approach for degradable polymeric scaffolds is the current lack of available data providing the model with accurate material parameters and experimental validation of simulated results. Specifically, there is a current gap in the literature regarding the changing fluid mechanical properties from valve scaffolds that vary by their design.

Fluid mechanics of all manner of aortic valve replacements, including mechanical, bioprosthetic, transcatheter, non-degradable polymers, tissue engineered scaffolds, and even physiological vs. pathological, have been extensively characterized experimentally typically using

particle image velocimetry (PIV) [99], [100], [103], [104], [231]–[233]. However, similar to computational models of pulmonary valve design and performance, analysis of flow profiles through the pulmonary valve and potential scaffold designs has lagged behind, only being characterized in a few instances [234]. Given the significant impact that material properties and scaffold geometry have on valve dynamics, it is hypothesized that these same variables will influence fluid flow through the valves. Specifically, from the observed asymmetric and incomplete opening of valves fabricated from stiffer materials, it is expected that resultant shear and turbulence will be worsened. Thus, it is the aim of this study to characterize flow fields of degradable polymer valves with a range of mechanical stiffness and of different geometric profiles.

3.2 Materials and Methods

3.2.1 Valve Scaffold Design and Fabrication

Cardiac valve scaffolds were fabricated using identical polymer blends and fabrication conditions used previously [235]. Briefly, valve scaffold properties were modified by changing either material stiffness or geometric configuration. Polymer valve scaffolds were based on elastomeric poly(carbonate urethane)urea (PCUU), synthesized according to established protocols [211]. Material stiffness was increased by adding incremental amounts of poly(ε-caprolactone) (PCL; Mn=80kDa, Sigma). Specifically, four groups of PCUU/PCL blends were tested, based on weight percentage of PCL: PCL5, PCL15, PCL25, PCL35.

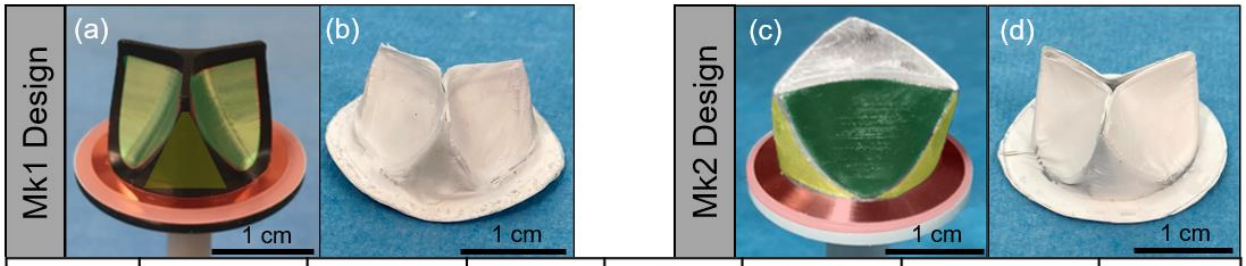

Phase	Deposition Focus	Polymer Voltage (kV)	Collector Voltage (kV)	Gap Distance (cm)	Collector Rotation (rpm)	Translational Speed (cm/sec)	Polymer Flow Rate (mL/hr)
Phase 1	Annulus	+6	-5	5	10	0	1.5
Phase 2	Leaflets	+5	-4	4	0	1	1.5
Phase 3	Overall	+6	-5	5	10	1	1.5
Phase 4	Commissures	+5	-4	4	0	1	1.5

Figure 3-1. Multi-phase electrospinning fabrication. Valve scaffold fabrications were separated into four phases focusing polymer deposition onto distinct regions of the collector mandrels meant to evenly distribute fibrous scaffold. Images of collector mandrels of both Mark 1 (Mk1) and Mark 2 (Mk2) designs are shown in (a) and (c) with regions from each electrospinning phase highlighted. Resultant valve scaffolds are shown in (b) and (d).

Valve scaffolds were produced by electrospinning each of the PCUU/PCL polymer blends onto two distinct electrospinning collector mandrels inspired by valve geometry and manufactured using double-component technology, wherein the core of the collectors comprise a metallic material and the outer surfaces and edges are covered by insulating plastic [67]. Geometric configurations were designed based on previously developed valve geometries. The first geometric configuration, termed Mark 1 design (Mk1), was based on a parametrized model of a clinically-used bioprosthetic valve [210]. The second geometric configuration, termed Mark 2 design (Mk2), was based on Thubrikar's "optimized" aortic valve model [91], modified by preserving leaflet height, free edge length, and leaflet surface area and converting the geometry to a 3-sided flat-faced collector to improve electrospun fiber deposition. Images of both geometric configurations, as well as resultant valve scaffolds, are given in Figure 3-1.

The electrospinning process was separated into 4 phases, with fiber deposition from each phase being focused to different regions of the collector mandrels. The first phase focused deposition onto the sewing ring at the base of the collectors. The second phase focused deposition onto the three leaflets. The third phase was a general deposition over all surfaces of the collectors, and the fourth phase focused deposition onto the commissural regions. A pictorial description of the valve scaffold fabrication process is given in Figure 3-1. Spatial variation in thickness was measured on all resultant valve scaffolds at 15 distinct locations on leaflet surfaces using a dial indicator pocket gage (1010MZ, Starrett).

3.2.2 Mock Circulatory Loop

The custom-built mock circulatory loop used in this study has been recently described [235]. Briefly, valve scaffolds were placed in custom mounts before loading into the mock loop. Physiological conditions for a pulmonary valve were recreated according to ISO 5840 requirements using a trapped-air compliance chamber and adjustable gate valve. The working fluid was 41% glycerin in deionized water to match the kinematic viscosity of blood in large conduits (measured at 3.48cSt). Pulsatile flow was provided by a servo cylinder (Model A1NZ9B, Ultra Motion) compressing a bellows that was not mechanically attached, allowing the simulation of passive filling in the native ventricle. Pulsatile flow was characterized by calculating the Reynolds number (Re) 1cm downstream of the valve during peak systole and the Womersley number (Wo), which are given by Equations 3-1 and 3-2, respectively:

$$\mathrm{Re} = \frac{U_{peak} D}{\nu} \tag{3-1}$$

$$Wo = \frac{D}{2}\sqrt{\frac{2\pi f}{\nu}} \tag{3-2}$$

where U_{peak} is the peak velocity calculated from the flow at peak systole, D is the valve diameter, f is the pulsatile frequency (72bpm), and ν is the kinematic viscosity of the working fluid.

Pressure sensors (Model 1501A12EZ5V5GPS, PCB Piezoelectrics) were placed up and downstream of the valve and measured right ventricular (RVP) and pulmonary arterial pressures (PAP). An in-line flow probe (ME25PXN, Transonic), connected to a TS410 flow meter (Transonic), measured instantaneous flow. Physiological parameters, such as mean transvalvular pressure gradient, effective orifice area, and regurgitant fraction were calculated from each of 10 consecutive cardiac cycles, per ISO 5840-2:2021 and averaged. Mean transvalvular pressure gradient (ΔP) is defined as the time-averaged difference between pressure curves during the positive differential pressure period (i.e., when ventricular pressure is greater than arterial pressure). Effective orifice area (EOA) is given in Equation 3-3:

$$EOA = \frac{Q_{RMS}}{51.6\sqrt{\frac{\Delta P}{\rho}}} \tag{3-3}$$

where Q_{RMS} is the root mean square of forward flow during the positive differential pressure period, ΔP is the mean transvalvular gradient as previously defined, and ρ is the fluid density. The regurgitant fraction is the ratio of backwards flow to forward flow through the valve.

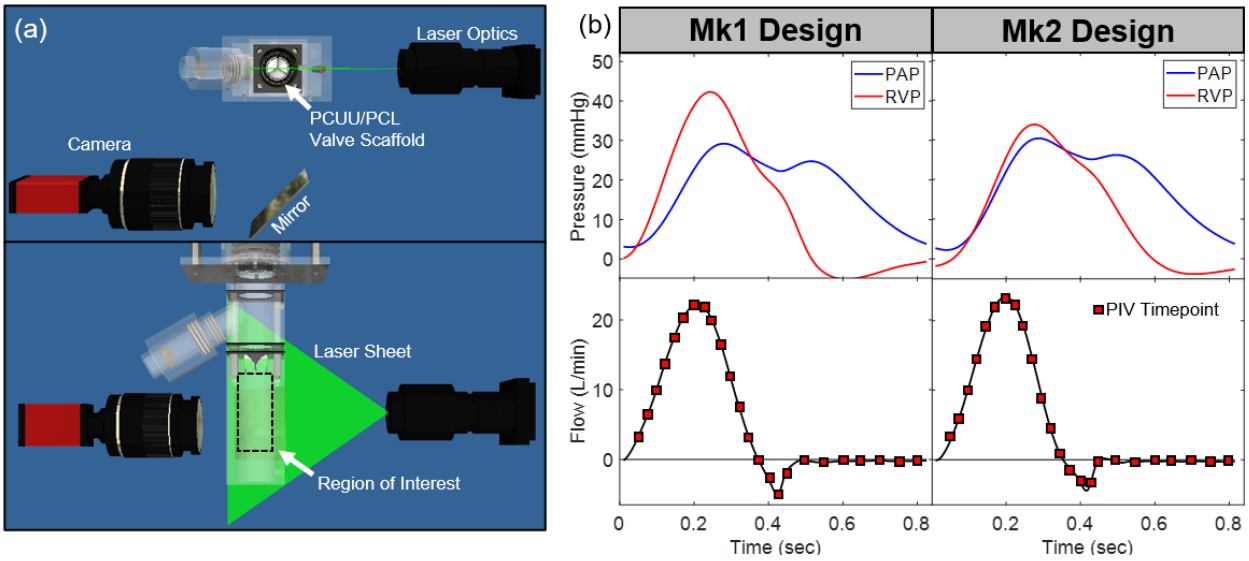

Figure 3-2. Particle image velocimetry experimental setup. (A) Schematic of laser sheet-camera-mock circulatory loop layout. (B) Representative images of pressure waveforms showing right ventricular pressure (RVP) and pulmonary artery pressure (PAP), as well as flow with PIV timepoints at 25 ms intervals indicated by red squares.

3.2.3 Particle Image Velocimetry

Particle image velocimetry (PIV) flow visualization experiments were performed using a double-pulsed Nd:YAG laser (SoloIII-15Hz, New Wave Research), spread into a laser sheet approximately 1mm thick by a combination of cylindrical and spherical lenses (Model 610026 Laser Light Sheet Optics; TSI, Inc.). The laser sheet was positioned at the central cross-section of the flow channel immediately distal to the valve scaffolds (Figure 3-2A,B). Glass spheres ranging between 9-13µm in diameter (Sigma) were seeded in the working fluid and were visualized by CCD camera (Manta G504-B, Allied Vision Technologies; spatial resolution of 20.5pixel/mm) positioned below the flow channel. Pump operation, laser pulse, and image capture were governed by a custom Labview script and were timed by an external synchronizer (LaserPulse^{TM} Model

610036, TSI Inc.). PIV image pairs were captured at 25ms intervals throughout the cardiac cycle. The time differential between laser pulses ranged from 300μs during systole to 1.5ms during diastole to capture relevant velocity field effects.

At each timepoint, 50 phase-locked image pairs were acquired and imported into an open-source Matlab application, PIVLab [236], [237]. For each image pair, a region of interest spanning the width of the flow channel (3.2cm) and with a length of 5cm, beginning 0.5cm distal to the free edge of the valve, was analyzed using final interrogation areas of 32 x 32 pixels with 50% overlap (Figure 3-3). An ensemble-average of all 50 image pairs was used for data analysis. To account for the mismatch of refractive indices between the working fluid and acrylic chamber, a grid of known dimensions was placed inside the flow chamber and a third-order polynomial fit was applied in a custom Matlab script to correct for optical distortion of the cylindrical channel.

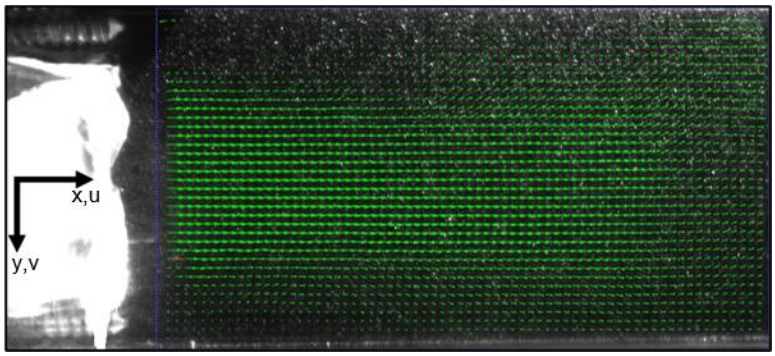

Figure 3-3. Representative image of a velocity field calculated from PIVLab within a region of interest spanning the width of the flow channel (3.2 cm) and extending 5 cm from 0.5 cm downstream of the valve scaffold.

Normal operation of the native heart valves does not lead to blood damage. However, stenosis or incomplete and asymmetric opening of any one of the valve leaflets can constrict the central jet diameter and elevate jet velocity. In these cases, characterizing velocity fields *in vitro*

can be a predictor of blood trauma *in vivo*. Shear stress is well-known to cause hemolysis and platelet activation dependent on magnitude and exposure time. Viscous shear stress (VSS), the physical force acting between layers of fluid, is calculated using Newton's law of viscosity for 2D flow (Equation 3-4) and gives a metric for shear stress magnitude experienced by the fluid under assumed laminar flow.

$$\tau(\mathrm{VSS}) = \rho\nu\left(\frac{\partial u}{\partial y} + \frac{\partial v}{\partial x}\right) \tag{3-4}$$

Vorticity (ω), defined mathematically as the curl of the velocity field (Equation 3-5), indicates rotational flow that can be an indicator of regions both of high shear and turbulent eddies.

$$\omega = \left(\frac{\partial v}{\partial y} - \frac{\partial u}{\partial x}\right) \tag{3-5}$$

Turbulence may often occur under conditions of inappropriate valve dynamics, and has been linked to blood damage *in vivo* and *in vitro* [238], [239]. Reynolds decomposition of the Navier-Stokes equations to include velocity fluctuations due to turbulence (represented mathematically by terms *u'* and *v'*) can yield relevant predictors of blood trauma such as principal Reynolds shear stress (RSS, Equation 3-6), and turbulent kinetic energy (TKE, Equation 3-7), which are mathematical formulations for the theoretical influence of eddies on changes in velocity.

$$\mathrm{RSS} = \rho\sqrt{\left(\frac{\overline{u'u'} - \overline{v'v'}}{2}\right)^2 + \left(\overline{u'v'}\right)^2} \tag{3-6}$$

$$\text{TKE} = \frac{1}{2}\rho\left(\overline{u'^2} + \overline{v'^2}\right) \quad (3\text{-}7)$$

While only theoretical proposals have been offered for a causal relationship, the well-documented history of turbulent-related blood damage, in heart valves specifically, justifies the calculation and report of turbulent metrics obtained from velocity field data.

3.2.4 Statistical Analysis

All 8 groups (4 groups based on PCUU/PCL content, 2 groups based on geometric configurations) comprised n=5 valve scaffolds per group. Statistical analyses of pressure/flow metrics and velocity field calculations were performed using one-way ANOVA between PCUU/PCL content groups with Tukey's test for post-hoc comparison and Student's t-test between geometric configurations. Results are presented as mean ± standard deviation.

3.3 Results

3.3.1 Scaffold Fabrication

Valve scaffolds fabricated with each PCUU/PCL blend and for both geometric configurations all measured within one standard deviation of the target 250 μm average thickness over the entire surface (Suppl. Figure 1). The geometric differences in the collector mandrels between Mk1 and Mk2 designs are documented in [235], but the principal difference was the free

edge length, which measured 21.9 and 26.2 mm, respectively, both having an annular diameter of 23 mm.

3.3.2 Valve Scaffold Functional Performance

Functional performance of all valve scaffolds was measured by ΔP, EOA, and regurgitant fraction (Figure 3-4). Conditions in the mock circulatory loop matched pulmonary arterial pressure (25-30 mmHg systolic pressure; 5mmHg diastolic pressure) and flow (5 L/min cardiac output), and pulsatile conditions produced Wo=16.9. Reynolds numbers ranged from 5540 to 6360 and tended to be elevated in the higher material stiffness groups (PCL25 and PCL35).

Measurements of ΔP (Figure 3-4A) revealed a consistent trend upward as material stiffness increased from PCL5 to PCL35 groups. However, a difference was only found between the less stiff (PCL5, PCL15) groups and the stiffest (PCL35) group of the Mk1 design, increasing from 9.48 and 9.78 mmHg up to 12.3 mmHg. While there was no difference among the stiffness groups of the Mk2 design, ΔP ranged from 2.75 mmHg for PCL5 to 4.17 mmHg for PCL35, consistently increasing with material stiffness. Comparing across Mk1 and Mk2 designs, there was a significant drop in ΔP at every stiffness level.

Results of EOA (Figure 3-4B) showed little effect of material stiffness. However, as with ΔP, significant differences were again found between both geometric designs for all stiffness levels. Regurgitant fraction was similar across all 8 groups tested, ranging between 8 and 12% (Figure 3-4C).

While ISO 5840-2:2021 provides minimum performance requirements only for valves on the left side of the heart, it is notable that peak RVP in the Mk1 design valve scaffolds exceeded

40mmHg which, based on the ISO, would be categorized as mildly hypertensive. By contrast, Mk2 design valve scaffolds all fell in the normotensive range.

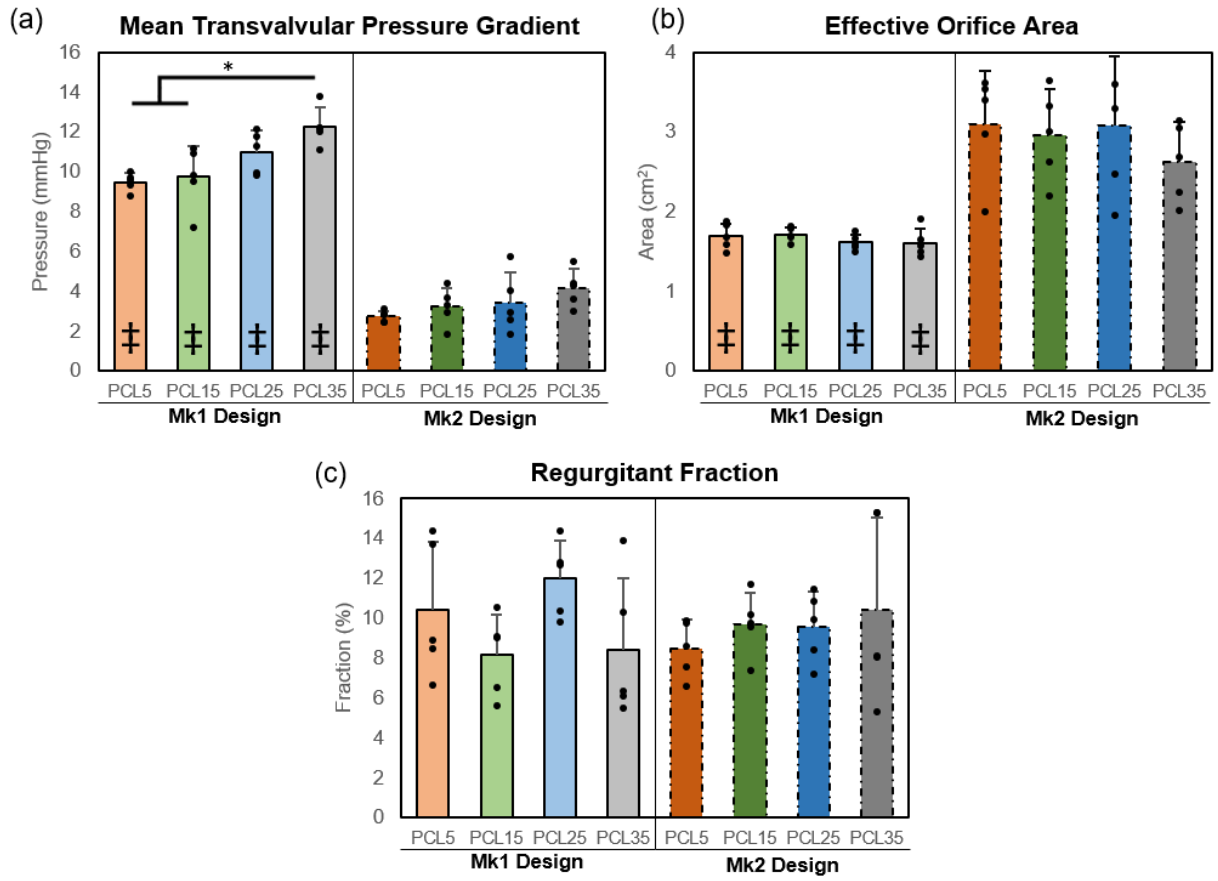

Figure 3-4. Figure 4. Valve scaffold mock circulatory loop performance metrics. (A) Mean transvalvular pressure gradient, (B) effective orifice area, and (C) regurgitant fraction for both Mark 1 (Mk1) and Mark 2 (Mk2) valve scaffold geometric designs. Error bars represent standard deviation, n=5 valve scaffolds/group. *Indicates significant difference ($p<0.05$) between groups indicated by the bars. ‡Indicates significant difference ($p<0.05$) between Mk1 and Mk2 counterparts.

3.3.3 Flow Visualization

Graphical depictions of averaged maximum values of relevant velocity field metrics at peak systole are shown in Figure 3-5. Velocity dynamics for a 250 ms period surrounding peak systole are plotted in Figure 3-6. Visual depictions of peak systolic field metrics are shown in Figures 3-7 through 3-11. Representative images were chosen to display typical behavior of fluid jets immediately downstream of the valve. In some cases of the stiffer valve groups (e.g., PCL25 and PCL35), one or more leaflets of these valve scaffolds opened incompletely or asymmetrically, causing eccentric divergence of the fluid jet.

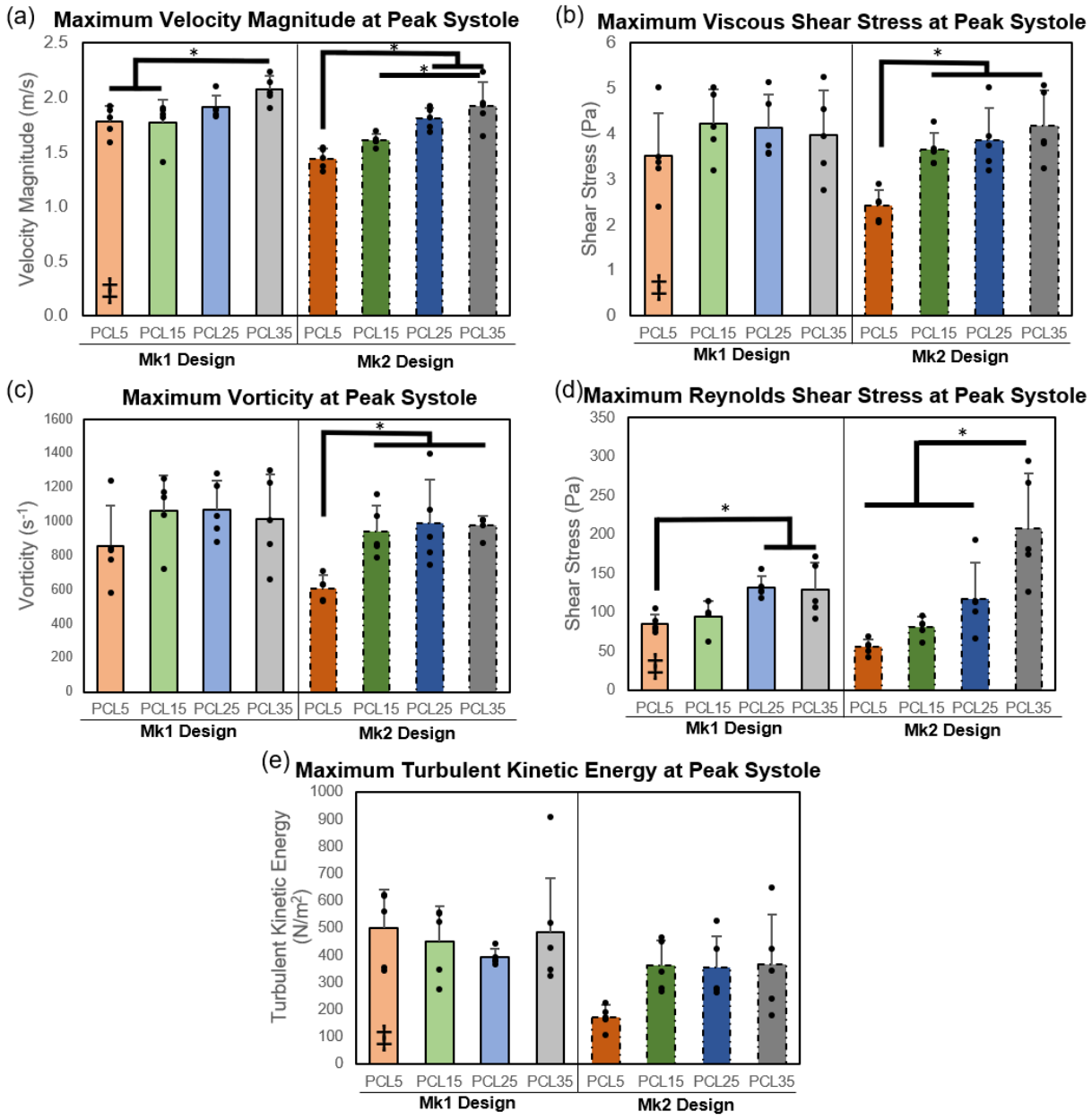

Figure 3-5. Velocity field metrics from particle image velocimetry results at peak systole for Mark 1 (Mk1) and Mark 2 (Mk2) valve scaffold geometric designs. (A) Maximum velocity magnitude, (B) viscous shear stress, (C) vorticity, (D) Reynolds shear stress, and (E) turbulent kinetic energy. Error bars represent standard deviation, n=5 valve scaffolds/group. *Indicates significant difference ($p<0.05$) between groups indicated by the bars. ‡Indicates significant difference ($p<0.05$) between Mk1 and Mk2 counterparts.

Ensemble-averaged velocity fields measured from PIV data were principally converted to velocity magnitudes. Representative images of velocity magnitude at peak systole for each of the experimental groups are displayed in Figure 3-7. From the graphic, there is an obvious reduction in magnitude of PCL5-Mk2 compared to all other groups. Quantitative comparison of the maximum velocity magnitudes at peak systole (Figure 3-5A) showed a general trend of increasing as material stiffness increased. For the Mk1 design, PCL5-Mk1 and PCL15-Mk1 were significantly lower at 1.78 and 1.77 m/s, respectively, than PCL35-Mk1 (2.07 m/s). Among Mk2 valve scaffolds, maximum velocity magnitude in PCL5-Mk2 was significantly lower at 1.44 m/s than PCL25-Mk2 (1.81 m/s) and PCL35-Mk2 (1.93 m/s). Likewise, PCL15-Mk2 was significantly lower at 1.61 m/s than PCL35-Mk2. While maximum velocity magnitude was consistently higher in all material stiffness groups of Mk1 design over Mk2, the only significant difference was the reduction of PCL5-Mk2 compared to PCL5-Mk1. By contrast, velocity during the diastolic phase showed no differences among any of the valve groups tested, with magnitudes ranging from 0.08-0.19 m/s.

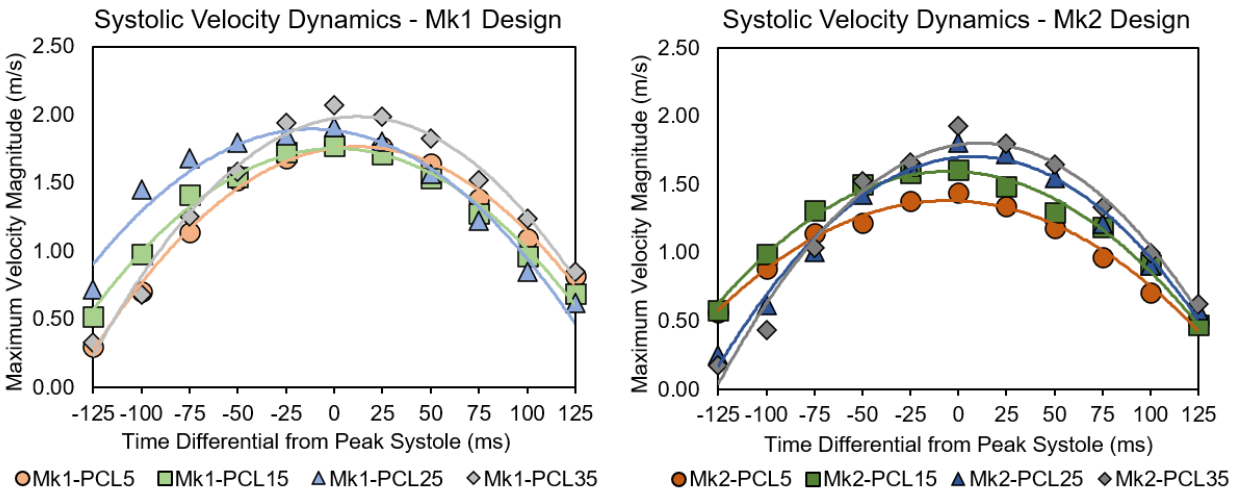

Figure 3-6. Velocity magnitudes from particle image velocimetry timepoints ranging from 125 ms before peak systole to 125 ms after peak systole. Velocity magnitude data from each group was fitted with a second-order polynomial to indicate the course of velocity changes throughout the systolic period.

Velocity dynamics during systole were tracked by plotting averaged maximum velocity magnitudes at each timepoint (Figure 3-6). Velocity magnitudes for each valve scaffold group were fitted with a second-order polynomial to describe time variation of velocity during systole. One takeaway from this graphical representation of velocity dynamics is the degree of difference in velocity magnitudes between the groups, particularly for the Mk2 design. Specifically, at 125 ms before peak systole, Mk2-PCL5 and Mk2-PCL15 displayed higher velocity magnitudes than Mk2-PCL25 and Mk2-PCL35. As previously noted, velocity magnitudes of Mk2-PCL5 and Mk2-PCL15 at peak systole were lower than Mk2-PCL35. Taking the first derivative of the second-order polynomial fit of the velocity dynamics revealed that acceleration of the fluid leading up to peak systole was significantly higher in the stiffer Mk2-PCL25 and Mk2-PCL35 groups as opposed to Mk2-PCL5. Likewise, deceleration was slower in the Mk2-PCL5 group than the Mk2-PCL25 and Mk2-PCL35 groups.

Representative images of VSS for all groups are displayed in Figure 3-8. Maximum VSS values were concentrated at the outer edges of the velocity jet, and were relatively negligible at the wall of the flow channel, except in cases of jet eccentricity. The magnitude of VSS is plotted for all groups in Figure 3-5B. In Mk1 valve scaffolds, VSS was similar for all material stiffness groups, ranging between 3.51 and 4.23 Pa. Mk2 valve scaffolds showed similar findings with the exception of PCL5-Mk2 being significantly lower than all other Mk2 scaffolds at 2.41Pa (vs. 3.65, 3.86, and 4.17 Pa for PCL15-Mk2, PCL25-Mk2, and PCL35-Mk2, respectively). Additionally, PCL5-Mk2 was significantly lower than its PCL5-Mk1 counterpart (2.41 vs. 3.51 Pa).

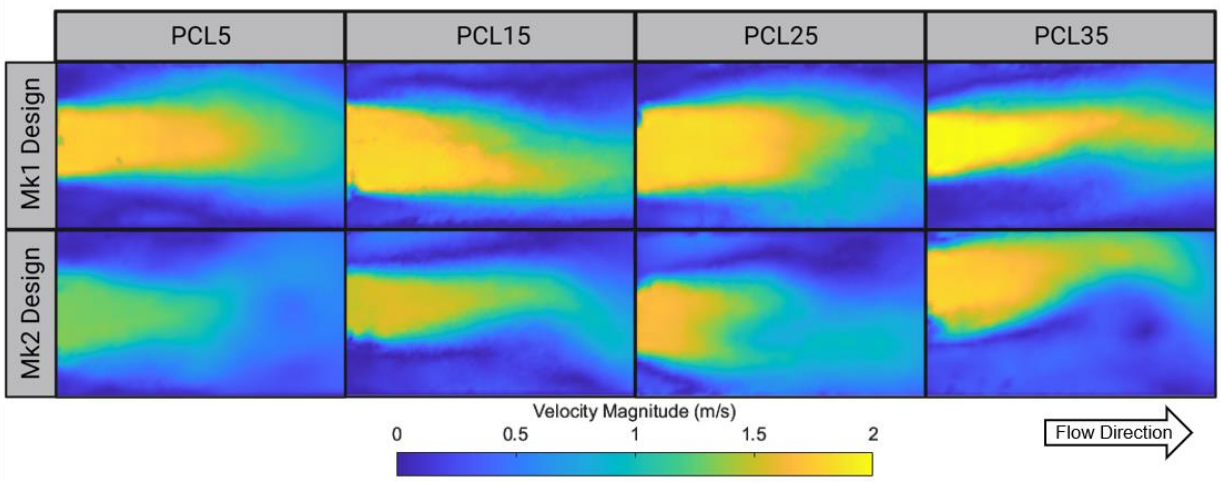

Figure 3-7. Representative averaged velocity magnitudes at peak systole.

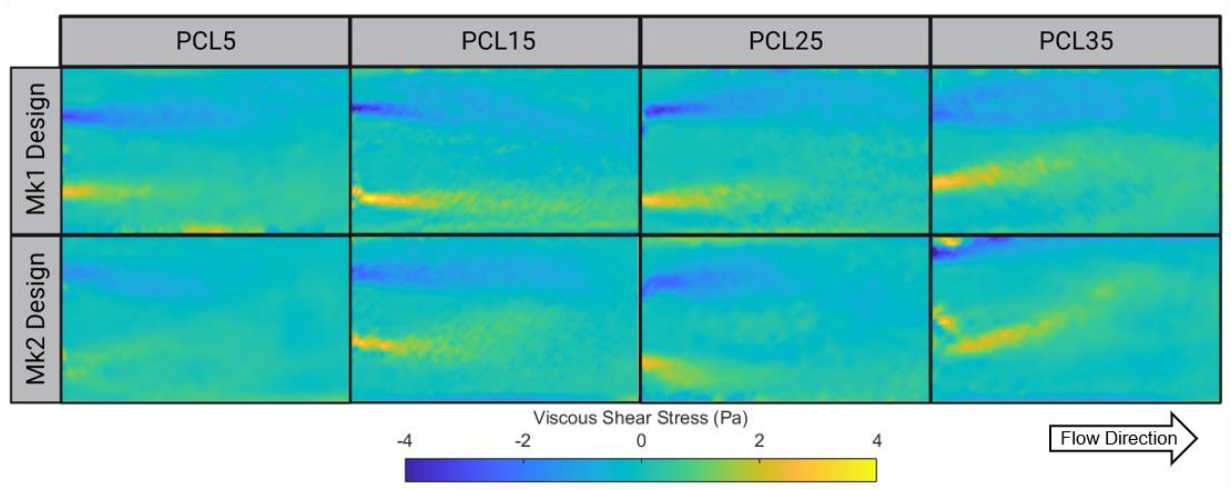

Figure 3-8. Representative averaged viscous shear stress at peak systole.

Given their similar mathematical formulations, vorticity showed substantially similar comparative results as VSS, and representative images are displayed in Figure 3-9. Once again, maximum magnitudes were located at the outer edges of the fluid jet. Plots of the maximum magnitudes of vorticity are given in Figure 3-5C. As in the plots for VSS, the only significant difference is found between PCL5-Mk2 (608 s^{-1}) and all other Mk2 groups (941, 990, and 978 s^{-1} for PCL15-Mk2, PCL25-Mk2, and PCL35-Mk2, respectively), as well as between PCL5-Mk2 and PCL5-Mk1 (608 vs. 856 s^{-1}).

Breaking down the ensemble-averaged velocity fields through Reynolds decomposition yielded information about the influence of turbulence on the fluid mechanics. Higher magnitudes of RSS, as with VSS, were concentrated at the outer edge of the fluid jet. Representative images of RSS magnitudes are given in Figure 3-10, with graphical depictions given in Figure 3-5D. Within the Mk1 design, quantitative analysis of RSS showed that PCL5-Mk1 had significantly reduced RSS magnitudes at 85.6 Pa compared to PCL25-Mk1 (132 Pa) and PCL35-Mk1 (129 Pa). The Mk2 design appeared to show increasing magnitudes of RSS as material stiffness increased, but only PCL35-Mk2 was demonstrated to be significantly elevated at 208Pa above the other three

groups (PCL5-Mk2=55.6 Pa, PCL15-Mk2=81.2 Pa, PCL25-Mk2=118 Pa). PCL5-Mk2 was once again shown to be significantly lower than its PCL5-Mk1 counterpart (55.6 vs. 85.6 Pa). All other stiffness groups were similar between Mk1 and Mk2 counterparts.

Calculations of TKE yielded mostly similar results across all groups (Figure 3-11). While it appears that PCL5-Mk2 had reduced TKE magnitudes compared to the rest of the Mk2 valve scaffolds, differences were not significant. The only significant difference among the entire cohort was between PCL5-Mk2 and PCL5-Mk1 (172 vs. 500 N/m^2).

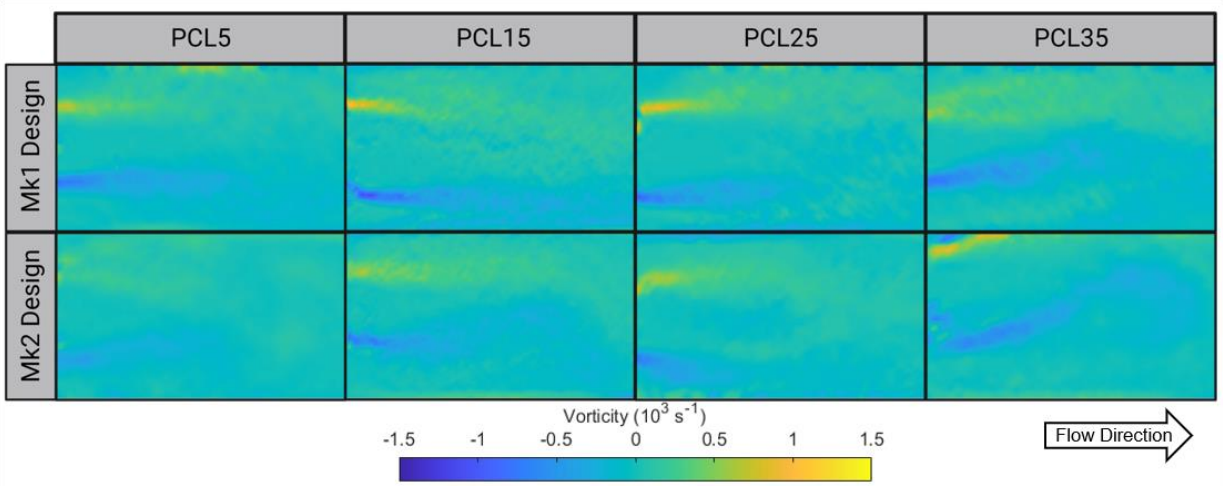

Figure 3-9. Representative averaged vorticity at peak systole.

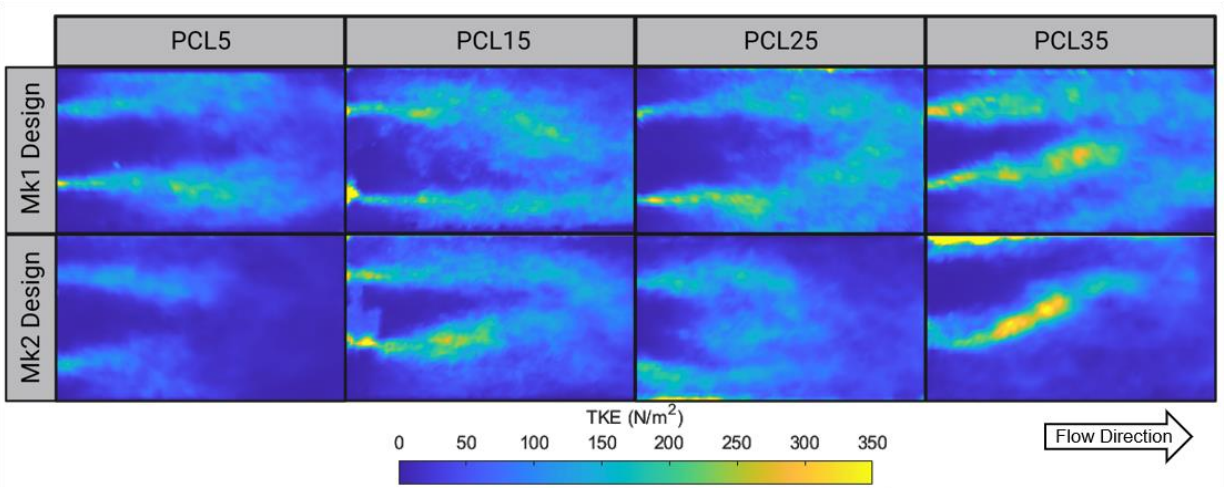

Figure 3-10. Representative averaged turbulent kinetic energy at peak systole.

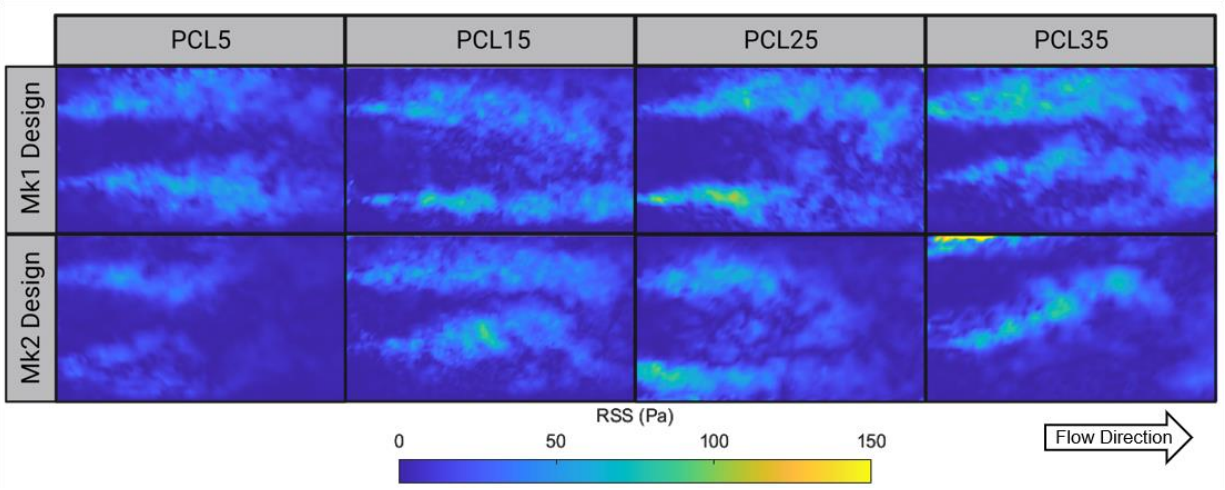

Figure 3-11. Representative averaged Reynolds shear stress at peak systole.

3.4 Discussion

Principles of valve design have a downstream effect on fluid mechanics that has not been sufficiently studied for pulmonary valve replacements. While the translation of pulmonary valve replacements seems imminent and closer than that of the aortic valve, the bulk of experimental and computational efforts at elucidating fluid flow fields remains on the left-side of the heart. The

influence of design parameters such as valve geometry and material stiffness on both the structural mechanics and the fluid mechanics is a crucial consideration for short-term performance and long-term tissue remodeling [133]. Our group has recently addressed structural mechanics dependent on valve design [235], and now report on the influence of the same material and geometric perturbations on fluid response. The results reported here show that, even within a relatively small range of material stiffness and geometry, these two design parameters had a significant impact on the velocity and shear of the fluid moving through the valves. Given the broad range of materials and geometries used in the various preclinical studies already reported, a comparative study at least of the short-term mechanics is warranted. Additionally, as valve design becomes more sophisticated through the use of predictive computational modeling, building robust and reliable material models through experimental validation will be important in future research.

Several metrics with some overlapping physical interpretations have been included here. For instance, vorticity, as a measure of rotational motion within the fluid, serves as an identifier of regions of high shear and turbulence. While calculation of vorticity at first seems redundant as a supplement to direct calculation of shear stress and estimations of turbulence, rationale for presenting vorticity calculations is to allow direct comparison to other studies reporting vorticity in isolation from other relevant parameters. Likewise, TKE and RSS are both mathematically derived from the Reynolds-averaged Navier-Stokes equations, estimating the influence of turbulent eddies on fluid movement, but their physical relevance differs. It should be noted that interpretations of both TKE and RSS only have theoretical physical manifestations on sub-Kolmogorov scales, discussed at length elsewhere [100], [240]. Even so, RSS is perhaps the most used metric for *in vitro* turbulence calculations of flow fields through heart valves, and has been repeatedly correlated with hemolysis [241]. TKE, on the other hand, is a measure of viscous

dissipation within turbulent eddies, and has been statistically elevated in various cardiac pathologies [242], [243].

In the results reported here, the most obvious observation is that of the markedly reduced velocity magnitude of the systolic jet in PCL5-Mk2 valve scaffolds. The velocity magnitude peaked at 1.44 m/s, which was significantly lower than the PCL35-Mk2 valves (1.93 m/s) and the PCL5-Mk1 valves (1.78 m/s). As increasing PCL content contributed to raising the material stiffness, it follows that valves in the stiffer groups (e.g., PCL25 and PCL35) would be less capable of opening during systole, and thus would generate asymmetric and eccentric jets and higher jet velocities. While the phenomenon of asymmetric and stenotic opening during systole was qualitatively observed in this study, this effect was quantified in our previous report [235]. Additionally, based on the velocity dynamics throughout systole (Figure 3-6), the stiffer valve scaffold groups showed elevated acceleration and deceleration, with velocity magnitudes beginning lower 125 ms before peak systole and reaching higher magnitudes at peak systole. This finding supports the conclusion that the material stiffness not only constricted the opening of these valve scaffolds, but also created a higher threshold of pressure for leaflet motion, hindering valve kinematics. As for the change across the geometric designs, the free edge length of Mk1 valve scaffolds was about 4 mm shorter than Mk2 valve scaffolds. This would obviously contribute to a more stenotic opening, generating higher jet velocities during systole.

Constricted opening of the valves during systole, caused either by reduced free edge length or elevated stiffness, likewise translated to higher values of VSS, vorticity, and RSS of stiffer Mk2 and PCL5-Mk1 valves compared to PCL5-Mk2. Levels of shear stress capable of causing blood damage have been studied by several research groups. Often cited is Hellums' compilation of shear stress vs. exposure time plot [244], which suggests a shear stress magnitude on the order of 10^4-

10^5 Pa to initiate platelet activation or hemolysis under exposure times relevant here (10^{-4}-10^{-3} sec). Measured VSS values reported here range from 2.41-4.23 Pa, well below the threshold required to induce shear-mediated platelet activation. Meanwhile, reports of RSS thresholds for causing hemolysis have offered conflicting values, which are neatly reviewed in the discussion section of the comparative analysis conducted by Jhun et al. [241]. In general, reported RSS thresholds of hemolysis range from 400-5,000 Pa. Even at the lower end of that range, the greatest RSS value reported here was 208 Pa (PCL35-Mk2) while PCL5-Mk2 was an order of magnitude lower at 55.6 Pa.

While PCL5-Mk2 recorded the lowest TKE values (172 N/m^2) and was significantly lower than its PCL5-Mk1 counterpart, there was no apparent trend across stiffness groups for either Mk1 or Mk2 valve scaffolds. The values ranged from 172 to 500 N/m^2 across all groups.

Peer-to-peer comparison of velocity field data is difficult to assess given the lack of available reports on pulmonary valve scaffold hemodynamics. In one comparable study of PIV flow field characterization through 25 mm diameter poly(tetrafluoroethylene) valves, Zhu et al. reported a peak systolic velocity magnitude of 1.33 m/s, similar to that of the PCL5-Mk2 valves reported here [234]. Likewise, RSS of the PCL5-Mk2 valves was similar to the findings of Zhu et al. at 55.6 vs. 49.2 Pa, respectively. Looking at clinical data, there is a sharp increase of the peak velocities reported in this study (PCL5-Mk2: 1.44 m/s) over peak velocities in healthy individuals (~0.9 m/s in [245], [246]), as measured by 4D magnetic resonance imaging (4D-MRI). However, comparative analysis of healthy patients and those who had undergone Tetralogy of Fallot (ToF) repair showed similar velocity values for ToF repair patients to data reported here [246], [247]. While valve scaffold design can still be improved, understanding that it is precisely this population

that would likely benefit from a tissue engineered pulmonary valve scaffold indicates a comparable level of function.

In that regard, some limitations of this study need to be addressed. The variables modified for the valve scaffold designs only included material stiffness and geometric configuration, mainly in the form of free edge length, and even these only on relatively small scales. To get a better sense of the influence valve scaffold design has over fluid mechanics, a much broader range could be included, as well as varying numerous other geometric parameters such as valve height, scaffold thickness distribution, coaptation area, etc. All of these parameters may have an impact on valve kinematics, and consequently fluid mechanics. While no trivial task, developing material models specific to polymeric scaffolds for application in computational models will improve the capacity to optimize valve scaffold design. Sophisticated models of bioprosthetic valves have already been developed using mechanical data as well as long-term clinical trends as validation [89]. An additional limitation is the relatively limited number of image pairs acquired at each time point. More accurate data analysis could be achieved with a greater number of image pairs used for ensemble-averaging and turbulence calculations. An improvement to the realism of the results obtained could have been achieved by using a more biologically-inspired flow channel consisting of pulmonary sinuses and a diameter matching that of the pulmonary artery.

While development and *in vivo* application of degradable pulmonary valve scaffolds has progressed, benchtop design optimization and experimental validation has lagged behind. Having now shown the effect that even a limited range of design perturbations has on fluid mechanics of polymeric valve scaffolds, a more complete assessment of the acute impact of implanting these scaffolds is warranted. By experimenting with a range of material properties and designs, we have presented what may serve as a beginning for the broader characterization of pulmonary valves in

the pursuit of designing more effective scaffolds. Long-term performance of tissue engineered cardiac scaffolds has been noted to change with remodeling process, so it is unclear how valve design might influence fluid behavior on such time scales. Understanding changes in valve scaffold structure, mechanics, and hemodynamics are all areas of great interest to this field that are just now beginning to be explored. In the meantime, elucidating fluid behavior by varying scaffold design is of immediate interest. Specifically, tweaking the mechanical behavior of valve scaffolds by modifying stiffness and deformability has been the goal of this paper and our previous report [235].

3.5 Conclusions

Reported here is an assessment of the fluid mechanical properties of electrospun, polymeric valve scaffolds ranging in geometric design and mechanical stiffness intended for the pulmonary position. Incremental increases in PCL content of the PCUU/PCL blended valve scaffolds had a slight impact on performance metrics such as mean transvalvular pressure gradient and effective orifice area. However, the geometric design difference was of relatively greater importance, creating significantly lower pressure gradients and effective orifice area between all Mk1 design and Mk2 design counterparts. Likewise, PIV results showed that material stiffness had a mild effect on metrics of fluid mechanics, but that geometric design appeared to have greater significance. Of all 8 valve scaffold groups tested, Mk2-PCL5 valve scaffolds showed the most promise in all metrics tested. While this study only varied two design parameters, and those to a relatively small degree, the results clearly indicate that even these parameters significantly impact valve scaffold performance and mechanics.

4.0 Strategy for Miniaturization of Valve Scaffold Design for Pediatric Use

4.1 Introduction

Pediatric valve replacement is generally not recommended due to the significant drawbacks of all available options, leading to poor outcomes [167], [206], [248]. Instead, the preferred treatment option for children suffering from congenital heart defects (CHD) or acquired valvular heart disease (e.g., rheumatic fever) requiring intervention is repair. While the goal of any valve repair, either surgical or through minimally-invasive procedures such as balloon valvotomies, is to permanently restore native function, the unfortunate reality is that most repair procedures are palliative [168], [249]. Modern techniques of valve repair are typically sufficient to allow children to grow into adulthood before valve health declines enough to require reintervention. However, the reoperation rate varies substantially depending on the valve being repaired, with the mitral valve having the highest reoperation rate during childhood [177]. Additionally, while valve repair may be preferred, there will be some cases in which valve replacement is the only viable option. The most common diagnoses in which valve replacement is required during childhood are pulmonary stenosis, rheumatic aortic and mitral valve disease, and severe bicuspid aortic valve stenosis [185], [248].

Treatment options for pediatric valve replacement are the same as in adult valves—mechanical, bioprosthetic, or allograft heart valves—but the drawbacks of each of these categories are magnified in children. The most prominent example is that of bioprosthetic heart valves (BHVs), which are not recommended for use in children due to their accelerated tendency toward calcification and structural valve deterioration [167]. Despite this, several commercial BHV

products have been tested and approved for pulmonary valve replacement in the pediatric population (e.g., Melody, Contegra, SAPIEN with Alterra Adaptive Prestent). Mechanical heart valves (MHVs) on the other hand require strict compliance with anticoagulation therapy and concomitant activity restriction, which may be more difficult to enforce in children. Decellularized allografts tend to demonstrate the best outcomes in children [195], [196], but are limited primarily by availability and cost of pre-processing [250]. As far as the pediatric population is concerned, the primary shortcoming of each of these valve replacement types is lack of growth accommodation, which can often result in prosthesis-patient mismatch. This challenge has inspired the development of living valve replacements using tissue engineering principles that allow for endogenous tissue growth.

The pulmonary valve is the valve most often needing replacement in children [177], either because of CHD affecting the pulmonary valve, as in tetralogy of Fallot (TOF), or as a result of the Ross procedure using the pulmonary autograft as an aortic valve replacement. As such, development of tissue engineered heart valves (TEHVs) intended for the pediatric population has been focused in that area. Degradable scaffolds intended for pulmonary valve replacement have only been an area of interest for a handful of groups, but those have become quite advanced, with published results from long-term large animal studies or even early clinical trials [138], [201], [202]. Despite this, reported outcomes have been less than optimal, with severe regurgitation due either to mechanical failure or leaflet shortening being reported. Clearly, strategies to replace the pulmonary valve in children would benefit from multiple approaches, testing a variety of variables. In that regard, the present work describes the adaptation of previously reported valve fabrication technology [67] to the pediatric pulmonary valve, and its subsequent functional performance.

4.2 Materials and Methods

4.2.1 Pediatric Valve Scaffold Design and Fabrication

Pediatric and adult valve scaffolds were fabricated using double-component electrospinning collectors designed using a variation on previously established methods [67], [235]. Briefly, the collector was designed using a combination of conductive metallic and insulating plastic components manufactured into the geometry of a trileaflet cardiac valve. The basis for adult valve scaffold geometric design was a parametrization of clinically-used bioprosthetic heart valves (BHVs) [210]. The pediatric valve scaffold design was geometrically similar to adult valve scaffolds, the only difference being the annular diameters, which were 16 mm and 23 mm, respectively (Figure 4-1). Polymeric valve scaffolds were fabricated from a 95:5 weight percentage ratio of poly(carbonate urethane)urea (PCUU) to poly(ε-caprolactone) (PCL). The PCUU/PCL mixture was dissolved at 12% w/v in 1,1,1,3,3,3-hexafluoro-2-propanol (HFIP; Oakwood Chemical) for the electrospinning process, which was conducted in a four-stage process. Parameters for each stage of pediatric valve scaffold fabrication are listed in Table 4-1. Those for adult valve scaffolds are listed in Table 4-2. After fabrication, scaffold thickness was measured at nine and fifteen locations on the leaflet surfaces of the pediatric and adult valve scaffolds, respectively.

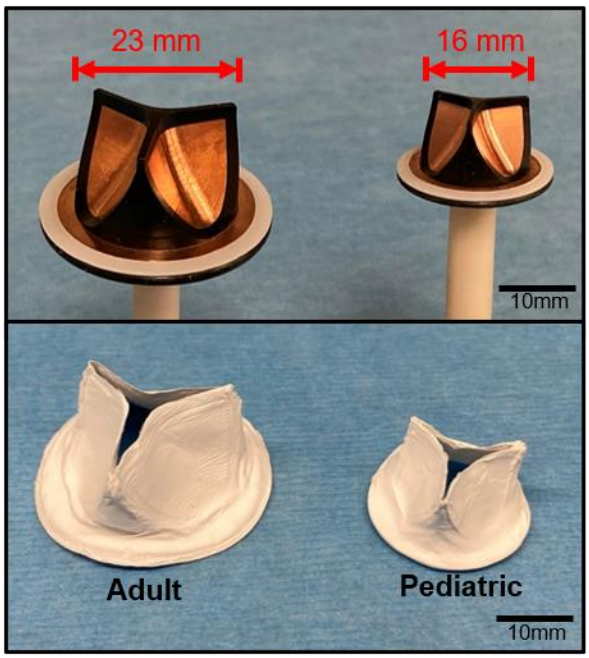

Figure 4-1. Adult and pediatric valve comparison. Electrospinning collector mandrels (top) and valve scaffolds (bottom).

Table 4-1. Fabrication Parameters for Pediatric Valve Scaffolds

	Deposition Focus	Polymer Voltage (kV)	Collector Voltage (kV)	Gap Distance (cm)	Collector Rotation (rpm)	Collector Translation (cm/sec)	Polymer Flow Rate (mL/hr)	Time (min)
Stage 1	Annulus	+6	-5	6	10	0	1.5	7
Stage 2	Leaflets	+6	-5	6	0	1	1.5	5.5
Stage 3	Overall	+6	-5	6	10	1	1.5	2.25
Stage 4	Commissures	+6	-5	6	0	1	1.5	5.25

Table 4-2. Fabrication Parameters for Adult Valve Scaffolds

	Deposition Focus	Polymer Voltage (kV)	Collector Voltage (kV)	Gap Distance (cm)	Collector Rotation (rpm)	Collector Translation (cm/sec)	Polymer Flow Rate (mL/hr)	Time (min)
Stage 1	Annulus	+6	-5	6	10	0	1.5	22
Stage 2	Leaflets	+5	-3	4	0	1	1.5	6
Stage 3	Overall	+6	-5	6	10	1	1.5	21
Stage 4	Commissures	+5	-3	4	0	1	1.5	7.5

4.2.2 Scaffold Microstructure and Mechanics

After fabrication, specimens were taken from both adult and pediatric valve scaffold leaflets for microstructural and mechanical analysis. Electrospun fiber microstructure was imaged using SEM, and fiber characteristics such as fiber diameter, pore size, and fiber orientation were quantified using a custom Matlab script that was developed previously [215]. Biaxial mechanics were measured using established methods [212], [213]. Briefly, a 10x10 mm specimen was excised from the belly region of valve scaffold leaflets, aligning the edges with the radial and circumferential directions of the leaflet, mounted into a custom biaxial tension apparatus, and loaded equi-biaxially to 500 kPa for 10 preconditioning cycles followed by 10 test cycles.

4.2.3 Pediatric Valve Scaffold Functional Performance

Pediatric valve scaffolds were mounted on custom-designed stents and placed into a mock circulatory loop designed to recreate pulmonary valve pressure/flow conditions according to ISO 5840, which has been previously described [235]. Briefly, the mock circulatory loop consisted of a trapped air compliance chamber, adjustable gate valve for resistance, reservoir, and custom-designed pump apparatus composed of a servo cylinder (Model A1NZ9B, Ultra Motion) that compressed a fluid-filled bellows. The bellows and servo cylinder were not physically attached, allowing the bellows to passively fill based on static pressure in the reservoir during the diastolic portion of the cardiac cycle. The working fluid was a 41% (v/v) mixture of glycerin and deionized water. The pump pulse rate was set at 80 beats per minute with a stroke length of 3.25 cm (providing a stroke volume of 35 mL, yielding a cardiac output of 2.8 L/min). A non-degradable polymer valve acted as the tricuspid valve between the ventricular chamber and the reservoir.

Pressure transducers (Model 1501A12EZ5V5GPS, PCB Piezoelectrics) were placed up- and downstream of the pediatric valves, and an in-line flow probe (ME25PXN, Transonic) measured real-time flow in the mock circulatory loop. Compliance and resistance elements were adjusted to produce a pulmonary arterial pressure of 20/5 mmHg. Pressure and flow waveforms were averaged across 10 cardiac cycles to calculate relevant flow parameters such as mean transvalvular pressure gradient (ΔP), effective orifice area (EOA), and regurgitant fraction. Geometric orifice area (GOA) was also directly calculated as the area encompassed by the valve orifice perimeter at the free edge during peak systole.

4.2.4 Statistical Analysis

Statistical analysis of scaffold features, such as fiber diameter and pore size, between adult and pediatric valve scaffolds for each variable used Student's t-test. Comparison of each axis of biaxial tension tests between adult and pediatric valve scaffolds likewise used Student's t-test. All tests used n=5 samples/group, and results are presented as mean ± standard deviation.

4.3 Results

4.3.1 Scaffold Properties

Average leaflet thickness of the pediatric valve scaffolds measured 0.147 ± 0.018 mm, ranging from 0.121 to 0.166 mm across 9 locations, while the average for adult valve scaffolds measured 0.252 ± 0.009 mm, ranging from 0.204 to 0.296 mm across 15 locations. Assessing the

impact of collector mandrel size and geometry on electrospun fiber morphology, analysis of SEM images of valve scaffold leaflets showed no difference in electrospun polymer fiber diameter, pore size, or fiber orientation between pediatric and adult-sized scaffolds (Figure 4-2, left panel). For pediatric and adult scaffolds, respectively, average fiber diameters were 0.53 ± 0.07 μm and 0.56 ± 0.03 μm, pore sizes were 5.07 ± 0.91 μm^2 and 3.97± 0.87 μm^2, and orientation indices were 0.54 ± 0.02 and 0.52 ± 0.02.

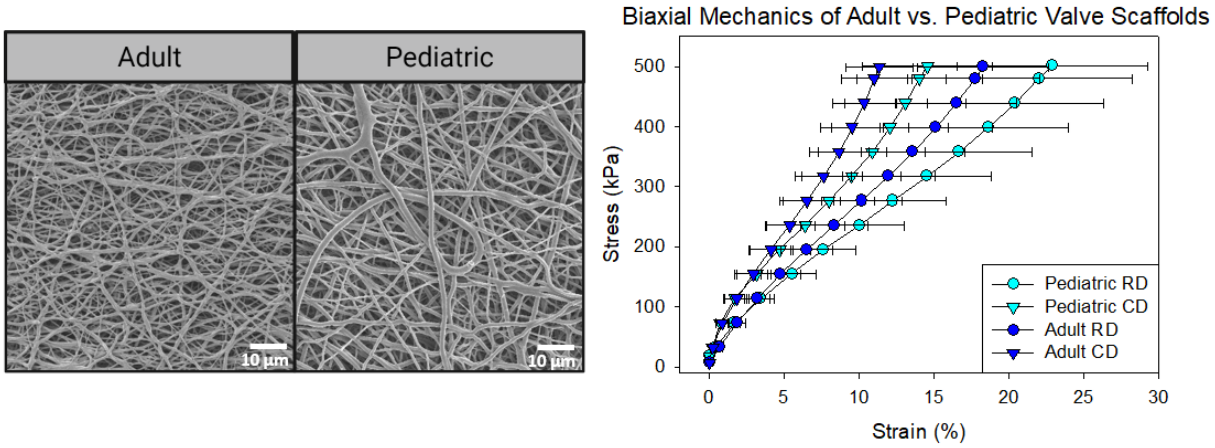

Figure 4-2. Adult vs. pediatric scaffold characterization. (Left) Representative SEM images showing polymer scaffold microstructure resulting from electrospinning onto adult- and pediatric-sized collector mandrels. No significant differences were found between resultant fiber networks. (Right) Comparison of equi-biaxial tension between adult and pediatric valve scaffolds showed no significant differences in maximum strain at maximum stress for either radial or circumferential directions (RD and CD, respectively), but in both valve scaffold groups, RD strain was significantly higher than CD strain ($p<0.05$).

4.3.2 Scaffold Mechanics

Equi-biaxial tension to 500 kPa of both adult and pediatric valve scaffolds (Figure 4-2, right panel) showed that maximum strain at maximum stress was similar in both the radial direction

(RD) and circumferential direction (CD). Maximum strains at maximum stress in the RD for pediatric and adult valves were 22.9 ± 6.36% and 18.3 ± 4.36%, respectively. In the CD, pediatric and adult maximum strains reached 14.6 ± 4.35% and 11.3 ± 2.25%, respectively. Comparing maximum strain at maximum stress between the RD and CD revealed that strain in the RD was significantly elevated over the CD for both pediatric and adult valve scaffolds ($p<0.05$).

4.3.3 Pediatric Pulmonary Valve Scaffold Performance

All pediatric valve scaffolds mounted in the mock circulatory loop were tested at relevant physiological conditions (Figure 4-3), based on a pulmonary arterial pressure set to 20/5 mmHg and cardiac output of 2.8 L/min for all five valves tested. The resultant ΔP was 8.17 ± 0.65 mmHg, and the EOA was 0.94 ± 0.08 cm^2, averaged over 10 cycles.

Short-axis imaging of the valve scaffolds showed good opening during systole. The GOA was calculated as 1.16 ± 0.12 cm^2. Both the flow waveform and short-axis imaging showed evidence of regurgitation during diastole. Regurgitant fraction, calculated from the averaged flow waveforms, was 11.37 ± 1.42%. A representative image of the valve scaffold in diastole shown in Figure 4-3 shows a small orifice at the center of the valve where the leaflets do not completely coapt.

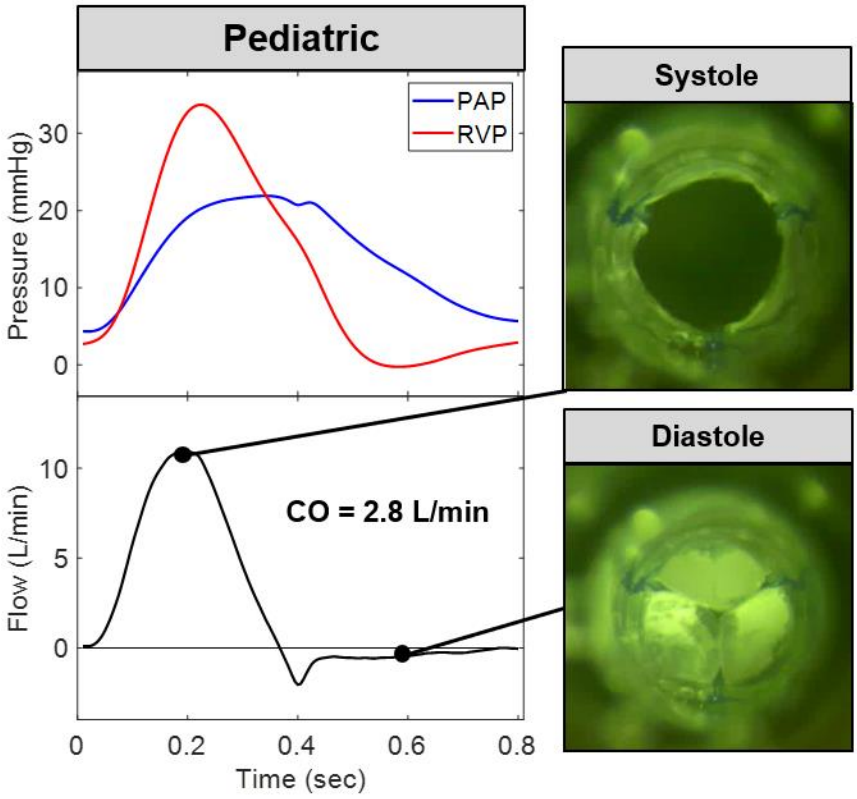

Figure 4-3. Functional performance of pediatric valve scaffolds. (Left panel) Representative pressure and flow waveforms of a typical cardiac cycle under pulmonary valve conditions. Pump parameters were programmed to generate 2.8 L/min cardiac output and 20/5 mmHg pulmonary arterial pressure. (Right) Representative short axis images of pediatric valve scaffolds at systole and diastole.

4.4 Discussion

There is an urgent unmet clinical need for a growing valve replacement in pediatric patients suffering from either congenital or acquired valve disease. Valve repair is possible and preferred in most cases, but this is largely due to the lack of a sufficient replacement. In some cases, too, replacement is inevitable. Of the handful of clinically-used replacements that exist, outcomes have been suboptimal, with early failure reported and no somatic growth accommodation possible

[167], [206], [248]. Strategies to develop TEHVs for pediatric patients are being pursued by several research groups, but only a few have produced comparable data on valve scaffold performance for pediatric-sized valves (annular diameter: 16-19 mm). However, major shortcomings of these attempts thus far in their development encourages alternative strategies comparing material, processing technique, mechanics, and functional performance.

One flaw in the initial design of the Xeltis pulmonary valved conduit (XPV-1) reported in Prodan et al. was inhomogeneity of polymer thickness in the valve leaflets, thought by the authors to be the cause of leaflet tearing and prolapse [201], mitigated in a second design (XPV-2) by adding additional material to the commissural region during the electrospinning fabrication [202]. While only a modest change, it reveals the impact of having a high degree of control over the polymer deposition during the electrospinning process. A previous study from our group, as well as the one reported here, demonstrates our ability to tightly control polymer deposition [235]. The range of scaffold thickness reported here are within 50 μm of the target thickness for the adult scaffolds and within 30 μm for the pediatric scaffolds.

Functional performance of pediatric valve scaffolds in this study showed greater average ΔP than first generation pediatric scaffolds tested in a mock circulatory loop reported by Syedain et al. [138], at 8.17 vs. 2.5 mmHg, respectively. During the 52-week growing lamb study, the authors still reported pressure gradients <10 mmHg. Conversely, the clinical pressure gradient for the XPV-2 ranged between 8 and 31 mmHg across six patients at 7 days post-implantation, as reported by Morales et al. [202]. After one year, pressure gradients in the XPV-2 remained relatively stable, ranging from 6 to 27 mmHg across five patients. While the EOA was not reported for clinical use of the XPV, the *in vitro* EOA of the first-generation valves of Syedain et al. (initial diameter: 19 mm) were 0.97 cm^2 [138], comparable to the EOA of 0.94 cm^2 in the pediatric

scaffolds tested here, despite the smaller annular diameter. Additionally, regurgitant fraction of the pediatric valve scaffolds in this study were slightly higher at 11.47% than those tested *in vitro* by Syedain et al. (8.1%).

Hemodynamic performance of clinically-used BHVs is difficult to gauge because clinical reports typically stratify groups by age instead of valve size. However, in children receiving Melody (Medtronic) transcatheter pulmonary valve replacement (TPVR), mean gradients have been reported to be around 16 mmHg with no moderate or severe regurgitation upon implantation, rising to approximately 20 mmHg after 5 years [251]. Comparison of hemodynamic performance between Contegra (Medtronic) bovine jugular venous valved conduits against pulmonary homografts after the Ross procedure has also been reported [252]. Mean gradients were similar at 15 mmHg post-implant, but rose to 40 and 38, respectively after 5 years.

The number of design variables that must be accounted for in TEHV development makes successful application a very difficult objective, even for adult-sized valves. Several studies have focused on improving geometric aspects [98], [145], optimizing stress profile [133], [228], interrogating material and mechanical properties on valve performance [235], and even modeling how material characteristics change long-term post-implantation [89]. An additional challenge in the development of pediatric TEHVs is growth potential. Balancing valve performance by ensuring unimpeded forward flow during systole while still maintaining complete leaflet coaptation during diastole (i.e., stenosis vs. regurgitation) represents a unique hurdle in a growing subject. While humans have a slower somatic growth rate than any animal model used in TEHV testing, allowing more time for recellularization, it is well-known that cell attachment and endogenous tissue growth occurs at its slowest rate towards the free edge of the leaflets [68], [132], [138], [199]. This means valve design will likely have to allow for expansion of pulmonary artery diameter before TEHV

resorption is complete. Perhaps the most extreme example to date was the growing lamb model of Syedain et al., wherein the pulmonary valve annular diameter of 19 mm in 4-month old lambs grew to about 25 mm in the 12-month study period [138]. The authors stated that the geometry of the valve was specifically designed with overcompensated leaflet coaptation length to allow for expansion of the annular diameter.

4.5 Limitations

This leads to limitations of this study that must be addressed. Primarily, this study was not adequately comparable to other pediatric pulmonary valve reports for a variety of reasons. The experimental conditions of the *in vitro* data cannot sufficiently be compared due to differences in equipment operating conditions. Moreover, hemodynamic performance *in vitro* involves many operational simplifications and therefore cannot be directly compared to *in vivo* clinical results. A direct head-to-head study between the valve scaffolds fabricated here, other pediatric TEHVs, and clinical pediatric BHVs would be a better method of comparing material characteristics and functional performance. Additionally, the pediatric valve scaffolds tested in this study are designed to be surgically implanted directly into the wall of the pulmonary artery, whereas the XPV and scaffolds reported by Syedain et al. are valved conduits, meaning there are several additional factors for valve implantation that must be considered. Interestingly, the reports by Syedain et al. and Morales et al. utilized two generations of valve scaffold design due to the failure of the first generations. The study reported here only utilized a single valve design, based on a geometry that has already been shown to have performance deficiencies [235]. A future study should consider design alterations to improve valve scaffold performance both *in vitro* and *in vivo*.

4.6 Conclusions

The development of a pediatric-sized valve scaffold (16 mm annular diameter), based on previously developed electrospinning collector mandrels, has been reported. Comparison of micro-scale electrospun fiber morphology between adult- (23 mm annular diameter) and pediatric-sized scaffolds revealed no differences in fiber diameter, pore size, or fiber orientation. Biaxial mechanical profiles between adult and pediatric scaffolds were also similar. Assessing the functional performance of pediatric valve scaffolds in a mock circulatory loop demonstrated that these pediatric valve scaffolds performed competitively with the clinical and preclinical data of the XPV and ECM-based valved conduits, but the overall valve design still requires improvement.

5.0 Continued Research and Future Directions

5.1 Design Optimization of Cardiac Valve Scaffolds

5.1.1 Computational Modeling of Cardiac Valve Performance

As discussed in Section 2.4, computational modeling of design and performance is poised to play a major role in the future development of cardiac valve scaffolds, for both biodegradable and biostable valves. Indeed, there is already a large body of literature in which *in silico* models of cardiac valves have been, and continue to be, used for both descriptive and prescriptive modeling of both clinically-used BHVs as well as newly developed polymeric valves [53], [95], [96], [230], [253]. However, since the majority of computational models focus on pericardial BHVs, constitutive model parameters for each degradable valve scaffold material must be identified independently through experimental mechanical testing.

Development of accurately predictive models of material mechanics is substantially complicated by the consideration that the driving failure mode in microfibrous TEHVs is typically not macro-scale mechanical failure, but instead is the erroneous cellular behavior during the process of cell infiltration. Therefore, an imperative in the development of structural models is definition of multi-scale mechanics, ranging from the typical macro-scale deformation down to microstructural properties of the material that will ultimately be felt by adherent cells, as discussed eloquently in Carleton et al. [254]. This was first attempted in the context of TEHVs by Argento et al. [255], wherein the authors coupled polymer microstructural features with macro-scale mechanics of a valve geometry. However, this study used a simplified constitutive model for

macroscopic stress calculations and only a representative area element of an electrospun network for microstructural modeling. While recognizing that building a robust multi-scale model is indeed a complicated endeavor, these are unrealistic assumptions that limit the applicability of this model. Fortunately, dedicated work from several groups, including our own, has offered improvements in model definition and implementation, including defining numerical approaches to simulate representative volume elements of electrospun networks, validation of microstructure based on micrographs, validation of mechanical response based on single-fiber and whole network mechanical tests, and *in vitro* cell seeding to quantify cell behavior and ECM deposition onto representative fibrous sheets [215], [254], [256]–[263]. These studies lay a groundwork to build more accurately descriptive models of multi-scale mechanics that can be translated to macro-scale geometric interrogation, representing a significant expansion of design capabilities reported in Chapters 2 and 3. The ultimate goal, if it can be reached, is to model, design, and fabricate a valve scaffold that incorporates microstructural and geometric characteristics, allowing the scaffold to navigate the biological response towards endogenous tissue restoration.

However, the ability of multi-scale models to guide valve scaffold design is only applicable insofar as realistic execution of control over microstructural characteristics of fibers electrospun onto a defined geometry can be achieved. Several publications have documented the ability to control structure-function relationship in electrospun networks by manipulating fabrication parameters onto geometrically simple collector mandrels [213], [218]–[220], [229]. Translation of this degree of control to valve-shaped collector mandrels is more problematic. For example, in the preliminary work that would finalize itself as Chapters 2 and 3 of this dissertation, influencing microstructural anisotropy in valve scaffolds by increasing mandrel rotational speed resulted in inhomogeneous polymer deposition patterns. To achieve homogeneous thickness distribution, a

slower rotational speed than could produce a biomimetic anisotropy ratio was implemented. Design innovations are currently in development to circumvent this limitation, with more discussion on this topic offered in subsequent sections.

Also, this endeavor is not without significant challenges. Indeed, there are several obstacles to this approach that currently seem insurmountable. Foremost is predicting the biological response on a cellular level. The mechanobiological cues that dictate cellular response to scaffold deformation are still poorly understood, so accurately incorporating a model of cellular response is, at present, not possible. Yet, it also may be unnecessary, at least in the practical sense of advancing toward clinical translation. Emmert et al. [133] and Motta et al. [98] have already reported that even as simple an approach as macro-scale static stress modeling of two competing valve geometries using a Neo-Hookean constitutive model to predict loading conditions *in vivo* resulted in valve scaffolds more capable of favorable tissue remodeling.

An additional challenge of modeling TEHVs is their designed degradation and the implications of degradation on loss of mechanical integrity. To model this, one area of interest that has only recently been broached by the group of Michael Sacks is the time-evolving properties of valve replacements. Zhang et al. simulated plastic strain within pericardial tissue leading to changes of the valve geometry even after only two simulated years of use [89]. This report could serve as a model for future research into the time-evolving mechanical properties of degradable scaffolds, with an important caveat that mechanisms and timing of scaffold degradation *in vivo* are not fully understood. At present, none of the degradable polymer scaffolds reported in preclinical studies have demonstrated complete scaffold resorption [69], [132], [139], and there is still very little quantitative reporting on changes to the relative load-bearing of remnant scaffold material and neotissue growth [69]. Even investigation of polymer degradation using relevant *in vitro*

models is still limited [264]. Gaining a mechanistic understanding of how the degradation process occurs (i.e., relative influence of hydrolytic, oxidative, and enzymatic degradation pathways, a material-dependent phenomenon) and relevant timescales will be an important step in developing a predictive TEHV model, and may be informed by recently reported models of growth and remodeling in polymeric vascular grafts [265], [266].

While developing a robust structural model of valve scaffold mechanics may be sufficient to predict cell behavior, the static applied loads typically simulated to predict stress/strain do not give a full representation of valve dynamics. Because the deformation of cardiac valves is mediated by shear and pressure of blood, to gain an optimal understanding of valve behavior *in silico*, it is therefore necessary to couple the mechanics of the solid domain with the fluid domain in fluid-structure interaction (FSI) models. Comparison between BHV deformation in a structural model with defined pressure load and a FSI model showed very similar mechanical response during the nearly hydrostatic load of diastole, but large discrepancies during the systolic period [226]. As mentioned in the paragraphs above, current modeling of valve mechanics is primarily accomplished by simulating diastole using simple static pressure loads on valves in a coapted state. In the context of the strain results described in Chapter 2, accurately representing leaflet load conditions for the pulmonary valve in systole is crucial. Therefore, FSI models accounting for complete dynamic behavior of valve scaffolds would be an important future direction of the research reported here.

5.1.2 Material Thickness

An area of valve scaffold design that is often overlooked is the thickness of the degradable layer. Scaffold thickness, when it is reported, is often done so only as a formality (with a few exceptions [67], [137]) and ranges substantially, usually being much greater than the native valve it is intended to replace [69], [98], [118], [134], [138], [143]. While comparative study of valve scaffold thickness has only begun to be addressed *in vivo* (see Appendix A), there is some evidence from computational and *in vitro* models showing that initial scaffold thickness has a significant impact on hydrodynamic performance [267] and structural stability during remodeling [268].

A portion of this work was dedicated to fine-tuning the electrospinning process to fabricate valve scaffolds with homogeneously distributed fiber networks resulting in an even thickness across the valve scaffold leaflets. The multi-phase fabrication process described in Chapters 2, 3, and 4 successfully demonstrated thickness distributions with small deviations. The purpose of achieving this was twofold: first, the ensure that no area of the valve scaffold leaflets would be deficient in polymer deposition as to cause early mechanical failure during testing, and second, to produce valve scaffolds that could evenly distribute the mechanical load during strain measuring. The importance of the former was recently addressed by Prodan et al. [201] and Morales et al. [202] wherein the authors described that a major design flaw in the clinical trial of the initial Xeltis valved conduit (XPV-1) was inadequate thickness in the commissural region, likely causing the valve prolapse that was reported. The solution, the authors reported, was to specifically target the commissural regions to add additional material. No explanation was offered about how that was achieved or any subsequent effects on scaffold mechanics (except for passing mention that increased thickness may inhibit leaflet flexibility), lending credence to the opening argument of this section that thickness is often overlooked as a key design parameter.

Despite the success the multi-phase electrospinning process was able to achieve in even thickness distribution, it should be noted that the thickness of native valve leaflets is not evenly distributed. Further development of this fabrication method may yield more native-like thickness distributions. Coupling thickness with microstructural and mechanical biomimicry (see Section 5.1.3) may be an avenue to achieve more consistent and optimal cell response for endogenous tissue growth. However, a major limitation of the multi-phase process is its dependence on a human operator, resulting in a lack of repeatability. To this end, an ongoing effort within our group is to construct a computer-controlled robotic electrospinning process that will be able to specifically and repeatably target deposition onto the collector mandrel. Additionally, non-uniform thickness distribution in non-degradable polymer valves has been shown to reduce stress concentrations compared to commercial BHVs [52], [269]. Thus, developing a fabrication method to reliably fabricate valve scaffolds with non-uniform thickness distributions may be advantageous in improving endogenous tissue growth and remodeling.

5.1.3 Microstructural and Mechanical Biomimicry

An avenue of design optimization long thought to be necessary for optimal tissue restoration is microstructural and mechanical biomimicry. In fact, given the importance of load-bearing in the cardiac valves, it is the physical resemblance shared between a microfibrous polymer structure and the native collagen architecture that makes electrospinning such an attractive polymer processing technique for this field. Early study into the application of electrospinning in heart valve tissue engineering demonstrated a high degree of control over microstructural characteristics that in theory could be translated to valve scaffold design [213], [218], [220], [270]. However, in reports of valve scaffold design that have advanced into preclinical and clinical study,

few have emphasized microstructural or mechanical biomimicry of the designed scaffold. On the contrary, a recent report by Uiterwijk et al. [69] argued that tissue remodeling overrules scaffold microstructural arrangement. This conclusion has been contested by other leading voices in the field [271]. Additional scrutiny of the results by Uiterwijk et al.—including the points that tissue growth occurred primarily over as opposed to within the scaffold, polymer fiber degradation had resulted in visible damage by study end, the observation of calcific nodule formation at 6 months and, perhaps most significant, the broad variability and low sample size of animals used—brings into question the reliability of this conclusion for future study. The role that cell-scaffold interface has on tissue remodeling, for VICs but also for macrophages, has been well-documented to demonstrate that erroneous immune- and mechanotransduction can cause cell response to go awry [81], [265], [272]–[274]. That is not to say that the results of Uiterwijk should be dismissed. Other applications of aligned electrospun microfibrous networks have also indicated some degree of reduction in mechanical anisotropy [275]. Yet, to the contrary, there are studies in other application areas demonstrating increasingly anisotropic mechanical behavior as tissue remodeling takes place [276], [277]. Clearly the relevance of microstructural and mechanical biomimicry deserves more intense study specific to the design and application of electrospun polymer valve scaffolds.

Methodologies for influencing microstructural similarity to collagen architecture is a current line of ongoing research. To mimic the curvilinear architecture of collagen in native valve leaflets, induction of similar structure in electrospun networks may be achieved by micro-scale topographical definition of the collector mandrel surface (Figure 5-1A,B). Preliminary data suggests that micro-scale channels in the surface of the conducting portion of the collector mandrel modulates the electric field (Figure 5-1C,D) to direct electrospun fibers to stretch across the gap, creating locally anisotropic fiber structure (Figure 5-1E).

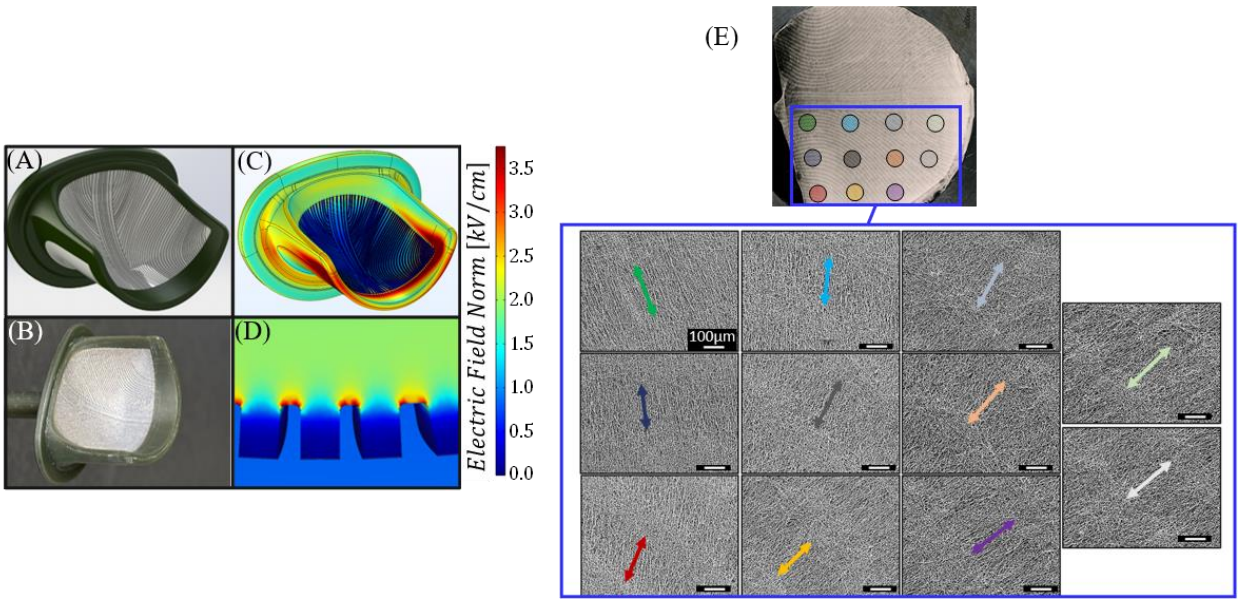

Figure 5-1. Micro-scale topographical definition of heart valve mandrel. Representation of micro-channeled collector mandrel in computer-aided design software (A) and after 3D printed manufacturing (B). In silico analysis of electric field (C) shows concentration of voltage at the edges of the gaps (D). Microstructural analysis of electrospun network demonstrates locally-aligned fibers perpendicular to designed gaps (E).

5.2 Calcification Mitigation Strategies

Calcification has been identified in preclinical reports of synthetic polymer and ECM-based degradable valve scaffolds, albeit to a significantly lesser degree than BHVs [132], [138]. It should also be reiterated that the standard ovine model is known to have accelerated calcification compared to humans. Whether calcific stenosis and mechanical failure will prove as substantial a plague in degradable polymer and ECM-based valves as in first-generation biostable polymer valves and BHVs remains to be seen. However, pursuit of calcification mitigation strategies by chemical modification to the polymer or bioactive additives is still warranted.

More complete discussion on the mechanism of calcification of BHVs has been offered in Section 1.2.2, but a simplified version of the main school of thought is that an absence of non-homeostatic cellular remains of artificial valves would remove the possibility of calcification. After calcification was seen early in polymer valves, further study identified that host response played a significant role in mediating calcification. Mechanisms of calcification in synthetic polymer valves have still not been fully mapped out, but is thought to share many similar pathways with calcific aortic valve disease [278], which in turn is characterized by chronic inflammatory response. The causes of chronic inflammatory response are manifold, and are covered in-depth elsewhere [90], but some specific targets for mitigating calcification can possibly be met through valve design. First, there is a clear correlation between calcific nodule formation and mechanical stress concentrations [27], [28], [279], and mounting evidence that mechanotransduction of cell signaling is the pertinent mechanism of calcium accumulation [280], so mechanical optimization of the valve may reduce maladaptive remodeling trending toward osteogenic differentiation of VICs [281]. Second, taking advantage of the tunability of polymer chemistry by introducing an immunomodulatory effect such as incorporating bioactive molecules into the polymer backbone may reduce activation of macrophages, VICs, and VECs. The implication of oxidative stress from chronically-activated macrophages in the progression of calcification has been increasingly appreciated [282]–[284]. Therefore, modification of the polymer chain to incorporate specific molecules that sequester reactive oxygen species (ROS) may at least slow the progression towards calcification. Specific modifications to the backbones of polyurethanes that impart antioxidant activity have already been tested in various biomaterial applications, including ascorbic acid (vitamin C) [285]–[287] and poly(thioketal urethane) [288]–[290]. Alternatively, directing macrophage behavior toward a pro-remodeling, anti-inflammatory phenotype has been achieved

in vitro with a polar, hydrophobic, ionic polyurethane [273], [274]. However, none of these modifications have been tested in a model specific to heart valves, combining relevant cell types (e.g., macrophages, VICs, VECs), and cyclic loading. Future work in valve scaffold development may consider immunomodulation a major target to facilitate optimal endogenous tissue restoration.

5.3 Implementation of Fully-Degradable Stented Valve Scaffold for Transcatheter Delivery

The main focus of this dissertation was on the mechanical characterization and design iteration of degradable polymer valve leaflets. However, the landscape of clinical implementation has shifted dramatically in favor of transcatheter delivery for BHVs and newly developed biostable polymer valves [6], [53], [56], [291]. Even recent study on TEHVs has seen initial prototype development and transcatheter deployment in animal models [68], [79], [131]. However, these latter studies have as yet only mounted degradable valves onto non-degradable stent materials. For an adult recipient, having a permanent stent with a degradable valve may not be a detriment; preclinical data only up to 6 months is currently available, so long-term conclusions cannot be drawn [68], [118]. For a child, however, inhibition of normal annular expansion during growth is one of the main detriments of current valve replacements (see Sections 1.4.2 and 1.4.3). Therefore, our group has theorized that incorporation of degradable valve scaffolds on degradable metallic stents may be worth pursuing, and has published an acute surgical pulmonary valve replacement study as a proof-of-concept to this end [136].

Most study into degradable metallic stent design and application is in the context of coronary stents. The most common degradable used in biomaterials applications historically has

been magnesium (Mg). The aforementioned pulmonary valve replacement study used the Mg alloy AZ31 (96% Mg, 3% aluminum, 1% zinc). Extensive research into Mg as a degradable stent material has revealed several impediments to its widespread use including low ductility, stress corrosion leading to early fracture, accelerated degradation rate, and accumulation of cytotoxic concentrations of ions [292]–[294]. While there are some lines of research to identify more robust Mg alloys, others are seeking alternative metals altogether such as zinc- (Zn) or iron- (Fe) based alloys to strike a balance between mechanical performance and degradation rate. The greatest concern with any metallic stent is fracturing under the compressive force and large deformation required to crimp the stent down to fit inside a catheter. In pursuit of a tradeoff, one recent study sought to design a collapsible stent combining both degradable and non-degradable components [203]. The struts were fabricated from degradable iron while the connections were a flexible Ni-Ti alloy (nitinol). Computational results showed that under simulated crimping, the major stress concentrations occurred at the nitinol connections, leaving the less ductile iron relatively unloaded. Although this was only an initial design for a stent to accommodate growth of pediatric patients, it demonstrates a potential pathway to circumvent drawbacks of totally degradable metallic stents and currently-used non-degradable stents. Continued development, including incorporating a degradable valve scaffold onto this stent design, could lead to a viable product for growing patients who are currently condemned to a series of follow-ups as growth progresses.

5.4 Endogenous Tissue Growth *In-Vivo*

Continued investigation into microstructural, geometric, and biochemical valve scaffold design also means continual preclinical investigation is necessary. One of many lessons that can

be learned from the volume of available data, including our own (see Appendix A), from ovine pulmonary valve replacement models is that subject-to-subject variability is large [69], [138], [139]. A downstream effect of this is that even if valve scaffold fabrication repeatability is high, difference in outcomes will likely still be seen. This was even demonstrated in the human trials of the XPV-1 and XPV-2 [201], [202], where mean pressure gradient and regurgitation varied widely. Thus, in the preclinical implementation of degradable valve scaffolds, the first priority ought to be improving valve scaffold design and repeatability of fabrication, followed closely by chronic *in vivo* study in sufficient numbers of animals to assess changes in biological response commensurate with changes in design. However, it is recognized that the greatest limiting factor in this goal of future study is funding. For many groups pursuing clinical translation of TEHVs, this is precisely where development ceases. Others able to overcome this obstacle have published and continue to publish reports on chronic animal study based on iterative design changes [69], [98], [131].

Future development of pediatric valve scaffolds should progress likewise, utilizing a growing lamb model [138], [143] to assess valve performance and biological response based on design optimizations. Additionally, should continued development include a degradable stented valve scaffold, it seems most appropriate to test in a juvenile, growing animal model for potential viability in pediatric patients.

6.0 Final Conclusions

Cardiac valve replacements have spanned a broad array of materials, designs, and implantation methods. Despite extensive research and development efforts, the continued lack of an ideal replacement has become a matter of debate among clinicians about who will be served best by each of the various valve designs. However, just as the official recommendations of surgical societies to balance the tradeoffs between MHVs and BHVs was becoming the de facto standard, novel transcatheter delivery systems gave sudden and dramatic rise to the absolute number and relative share of BHVs being implanted in increasingly younger patients. This despite clear evidence that BHV longevity is inversely correlated with age. The prospect of failure has also given rise to subsequent replacement strategies such as the valve-in-valve procedure. With the aim of maintaining and advancing the current paradigm of transcatheter valve replacement while extending valve durability, parallel lines of research to modify pretreatment of BHVs and develop a newer generation of durable polymer valves are ongoing.

At the same time, development of valve replacement devices for pediatric patients suffering from CHD or acquired valve disease (e.g., rheumatic disease) has been slower, given the additional challenges of valve replacement in the pediatric population. In fact, valve repair is the much-preferred course of treatment, and accounts for a majority of pediatric valve interventions. When repair is not possible, homografts are the replacement of choice for small children, when they are available, but commercial BHVs have also been developed specifically for pediatric patients. These include the Contegra bovine jugular vein valved conduit, Melody stented bovine jugular vein valve, and other, smaller versions of adult-sized replacements such as the SAPIEN. Regardless, it is understood as a sobering fact that a large percentage of children receiving

intervention for valve repair or valve replacement will likely have to undergo one or multiple follow-up procedures.

The advent of tissue engineering and its application to cardiac valve replacement continues to be a dedicated pursuit of overcoming the many limitations of current iterations of clinically-used valve replacements. However, despite the enthusiasm of TEHV development, each step toward clinical translation has been met with significant hurdles encompassing three broad categories: material, mechanical, and biological. TEHV research has been a popular target among many in the cardiovascular biomaterials community, each group proposing their own material for scaffold fabrication. Several publications exist from each of these groups documenting material properties such as cytotoxicity and degradation profile. Micro-fibrous networks are the preferred microstructural organization for valve scaffolds, given the physical resemblance of fiber networks to the native collagen architecture. From there, an increasingly sophisticated degree of research into scaffold mechanics on the macroscopic and microscopic level, and by tuning scaffold microstructure has been reported. Biological response, in these latter days of TEHV development, is typically assessed *in vivo* using an ovine model, with a primary endpoint of cellular infiltration and *de novo* ECM deposition. However, tracking cell phenotype markers of all relevant cell types to understand the stepwise process of optimal vs. maladaptive remodeling is being increasingly appreciated. As of this dissertation, no attempt at TEHV implantation has been successful in all requirement categories, even as degradable valved conduits have begun clinical trials.

In a small way, the objectives in this dissertation were designed to test requirements in each of the three aforementioned categories. In Chapters 2 and 3, material properties were modulated by blending elastomeric PCUU with incremental amounts of the relatively stiffer PCL to increase the material stiffness. Because of the influence of microstructure on macro-scale mechanics, the

microstructure was controlled between all PCUU/PCL blends tested to isolate the effects of material stiffness. Then, two different geometric profiles were designed and used to fabricate a total of 8 groups of valve scaffolds. These 8 groups were then subjected to *in vitro* testing to characterize both structural and fluid mechanics.

Chapter 2 adapted methods used by others to generate strain profiles of both native valves and BHVs. Strain profiling provides a much clearer picture of spatial deformation within the valve leaflets, especially under dynamic conditions, than the basic mechanical tests that are usually conducted (e.g., uniaxial, biaxial tension). Furthermore, strain profiling must be conducted independently for any variation in material properties, thickness distribution, microstructural organization, or valve geometry. Given the importance of stress distribution in valve leaflets for mechanical integrity, cellular response, and implication in calcification and SVD, it seems fitting that this type of analysis should serve as a model for other groups interested in TEHV development to follow, even only as experimental validation of ever-advancing computational simulations toward optimized designs.

Following with the discussion on computational modeling of cardiac valve scaffolds (Section 5.1.1), it was intended that the methodologies developed to measure strain profiles and fluid velocity field data in Chapters 2 and 3 would serve as a framework to couple computational design with experimental validation. The outlook has been shared throughout this dissertation that computational efforts will not only accelerate improvements to end-stage valve remodeling, they will in fact be indispensable in guiding valve design toward that end. It can already be seen from other groups advanced in TEHV research that design changes to valve scaffolds are currently made based almost exclusively on intuition and anecdotal experience, and still show signs of limitations in animal models and in humans. Additionally, as was demonstrated in the research above, the

degree to which design parameters can reasonably be changed and tested experimentally is limited by time and resources, whereas these changes and the effects they will have on valve performance can be interrogated much faster and more accurately in a simulation. The main caveat to this is the dependence on model reliability, meaning experimental validation will be an integral portion of valve development for the foreseeable future. Initial development of reliable, advanced FSI models to simulate real valve loading will be based heavily on experimental efforts.

Biological response is currently being assessed in the PCUU-based valve scaffolds using an ovine model of surgical pulmonary valve replacement. The latest results are provided in Appendix A. The main hypothesis being tested is how much impact initial scaffold thickness has on valve performance and cellular infiltration. With broad variability being assessed in the explants and a low sample size, conclusions on functional performance are difficult to make. Based on echocardiography alone, no worsening in performance was observed in scaffolds between 120 μm (native ovine PV thickness) and 240 μm, but substantial thrombus formation did occur in the commissures of 240 μm valve scaffolds after 30 days. After 90 days, 240 μm valve scaffolds demonstrated the most neotissue formation and a slight amount of cellular infiltration around the hinge region of the valve leaflets. Two main takeaways from our present experience *in vivo* are the substantial subject-to-subject variability and the need for updated valve designs; two of the same lessons having recently been learned by several other groups. While there is a possibility of developing computational models that incorporate cellular response into valve deformation, as has recently been attempted in vascular grafts (see Section 5.1.1), currently the most reliable method of testing how well valve scaffolds meet biological criteria is increasing numbers of chronic animal studies.

Each of the preceding four paragraphs could be equally applied to scaffolds intended for both adults and children, with only slight adaptation in the approach. The main variable differentiating the two is size, whereas geometry and scaffold microstructure can likely remain the same. Hemodynamic loading may also change based on differences in valve kinematics caused by changes to heart rate, cardiac output, systolic duration, and pressure with age. Biological response in a juvenile model will likely prove to be the most unpredictable, and will again require extensive *in vivo* experience.

Optimization of valve design will be the most highly pursued goal of TEHV research in the coming years, with simultaneous effort to commercialize a viable product, as has been the case with the Dutch-based company Xeltis. However, the technology platform developed and used in the work presented here represents a highly customizable approach to design change and experimental testing. Ongoing efforts to expand our group's capacity to design and manufacture collector mandrels, fabricate valve scaffolds, and experimentally test them in-house are powerful steps to streamline production capacity, but can also be easily supplemented by a computational approach that aids in manipulating design features prior to scaffold fabrication. The work presented in this dissertation can be seen as a small but essential step in the larger process of product design and refinement, with the ultimate goal of generating a degradable cardiac valve scaffold that serves as a curative solution to valvular heart disease.

Appendix A *In Vivo* Assessment of Stented, Degradable Polymeric Valves in an Ovine Model

Appendix A.1 Introduction

While several crucial factors must be considered in TEHV development, the paramount biological response to TEHVs is the defining criterion for success. In many ways, biological response is the first and final hurdle in the course of TEHV development. Early-stage research of material candidates typically begins with *in vitro* cytotoxicity testing to ensure basic biocompatibility. Successful clinical translation of TEHVs requires demonstration of sufficient cell infiltration and neotissue formation competing with material degradation profile. However, *in situ* cell infiltration is vastly more complicated than early-stage *in vitro* study, comprising many different cell phenotypes, biological milieu, and a dynamic mechanical environment. Indeed, early failure of TEHVs is reported frequently, and is often attributed to aberrations in the remodeling process [107]. For this reason, *in vitro* and *in silico* study of the myriad valve design parameters have been employed to influence mechanical behavior to improve remodeling prospects [133].

Several different approaches to TEHV development have been undertaken by a handful of research groups and span materials ranging from decellularized ECM to synthetic polymers like supramolecular 2-ureido-4[1H]-pyrimidone (UPy) [68], [132], [134], [138], [143]. Long-term ovine studies of each type of these materials have demonstrated early failure, often in the form of leaflet shortening leading to valve insufficiency [118], [131], [143]. This failure mode is thought to be initiated by differentiation of fibroblasts to contractile myofibroblast phenotype [133]. However, one factor that is not often considered in these studies is the initial thickness of the

implanted scaffolds. Thickness values for valve scaffold leaflets of comparable pulmonary valve replacement studies are infrequently reported. Those that are tend to be at least 2- to 3-fold greater than native pulmonary valve leaflet thickness (approximately 120 μm [67]). Therefore, our group sought to implant degradable polymeric valve scaffolds in an ovine model at two leaflet thickness designations, 120 μm and 240 μm, to understand the effect of thickness on cell infiltration, tissue encapsulation, and functional performance *in vivo*.

Appendix A.2 Materials and Methods

Appendix A.2.1 Polymer Valve Scaffold Preparation

Polymeric valve scaffolds were fabricated according to previously established protocols [235]. Briefly, poly(carbonate urethane) urea (PCUU) and poly(ε-caprolactone) (PCL) were blended at a 95:5% weight ratio and dissolved at 12% (w/v) in 1,1,1,3,3,3-hexafluoroisopropanol (HFIP). Polymer solution was electrospun onto a double-component electrospinning collector mandrel which have been previously described [67]. The electrospinning process utilized the four-stage approach, described elsewhere [235], for targeted deposition on different locations of the mandrel to achieve uniform polymer thickness. Deposition times were adjusted to obtain appropriate polymer thickness values. Target thickness was divided into two groups: 120 μm and 240 μm. Thickness was measured at 15 locations on all valve scaffold leaflets using a dial indicator pocket gage (1010MZ, Starrett).

After electrospinning fabrication, each valve scaffold was mounted onto a stent (Appendix Figure 1), similar to previously reported protocols [136]. Briefly, valve scaffolds were attached,

using 5-0 polypropylene suture, at three locations on the annular sewing ring (midway between commissures) and at each commissure, onto stainless-steel stents (diameter: 23 mm) that had previously been dip-coated five times in 2% (w/v) PCUU in HFIP. The stented valve scaffolds were then sterilized with ethylene oxide prior to animal implantation.

Appendix A.2.2 Surgical Pulmonary Valve Replacement in an Ovine Model

All experiments described in this Appendix were approved by the Institutional Animal Care and Use Committee of the University of Pittsburgh (protocol number: 22061301). Animals were cared for in accordance with the Guide for the Care and Use of Laboratory Animals as published by the National Institute of Health.

Sheep ranging between 60-70 kg were obtained and assessed preoperatively by veterinary staff. Anesthesia was induced by intravenous ketamine and Midazolam, and maintained with inhaled isoflurane. Animals were monitored throughout the procedure with EKG, pulse oximeter, and rectal thermometer. A left thoracotomy was performed to access the heart and great vessels. Heparin was administered systemically to an activated clotting time (ACT) greater than 420 seconds and cardiopulmonary bypass (CPB) was established through aortic and right atrial cannulation. During beating-heart CPB, the pulmonary artery was incised ~1 cm above right ventricular outflow tract to expose the native pulmonary valve. Native pulmonary valve leaflets were excised and a stented valve scaffold, either 120 or 240 μm, was positioned orthotopically, attaching the distal portion of the stent to the pulmonary arterial wall upon closure with a running 4-0 polypropylene suture. Animals were then weaned from CPB and cannulae were removed following administration of protamine sulfate to return ACT to baseline.

Prior to chest closure, 2D epicardial echocardiography (echo) was performed to assess valve orientation and function. Trans-thoracic echo was repeated every 30 days. At defined study endpoints, 30- and 90-days, general anesthesia was induced and the heart was exposed by left thoracotomy. Valve function was finally assessed with epicardial echo prior to animal euthanasia.

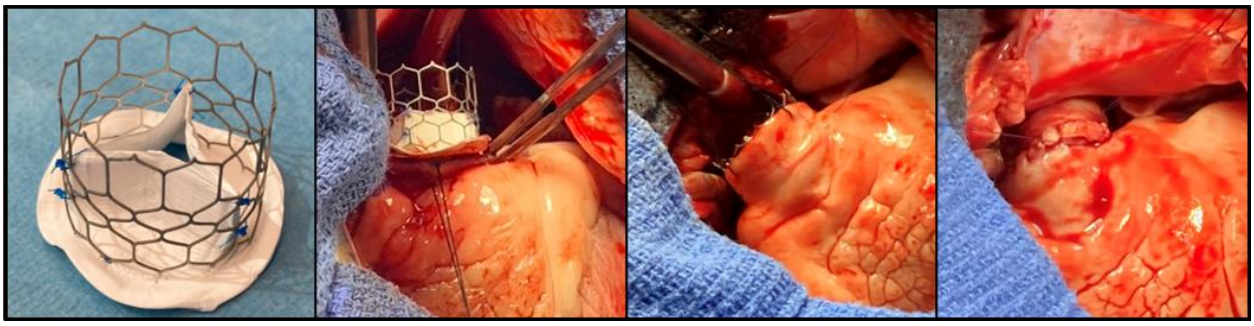

Appendix Figure 1. Pre-Implant and intraoperative photos of stented valve scaffold.

Appendix A.2.3 Explant Analysis

After animal euthanasia, the right ventricular outflow tract and pulmonary artery were removed and rinsed three times in heparinized saline (1 U/mL in 0.09% NaCl). Stented valve scaffolds were carefully removed from the stents, and were visually inspected for evidence of valve material failure or thrombosis. After removal, valve leaflets were separated along the radial direction into two halves and placed in 10% formalin solution for histological processing.

Sections 10 μm thick of explanted valve scaffold material, beginning at the midline of valve leaflets were then stained with hematoxylin & eosin to assess cell infiltration and neotissue formation, Picro-Sirrus Red and Masson Trichrome to assess collagen and ECM deposition and maturation, and Von Kossa to assess calcium deposition. Immunohistochemistry was performed with CD31 to assess endothelial cell presence and organization on the surface of valve scaffolds.

Appendix A.3 Results

Appendix A.3.1 Ovine Pulmonary Valve Replacement Model

Average thickness over the 15 locations of the valve leaflet surface for the 120 μm group was 0.133 ± 0.016 mm, and for the 240 μm group was 0.266 ± 0.019 mm.

At the 30-day timepoint, nine animals underwent pulmonary valve replacement (n=4 for 120 μm group). Of these, seven animals survived to study end, while two animals died early from complications not related to the valve scaffold. In the first two valve scaffolds implanted, the distal portion of the stent was not secured with a suture line. These two valve scaffolds were observed to have tilted during the course of the 30-day study upon explantation, necessitating a change to implantation protocol, and so were not included in final analysis. The final analysis of 30-day implants comprised n=3 valve scaffolds from the 240 μm group and n=2 valve scaffolds from the 120 μm group.

At the 90-day timepoint, four animals received pulmonary valve scaffolds (n=2/group), and all animals survived until study end. Upon explantation, one of the 240 μm valve scaffolds was observed to have tilted sometime between day 60 and day 90, and so this valve was not included in final analysis.

Epicardial echo at implantation showed varying degrees of failure in leaflet coaptation of all valves tested. This resulted in regurgitation ranging from trace (n=1 in 240 μm group), to mild (n=2/group), to moderate (n=1/group). At explant for the 30-day scaffolds, echo showed little change in leaflet motility and regurgitation except in one valve in the 120 μm group that showed greater leaflet motility and only trace regurgitation (from mild at implantation). Echo results from the 90-day scaffolds showed were more ambiguous. One valve in the 120 μm group showed

moderate regurgitation, an increase from mild regurgitation at implant, while the other valve in the 120 μm group showed mild regurgitation, down from moderate at implant. The 240 μm scaffold remained steady at mild regurgitation for the duration of the 90-day study.

Appendix A.3.2 Gross Morphological Assessment, 30-day Explants

After explanting the valve scaffolds at the 30-day timepoint, there was gross evidence of thrombosis in 2 of 3 valve scaffolds in the 240 μm group, which were located in all three of the commissural regions on the ventricular side, with varying dimensions (Appendix Figure 2, bottom row). The largest thrombus measured 0.65x0.5 cm. Qualitatively, the thrombi were a light pink, yellowish color. There was evidence of small tears in the polymer material in 1 of 2 valve scaffolds in the 120 μm group, located at the sites of suture puncture at the base of the leaflets (Appendix Figure 2, top row). Interestingly, the other valve scaffold in the 120 μm group showed no evidence of material failure, but had a substantial layer of tissue grown over the polymer valve. It was observed that under normal handling, the tissue layer delaminated easily from the polymer layer, indicating little or no tissue integration with the polymer material. Additionally, this was the only valve scaffold which experienced such tissue growth.

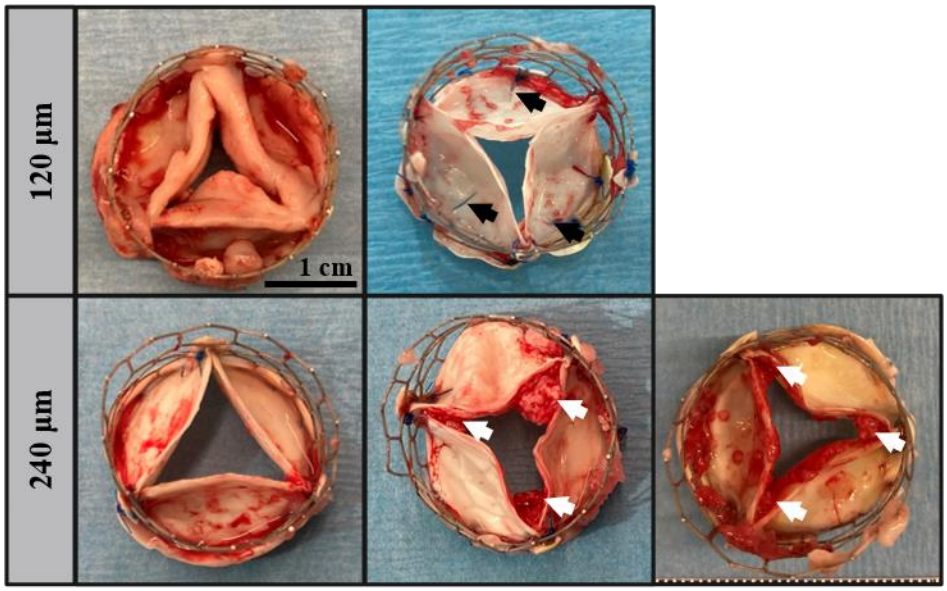

Appendix Figure 2. 30-day valve scaffold explants. (Top row) 120 µm explants showed either a large quantity of tissue overgrowth or small tears at the point of suture in the annular sewing ring. (Bottom row) 240 µm explants showed 2 out of 3 valves had significant thrombus formation at all three commissures. Black arrows indicate tears in polymer material. White arrows indicate thrombosis.

Appendix A.3.3 Gross Morphological Assessment, 90-day Explants

Gross morphological observation of 90-day explants showed no thrombosis on any of the valve scaffolds. There was a small tear in 1 of the 2 valve scaffolds in the 120 µm group, located at the junction between the leaflet and sewing ring adjacent to one of the commissures (Appendix Figure 3). Interestingly, despite the longer timepoint, the valve scaffolds had only minimal evidence of tissue growth on the surface of the polymer valve, localized to the base of the leaflets and the sewing ring.

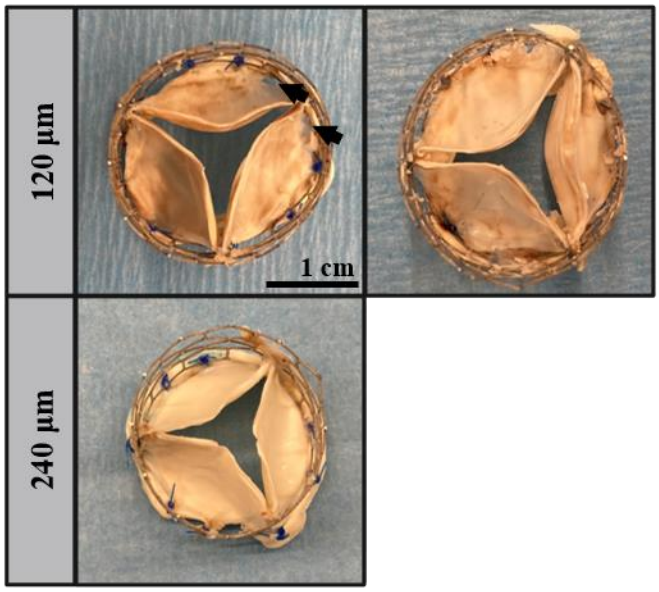

Appendix Figure 3. 90-day valve scaffold explants. (Top row) 120 µm explants showed 1 of 2 valves had small tears at the commissural juncture with the annular sewing ring. (Bottom row) 240 µm explant of 1 valve showed no issues under gross morphological assessment. Black arrows indicate tears in polymer material.

Appendix A.3.4 Histological Assessment, 30-day Explants

Histological assessment of 30-day explants showed largely no evidence of cell infiltration into the polymer scaffold or fibrous tissue growth within or encapsulating the polymer fiber network. There were two exceptions to this, the 120 µm valve scaffold that was observed to have a large mass of tissue growth, and one of the 240 µm valve scaffolds. Histological staining of the 120 µm valve scaffold (Appendix Figure 4) showed a large quantity of cells present immediately at the surface, and to a slightly lesser extent, interpenetrating within the polymer scaffold. Assessment of the quality of the tissue mass from Picro-sirrus Red and Masson Trichrome staining revealed that the mass was not characterized by mature fibrous tissue growth. Additionally, Von Kossa staining revealed the presence of several large calcific nodules with the polymer scaffold, spanning from the base to the free edge of the leaflet.

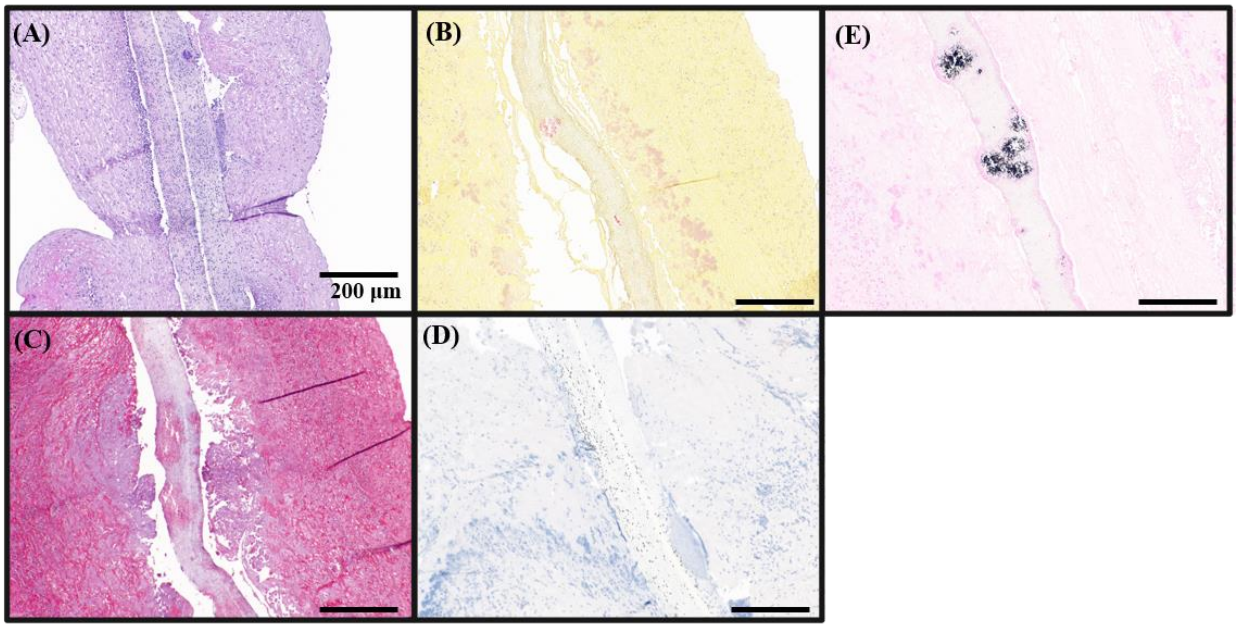

Appendix Figure 4. Histology of tissue overgrowth in 120 µm valve explant. 10x magnification images of the base region of valve leaflets. (A) H&E, (B) Picro-sirrus Red, (C) Masson Trichrome, (D) CD31, and (E) Von Kossa.

One of the three 240 µm valve scaffolds showed some degree of tissue growth encapsulating portions of the valve leaflet, primarily the base region (Appendix Figure 5). However, H&E staining showed that cellular infiltration was scarce. Picro-sirrus Red staining showed that, while most of the tissue encapsulation consisted of non-fibrous tissue or immature collagen, there was some maturation of a network of type I collagen. Endothelial cell presence was scarce, and was focalized at one portion of the base region of the valve scaffold only on the arterial side. Von Kossa showed no indication of calcific nodule formation.

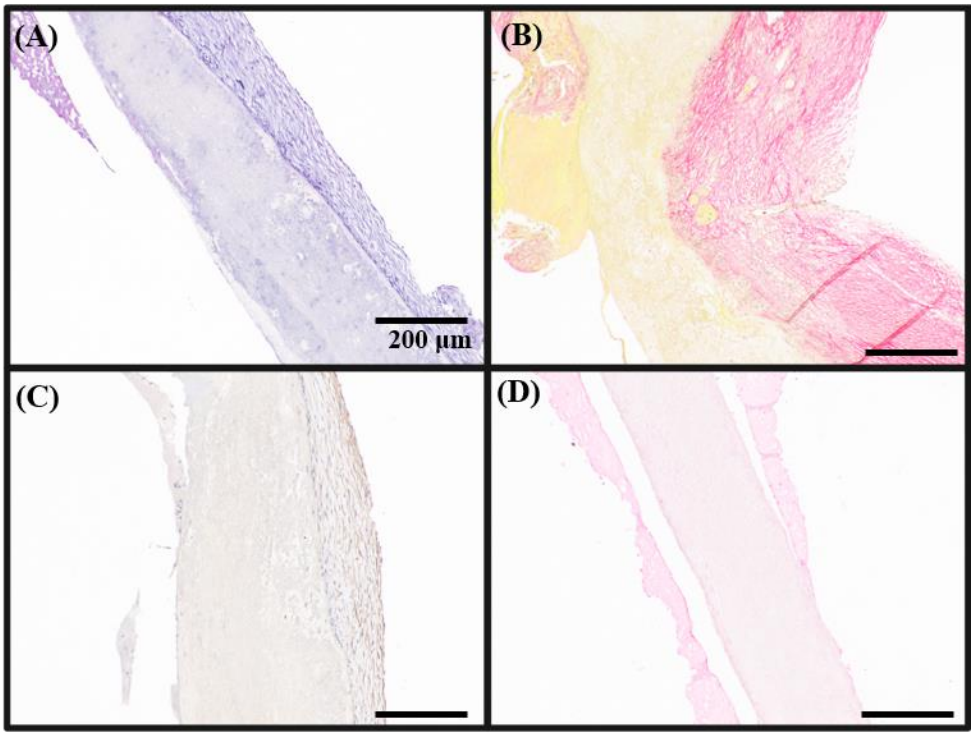

Appendix Figure 5. Histological assessment of 30-day 240 µm valve explant. 10x magnification images of the base region of valve leaflets. (A) H&E, (B) Picro-sirrus Red, (C) CD31, (D) Von Kossa.

Appendix A.3.5 Histological Assessment, 90-day Explants

There was a distinct difference in the presence of cells and tissue between 90-day explants in the 120 µm and 240 µm groups. At the base of valve scaffold leaflets, the 240 µm valve scaffolds were marked by encapsulation of tissue (Appendix Figure 6), whereas only scant evidence of cell adhesion and tissue formation was present in 120 µm valve scaffolds (Appendix Figure 7). Higher magnification views of the tissue growth at the base of 240 µm valve scaffolds revealed limited cellular infiltration into the fibrous network, with H&E stain demonstrating an absence of cell nuclei inside of the polymer network. More stark is the delineation between polymer and fibrous tissue stained with Picro-sirrus Red and Masson Trichrome. There was some, but limited, evidence

of fibrous tissue beginning to penetrate the polymer scaffold at the base region of 240 μm valves. Cell and tissue adhesion was only present at the base of valve leaflets. Extending toward the leaflet free edge, no cells or fibrous tissue was visible.

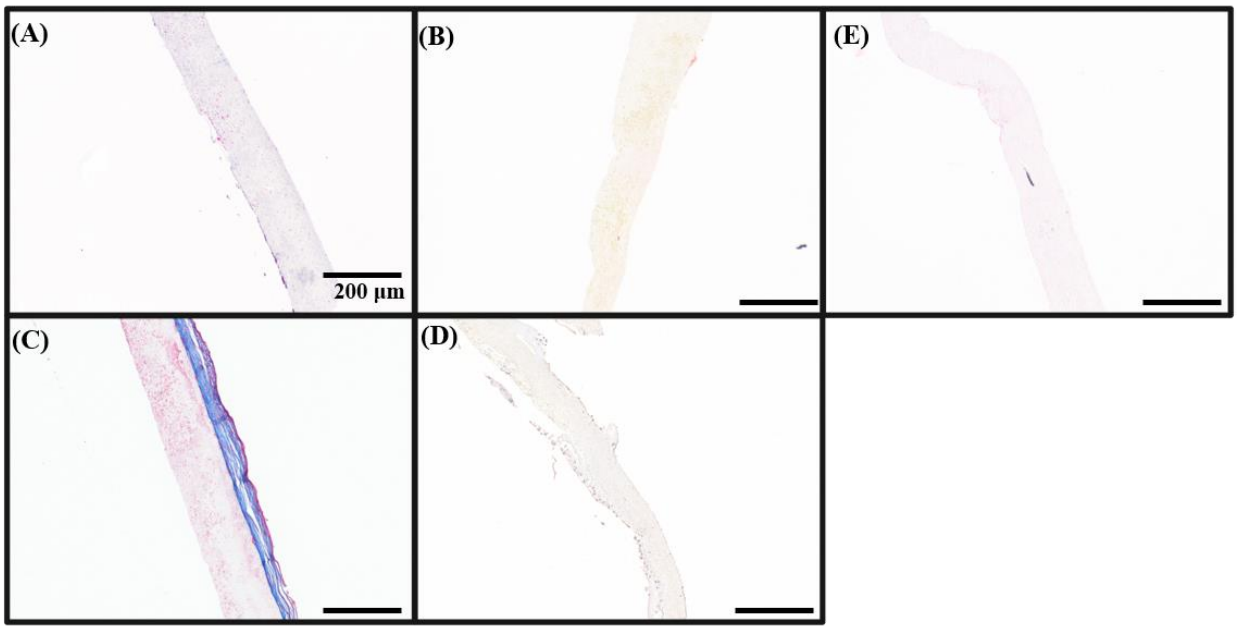

Appendix Figure 6. Histological assessment of 90-day 120 μm valve explants. 10x magnification images of the base region of valve leaflets. (A) H&E, (B) Picro-sirrus Red, (C) Masson Trichrome, (D) CD31, and (E) Von Kossa.

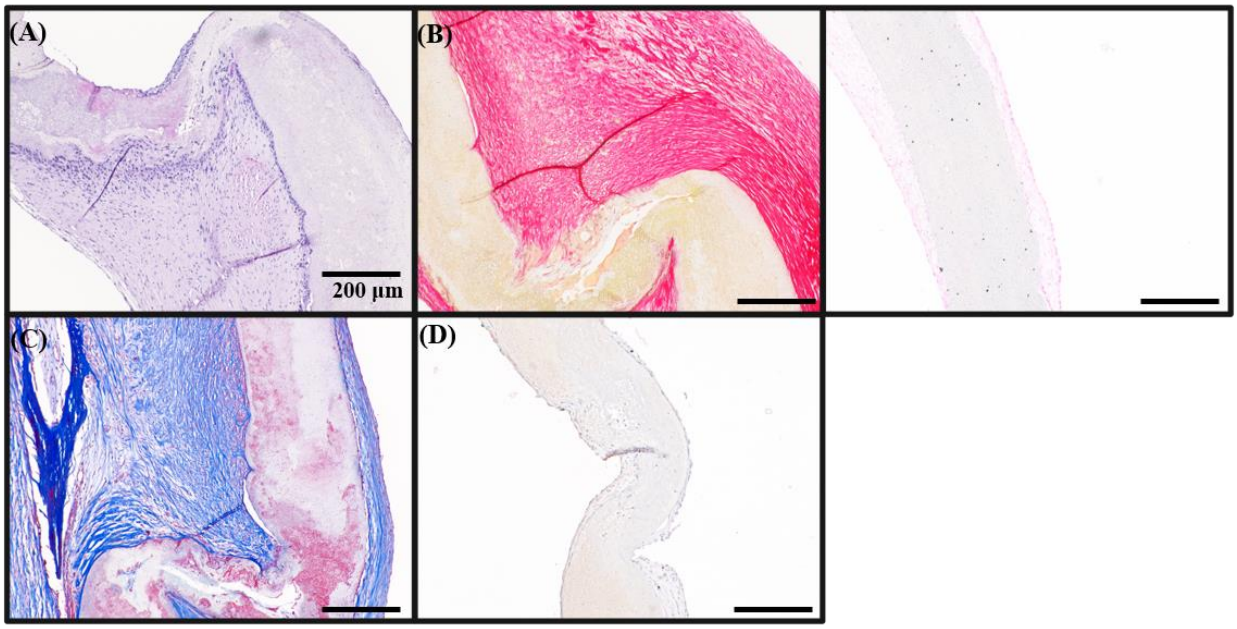

Appendix Figure 7. Histological assessment of 90-day 240 µm valve explants. 10x magnification images of the base region of valve leaflets. (A) H&E, (B) Picro-sirrus Red, (C) Masson Trichrome, (D) CD31, and (E) Von Kossa.

Appendix A.4 Discussion

The study performed here represents an early-phase, short-term analysis of PCUU-based degradable valve scaffolds. The study endpoints of 30- and 90-days are short relative to the timescales even of cell infiltration and neo-tissue formation, not to mention the timescales of complete polymer degradation. However, the shorter timepoints allow for an assessment of the more acute immune-mediated response, such as inflammation. For example, histological characterization of the 120 µm valve scaffold with substantial tissue growth lends to the conclusion that the valve scaffold was subject of a hyperactive immune response. The clustering of cells at the surface of the polymer scaffold appeared to be multi-nucleated foreign body giant cells which,

given the degree of cellular convergence to the polymer surface, indicated a strong inflammatory response. Additional evidence of a hyperactive immune response is the number and size of calcium deposits visible in Von Kossa staining. Pro-inflammatory macrophages release ROS that contribute to valve calcification [283]. Presence of calcification in this valve scaffold when it was not present in any other valve scaffold, either at 30- or 90-days, is indicative of abnormal biological response to the valve scaffold. The cause for this response is unclear. This level of cellular response and calcification at such an early timepoint has been seen before, in a study that also showed high variability in terms of tissue remodeling response to degradable valve scaffolds [118]. This outcome could be caused by the elevated immune responses in sheep relative to other large animal models [148], and a high variability in immune reaction on an individual level. However, to test this theory, a greater number of animal experiments would need to be conducted.

Results from the histology of the 90-day explants showed that tissue growth around the base of the valve leaflets was capable of forming mature fibrous tissue. The tissue growth did not extend outward toward the belly region or free edge of the leaflet but, at such a short study duration, tissue growth on the leaflet is not expected [131]. In comparable studies of degradable valves in an ovine model, tissue remodeling does not typically occur on the more dynamic portions of valve leaflets until after 6 months at least [132], [139]. What is interesting about the 90-day explants in this study was the lack of cell infiltration into the scaffold, even at the base region. One explanation for this could be the compactness of the electrospun fibrous network. For instance, in a previous study by our group analyzing microstructural characteristics of electrospun valve scaffolds fabricated under similar conditions, the average pore size was about 4 μm^2 [235], which is much smaller than the fibroblasts that would be desired to initiate tissue remodeling.

Valve function as measured from echo observations was less than optimal, exposing a flaw in valve scaffold design and stenting strategy. Upon implantation, most valves for both thickness groups had incomplete coaptation and mild to moderate central regurgitation. An additional troubling finding in this regard was the thrombosis in each of the commissural regions of 2 out of 3 240 μm valve scaffolds at the 30-day timepoint. The mandrel geometry was designed such that electrospun valves would be fabricated in a coapted state. Given the valve geometry, however, puncturing the valve leaflet material to secure the scaffold to the stent was unavoidable. To mitigate risk of valve tearing, pledgets made from PCUU were added to the commissure regions to reinforce suture attachment. In the course of reinforcement, the scaffold material was evidently placed under too much tension, causing a gap to form in the center of the valve scaffold, and limiting leaflet motility. Given the location and appearance of thrombi, it is likely that they were flow-induced by the lack of leaflet motion creating only a pinched orifice through which blood could flow.

Looking at the echo imaging in a relative sense, the results are surprisingly consistent. Over the course of 30 and 90 days, there was little to no change in the degree of regurgitation. This is in contrast to other groups that have shown rapid progression of leaflet contraction leading to moderate and severe regurgitation within 12 to 18 weeks [118], [131], [143]. Indeed, leaflet shortening, due to abnormal or extended immune response causing contractile cell phenotypes [107], leading to regurgitation has been the main failure mode of TEHVs in preclinical study. While it is possible that in chronic studies with longer durations these valve scaffolds will suffer the same fate, these initial findings are encouraging.

Initial, short-term *in vivo* study of valve replacements are an important step in valve design and development because of the unmatchable conditions of the animal model. The shortcomings

in valve design tested in this study revealed a need to compensate for stent mounting by modifying valve design to allow for full coaptation and leaflet motility while reinforcing suture points in the valve leaflet material. Additionally, given the range of biological response from animal to animal, a greater number of valve scaffolds should be implanted to adequately measure an average cellular response to the valve scaffolds used in this study. Post-processing of explants to yield more information regarding the specific immune response to these scaffolds may shed more light on applicability of this material as opposed to others that have been attempted. Moreover, data regarding immune response to valve scaffolds would be a useful addition to the literature mapping out inflammatory processes in TEHVs [156].

Bibliography

[1] M. E. Bowdish *et al.*, "The Society of Thoracic Surgeons Adult Cardiac Surgery Database: 2020 Update on Outcomes and Research," *Ann. Thorac. Surg.*, vol. 109, no. 6, pp. 1646–1655, Jun. 2020, doi: 10.1016/j.athoracsur.2020.03.003.

[2] P. Andell *et al.*, "Epidemiology of valvular heart disease in a Swedish nationwide hospital-based register study," *Heart*, vol. 103, no. 21, pp. 1696–1703, Nov. 2017, doi: 10.1136/heartjnl-2016-310894.

[3] D. Y. Tam, R. V. Rocha, H. C. Wijeysundera, P. C. Austin, D. Dvir, and S. E. Fremes, "Surgical valve selection in the era of transcatheter aortic valve replacement in the Society of Thoracic Surgeons Database," *J. Thorac. Cardiovasc. Surg.*, vol. 159, no. 2, pp. 416-427.e8, 2020, doi: 10.1016/j.jtcvs.2019.05.081.

[4] U.S. Food and Drug Administration, "Pre-Market Approval (PMA): EDWARDS SAPIEN TRANSCATHETER HEART VALVE AND ACCESSORIES," 2011. https://www.accessdata.fda.gov/scripts/cdrh/cfdocs/cfpma/pma.cfm?id=P100041.

[5] U.S. Food and Drug Administration, "Pre-Market Approval (PMA): MELODY TRANSCATHETER PULMONARY VALVE (TPV), ENSEMBLE TRANSCATHETER VALVE DELIVERY SYSTEM (DS)," 2015. https://www.accessdata.fda.gov/scripts/cdrh/cfdocs/cfpma/pma.cfm?id=P140017.

[6] J. D. Carroll *et al.*, "STS-ACC TVT Registry of Transcatheter Aortic Valve Replacement," *J. Am. Coll. Cardiol.*, vol. 76, no. 21, pp. 2492–2516, 2020, doi: 10.1016/j.jacc.2020.09.595.

[7] P. Pibarot and J. G. Dumesnil, "Prosthetic Heart Valves," *Circulation*, vol. 119, no. 7, pp. 1034–1048, Feb. 2009, doi: 10.1161/CIRCULATIONAHA.108.778886.

[8] Tillquist, Tillquist, and T. Maddox, "Cardiac crossroads: deciding between mechanical or bioprosthetic heart valve replacement," *Patient Prefer. Adherence*, vol. 5, p. 91, Feb. 2011, doi: 10.2147/PPA.S16420.

[9] S. J. Head, M. Çelik, and A. P. Kappetein, "Mechanical versus bioprosthetic aortic valve replacement," *Eur. Heart J.*, vol. 38, no. 28, pp. 2183–2191, Jul. 2017, doi: 10.1093/eurheartj/ehx141.

[10] A. B. Goldstone *et al.*, "Mechanical or Biologic Prostheses for Aortic-Valve and Mitral-Valve Replacement," *N. Engl. J. Med.*, vol. 377, no. 19, pp. 1847–1857, Nov. 2017, doi: 10.1056/NEJMoa1613792.

[11] C. M. Otto *et al.*, "2020 ACC/AHA Guideline for the Management of Patients With

Valvular Heart Disease," *J. Am. Coll. Cardiol.*, vol. 77, no. 4, pp. e25–e197, Feb. 2021, doi: 10.1016/j.jacc.2020.11.018.

[12] A. P. Yoganathan, Z. He, and S. Casey Jones, "Fluid Mechanics of Heart Valves," *Annu. Rev. Biomed. Eng.*, vol. 6, no. 1, pp. 331–362, Aug. 2004, doi: 10.1146/annurev.bioeng.6.040803.140111.

[13] F. Oveissi, S. Naficy, A. Lee, D. S. Winlaw, and F. Dehghani, "Materials and manufacturing perspectives in engineering heart valves: a review," *Mater. Today Bio*, vol. 5, no. December 2019, p. 100038, Jan. 2020, doi: 10.1016/j.mtbio.2019.100038.

[14] Q. Li, F. Hegner, and C. H. Bruecker, "Comparative study of wall-shear stress at the ascending aorta for different mechanical heart valve prostheses," *J. Biomech. Eng.*, vol. 142, no. 1, pp. 1–11, 2020, doi: 10.1115/1.4043357.

[15] D. Bluestein, E. Rambod, and M. Gharib, "Vortex Shedding as a Mechanism for Free Emboli Formation in Mechanical Heart Valves," *J. Biomech. Eng.*, vol. 122, no. 2, pp. 125–134, Apr. 2000, doi: 10.1115/1.429634.

[16] M. Hedayat, H. Asgharzadeh, and I. Borazjani, "Platelet activation of mechanical versus bioprosthetic heart valves during systole," *J. Biomech.*, vol. 56, pp. 111–116, May 2017, doi: 10.1016/j.jbiomech.2017.03.002.

[17] M. Hedayat and I. Borazjani, "Comparison of platelet activation through hinge vs bulk flow in bileaflet mechanical heart valves," *J. Biomech.*, vol. 83, pp. 280–290, Jan. 2019, doi: 10.1016/j.jbiomech.2018.12.003.

[18] M. Ahmed, N. Gupta, R. Jana, M. K. Das, and K. K. Kar, "Ramifications of Vorticity on Aggregation and Activation of Platelets in Bi-Leaflet Mechanical Heart Valve: Fluid–Structure-Interaction Study," *J. Biomech. Eng.*, vol. 144, no. 8, pp. 1–17, Aug. 2022, doi: 10.1115/1.4053665.

[19] W. R. E. Jamieson *et al.*, "PROSE: Prospective Randomized Trial of the On-X Mechanical Prosthesis and the St Jude Medical Mechanical Prosthesis Evaluation: Part 2: Study results—prostheses, positions, and economic development," *JTCVS Open*, vol. 12, no. C, pp. 51–70, 2022, doi: 10.1016/j.xjon.2022.07.011.

[20] B. Meuris, L. Van Hoof, W. Decré, M. Lamberigts, T. Langenaeken, and P. Verbrugghe, "In-vivo Evaluation of a Novel Surgical Heart Valve Prosthesis Designed to Be Durable, Anticoagulant-free and Silent," *Struct. Hear.*, vol. 5, p. 2, Jun. 2021, doi: 10.1080/24748706.2021.1898251.

[21] J. P. Binet, A. Carpentier, J. Langlois, C. Duran, and P. Colvez, "[Implantation of heterogenic valves in the treatment of aortic cardiopathies].," *C. R. Acad. Sci. Hebd. Seances Acad. Sci. D.*, vol. 261, no. 25, pp. 5733–4, Dec. 1965, [Online]. Available: http://www.ncbi.nlm.nih.gov/pubmed/4955645.

[22] T. Bourguignon *et al.*, "Very long-term outcomes of the carpentier-edwards perimount

valve in aortic position," *Ann. Thorac. Surg.*, vol. 99, no. 3, pp. 831–837, 2015, doi: 10.1016/j.athoracsur.2014.09.030.

[23] D. R. Johnston *et al.*, "Long-term durability of bioprosthetic aortic valves: Implications from 12,569 implants," *Ann. Thorac. Surg.*, vol. 99, no. 4, pp. 1239–1247, 2015, doi: 10.1016/j.athoracsur.2014.10.070.

[24] A. Carpentier, G. Lemaigre, L. Robert, S. Carpentier, C. Dubost, and F. Gerbode, "Biological factors affecting long-term results of valvular heterografts," *J. Thorac. Cardiovasc. Surg.*, vol. 58, no. 4, pp. 467–483, Oct. 1969, doi: 10.1016/S0022-5223(19)42561-0.

[25] F. J. Schoen, "Mechanisms of function and disease of natural and replacement heart valves," *Annu. Rev. Pathol. Mech. Dis.*, vol. 7, pp. 161–183, 2012, doi: 10.1146/annurev-pathol-011110-130257.

[26] D. F. Williams, D. Bezuidenhout, J. de Villiers, P. Human, and P. Zilla, "Long-Term Stability and Biocompatibility of Pericardial Bioprosthetic Heart Valves," *Front. Cardiovasc. Med.*, vol. 8, no. September, pp. 1–17, 2021, doi: 10.3389/fcvm.2021.728577.

[27] M. J. Thubrikar, J. D. Deck, J. Aouad, and S. P. Nolan, "Role of mechanical stress in calcification of aortic bioprosthetic valves," *J. Thorac. Cardiovasc. Surg.*, vol. 86, no. 1, pp. 115–125, Jul. 1983, doi: 10.1016/S0022-5223(19)39217-7.

[28] M. Deiwick *et al.*, "In vitro testing of bioprostheses: influence of mechanical stresses and lipids on calcification," *Ann. Thorac. Surg.*, vol. 66, no. 6, pp. S206–S211, Dec. 1998, doi: 10.1016/S0003-4975(98)01125-4.

[29] A. Whelan *et al.*, "Collagen fibre-mediated mechanical damage increases calcification of bovine pericardium for use in bioprosthetic heart valves," *Acta Biomater.*, vol. 128, pp. 384–392, 2021, doi: 10.1016/j.actbio.2021.04.046.

[30] N. Vyavahare *et al.*, "Prevention of Bioprosthetic Heart Valve Calcification by Ethanol Preincubation," *Circulation*, vol. 95, no. 2, pp. 479–488, Jan. 1997, doi: 10.1161/01.CIR.95.2.479.

[31] B. Meuris *et al.*, "A novel tissue treatment to reduce mineralization of bovine pericardial heart valves," *J. Thorac. Cardiovasc. Surg.*, vol. 156, no. 1, pp. 197–206, Jul. 2018, doi: 10.1016/j.jtcvs.2018.01.099.

[32] K. Z. Konakci *et al.*, "Alpha-Gal on bioprostheses: Xenograft immune response in cardiac surgery," *Eur. J. Clin. Invest.*, vol. 35, no. 1, pp. 17–23, 2005, doi: 10.1111/j.1365-2362.2005.01441.x.

[33] N. Lila, C. G. A. McGregor, S. Carpentier, J. Rancic, G. W. Byrne, and A. Carpentier, "Gal knockout pig pericardium: New source of material for heart valve bioprostheses," *J. Hear. Lung Transplant.*, vol. 29, no. 5, pp. 538–543, 2010, doi: 10.1016/j.healun.2009.10.007.

[34] F. Naso *et al.*, “Alpha-Gal Inactivated Heart Valve Bioprostheses Exhibit an Anti-Calcification Propensity Similar to Knockout Tissues,” *Tissue Eng. - Part A*, vol. 23, no. 19–20, pp. 1181–1195, 2017, doi: 10.1089/ten.tea.2016.0474.

[35] F. Naso *et al.*, “Correlations between the alpha-Gal antigen, antibody response and calcification of cardiac valve bioprostheses: experimental evidence obtained using an alpha-Gal knockout mouse animal model,” *Front. Immunol.*, vol. 14, no. June, pp. 1–10, 2023, doi: 10.3389/fimmu.2023.1210098.

[36] P. Human, D. Bezuidenhout, E. Aikawa, and P. Zilla, “Residual Bioprosthetic Valve Immunogenicity: Forgotten, Not Lost,” *Front. Cardiovasc. Med.*, vol. 8, no. January, pp. 1–11, 2022, doi: 10.3389/fcvm.2021.760635.

[37] Y. Zhou, T. Xiong, P. Bai, C. Chu, and N. Dong, “Clinical outcomes of transcatheter versus surgical pulmonary valve replacement: A meta-analysis,” *J. Thorac. Dis.*, vol. 11, no. 12, pp. 5343–5351, 2019, doi: 10.21037/jtd.2019.11.64.

[38] A. Alperi *et al.*, “Transcatheter tricuspid valve interventions: Current status and future perspectives,” *Front. Cardiovasc. Med.*, vol. 9, no. 1, pp. 1–9, Sep. 2022, doi: 10.3389/fcvm.2022.994502.

[39] M. Hensey *et al.*, “Transcatheter Mitral Valve Replacement: An Update on Current Techniques, Technologies, and Future Directions,” *JACC Cardiovasc. Interv.*, vol. 14, no. 5, pp. 489–500, 2021, doi: 10.1016/j.jcin.2020.12.038.

[40] C. R. Smith *et al.*, “Transcatheter versus Surgical Aortic-Valve Replacement in High-Risk Patients,” *N. Engl. J. Med.*, vol. 364, no. 23, pp. 2187–2198, Jun. 2011, doi: 10.1056/NEJMoa1103510.

[41] A. Alperi, S. Garcia, and J. Rodés-Cabau, “Transcatheter valve-in-valve implantation in degenerated surgical aortic and mitral bioprosthesis: Current state and future perspectives,” *Prog. Cardiovasc. Dis.*, vol. 72, pp. 54–65, 2022, doi: 10.1016/j.pcad.2021.10.001.

[42] A. J. Coury, “Chemical and Biochemical Degradation of Polymers Intended to Be Biostable,” in *Biomaterials Science*, Fourth Edi., W. R. Wagner, G. Zhang, S. E. Sakiyama-Elbert, and M. J. Yaszemski, Eds. Elsevier, 2020, pp. 919–940.

[43] N. S. Braunwald and A. G. Morrow, “A LATE EVALUATION OF FLEXIBLE TEFLON PROSTHESES UTILIZED FOR TOTAL AORTIC VALVE REPLACEMENT,” *J. Thorac. Cardiovasc. Surg.*, vol. 49, no. 3, pp. 485–496, Mar. 1965, doi: 10.1016/S0022-5223(19)33284-2.

[44] N. S. Braunwald, T. Cooper, and A. G. Morrow, “COMPLETE REPLACEMENT OF THE MITRAL VALVE,” *J. Thorac. Cardiovasc. Surg.*, vol. 40, no. 1, pp. 1–11, Jul. 1960, doi: 10.1016/S0022-5223(19)32638-8.

[45] C. B. Wisman, W. S. Pierce, J. H. Donachy, W. E. Pae, J. L. Myers, and G. A. Prophet, “A Polyurethane Trileaflet Cardiac Valve Prosthesis - In Vitro and In Vivo Studies,” *Trans.*

Am. Soc. Artif. Intern. Organs, vol. 28, no. 1, pp. 164–168, 1982, [Online]. Available: https://journals.lww.com/asaiojournal/Citation/1982/28000/A_Polyurethane_Trileaflet_Cardiac_Valve.33.aspx.

[46] S. L. Hilbert, V. J. Ferrans, Y. Tornita, E. E. Eidbo, and M. Jones, "Evaluation of explanted polyurethane trileaflet cardiac valve prostheses," *J. Thorac. Cardiovasc. Surg.*, vol. 94, no. 3, pp. 419–429, Sep. 1987, doi: 10.1016/S0022-5223(19)36257-9.

[47] G. M. Bernacca, T. G. Mackay, R. Wilkinson, and D. J. Wheatley, "Polyurethane heart valves: Fatigue failure, calcification, and polyurethane structure," *J. Biomed. Mater. Res.*, vol. 34, no. 3, pp. 371–379, 1997, doi: 10.1002/(SICI)1097-4636(19970305)34:3<371::AID-JBM12>3.0.CO;2-J.

[48] E. M. Christenson, J. M. Anderson, and A. Hiltner, "Oxidative mechanisms of poly(carbonate urethane) and poly(ether urethane) biodegradation: In vivo and in vitro correlations," *J. Biomed. Mater. Res. - Part A*, vol. 70, no. 2, pp. 245–255, 2004, doi: 10.1002/jbm.a.30067.

[49] L. S. Dandeniyage *et al.*, "In vitro oxidative stability of high strength siloxane poly(urethane-urea) elastomers based on linked-macrodiol," *J. Biomed. Mater. Res. - Part B Appl. Biomater.*, vol. 107, no. 8, pp. 2557–2565, 2019, doi: 10.1002/jbm.b.34346.

[50] H. Ghanbari, A. G. Kidane, G. Burriesci, B. Ramesh, A. Darbyshire, and A. M. Seifalian, "The anti-calcification potential of a silsesquioxane nanocomposite polymer under in vitro conditions: Potential material for synthetic leaflet heart valve☆," *Acta Biomater.*, vol. 6, no. 11, pp. 4249–4260, Nov. 2010, doi: 10.1016/j.actbio.2010.06.015.

[51] M. Heitkemper, H. Hatoum, and L. P. Dasi, "In vitro hemodynamic assessment of a novel polymeric transcatheter aortic valve," *J. Mech. Behav. Biomed. Mater.*, vol. 98, pp. 163–171, Oct. 2019, doi: 10.1016/j.jmbbm.2019.06.016.

[52] O. M. Rotman, B. Kovarovic, M. Bianchi, M. J. Slepian, and D. Bluestein, "In Vitro Durability and Stability Testing of a Novel Polymeric Transcatheter Aortic Valve," *ASAIO J.*, vol. 66, no. 2, pp. 190–198, 2020, doi: 10.1097/MAT.0000000000000980.

[53] B. Kovarovic, R. Helbock, K. Baylous, O. M. Rotman, M. J. Slepian, and D. Bluestein, "Visions of TAVR Future: Development and Optimization of a Second Generation Novel Polymeric TAVR," *J. Biomech. Eng.*, vol. 144, no. 6, Jun. 2022, doi: 10.1115/1.4054149.

[54] J. R. Stasiak *et al.*, "Design, development, testing at ISO standards and: In vivo feasibility study of a novel polymeric heart valve prosthesis," *Biomater. Sci.*, vol. 8, no. 16, pp. 4467–4480, 2020, doi: 10.1039/d0bm00412j.

[55] C. Jenney *et al.*, "Assessment of a Siloxane Poly(urethane-urea) Elastomer Designed for Implantable Heart Valve Leaflets," *Adv. NanoBiomed Res.*, vol. 1, no. 2, p. 2000032, 2021, doi: 10.1002/anbr.202000032.

[56] M. Kachel *et al.*, "Temporal, biomechanical evaluation of a novel, transcatheter polymeric

aortic valve in ovine aortic banding model," *Front. Cardiovasc. Med.*, vol. 9, no. December, pp. 1–10, 2022, doi: 10.3389/fcvm.2022.977006.

[57] S. H. Daebritz *et al.*, "Introduction of a flexible polymeric heart valve prosthesis with special design for aortic position," *Eur. J. Cardio-thoracic Surg.*, vol. 25, no. 6, pp. 946–952, 2004, doi: 10.1016/j.ejcts.2004.02.040.

[58] D. J. Kereiakes *et al.*, "Preliminary Evaluation of a Novel Polymeric Valve Following Surgical Implantation for Symptomatic Aortic Valve Disease," *JACC Cardiovasc. Interv.*, vol. 14, no. 24, pp. 2754–2756, 2021, doi: 10.1016/j.jcin.2021.08.071.

[59] J. P. Santerre, K. Woodhouse, G. Laroche, and R. S. Labow, "Understanding the biodegradation of polyurethanes: From classical implants to tissue engineering materials," *Biomaterials*, vol. 26, no. 35, pp. 7457–7470, 2005, doi: 10.1016/j.biomaterials.2005.05.079.

[60] T. Shinoka *et al.*, "Tissue Engineering Heart Valves: Valve Leaflet Replacement Study in a Lamb Model," *Ann. Thorac. Surg.*, vol. 60, no. 6, pp. S513–S516, Dec. 1995, doi: 10.1016/S0003-4975(21)01185-1.

[61] P. Simon *et al.*, "Early failure of the tissue engineered porcine heart valve SYNERGRAFT™ in pediatric patients," *Eur. J. Cardio-thoracic Surg.*, vol. 23, no. 6, pp. 1002–1006, 2003, doi: 10.1016/S1010-7940(03)00094-0.

[62] S. Cebotari *et al.*, "Clinical application of tissue engineered human heart valves using autologous progenitor cells," *Circulation*, vol. 114, no. SUPPL. 1, pp. 132–137, 2006, doi: 10.1161/CIRCULATIONAHA.105.001065.

[63] P. M. Dohmen *et al.*, "Mid-Term Clinical Results Using a Tissue-Engineered Pulmonary Valve to Reconstruct the Right Ventricular Outflow Tract During the Ross Procedure," *Ann. Thorac. Surg.*, vol. 84, no. 3, pp. 729–736, 2007, doi: 10.1016/j.athoracsur.2007.04.072.

[64] T. C. Flanagan *et al.*, "In vivo remodeling and structural characterization of fibrin-based tissue-engineered heart valves in the adult sheep model," *Tissue Eng. - Part A*, vol. 15, no. 10, pp. 2965–2976, 2009, doi: 10.1089/ten.tea.2009.0018.

[65] J. M. Reimer, Z. H. Syedain, B. H. T. Haynie, and R. T. Tranquillo, "Pediatric tubular pulmonary heart valve from decellularized engineered tissue tubes," *Biomaterials*, vol. 62, pp. 88–94, 2015, doi: 10.1016/j.biomaterials.2015.05.009.

[66] J. Dubé *et al.*, "Progress in developing a living human tissue-engineered tri-leaflet heart valve assembled from tissue produced by the self-assembly approach," *Acta Biomater.*, vol. 10, no. 8, pp. 3563–3570, 2014, doi: 10.1016/j.actbio.2014.04.033.

[67] A. D'Amore *et al.*, "Heart valve scaffold fabrication: Bioinspired control of macro-scale morphology, mechanics and micro-structure," *Biomaterials*, vol. 150, pp. 25–37, 2018, doi: 10.1016/j.biomaterials.2017.10.011.

[68] J. Kluin *et al.*, “In situ heart valve tissue engineering using a bioresorbable elastomeric implant – From material design to 12 months follow-up in sheep,” *Biomaterials*, vol. 125, pp. 101–117, 2017, doi: 10.1016/j.biomaterials.2017.02.007.

[69] M. Uiterwijk *et al.*, “In Situ Remodeling Overrules Bioinspired Scaffold Architecture of Supramolecular Elastomeric Tissue-Engineered Heart Valves,” *JACC Basic to Transl. Sci.*, vol. 5, no. 12, pp. 1187–1206, 2020, doi: 10.1016/j.jacbts.2020.09.011.

[70] A. K. Capulli *et al.*, “JetValve: Rapid manufacturing of biohybrid scaffolds for biomimetic heart valve replacement,” *Biomaterials*, vol. 133, pp. 229–241, 2017, doi: 10.1016/j.biomaterials.2017.04.033.

[71] N. T. Saidy *et al.*, “Biologically Inspired Scaffolds for Heart Valve Tissue Engineering via Melt Electrowriting,” *Small*, vol. 15, no. 24, 2019, doi: 10.1002/smll.201900873.

[72] D. S. Puperi *et al.*, “Electrospun Polyurethane and Hydrogel Composite Scaffolds as Biomechanical Mimics for Aortic Valve Tissue Engineering,” *ACS Biomater. Sci. Eng.*, vol. 2, no. 9, pp. 1546–1558, 2016, doi: 10.1021/acsbiomaterials.6b00309.

[73] Y. Luo *et al.*, “3D Scaffolds,” *Princ. Tissue Eng. Fourth Ed.*, vol. 7, no. 2013, pp. 475–494, 2013, doi: 10.1016/B978-0-12-398358-9.00024-0.

[74] D. H. Reneker and A. L. Yarin, “Electrospinning jets and polymer nanofibers,” *Polymer (Guildf).*, vol. 49, no. 10, pp. 2387–2425, 2008, doi: 10.1016/j.polymer.2008.02.002.

[75] S. H. Yousefi, D. G. Venkateshan, C. Tang, H. V. Tafreshi, and B. Pourdeyhimi, “Effects of electrospinning conditions on microstructural properties of polystyrene fibrous materials,” *J. Appl. Phys.*, vol. 124, no. 23, 2018, doi: 10.1063/1.5049128.

[76] S. Ramakrishna, K. Fujihara, W.-E. Teo, T.-C. Lim, and Z. Ma, “Electrospinning Process,” in *An Introduction to Electrospinning and Nanofibers*, 1st ed., S. Ramakrishna, K. Fujihara, W.-O. Teo, T.-C. Lim, and Z. Ma, Eds. Singapore: WORLD SCIENTIFIC, 2005, pp. 90–154.

[77] J. Xue, T. Wu, Y. Dai, and Y. Xia, “Electrospinning and electrospun nanofibers: Methods, materials, and applications,” *Chem. Rev.*, vol. 119, no. 8, pp. 5298–5415, 2019, doi: 10.1021/acs.chemrev.8b00593.

[78] M. R. Badrossamay, H. A. McIlwee, J. A. Goss, and K. K. Parker, “Nanofiber assembly by rotary jet-spinning,” *Nano Lett.*, vol. 10, no. 6, pp. 2257–2261, 2010, doi: 10.1021/nl101355x.

[79] S. E. Motta *et al.*, “On-demand heart valve manufacturing using focused rotary jet spinning,” *Matter*, vol. 6, no. 6, pp. 1860–1879, 2023, doi: 10.1016/j.matt.2023.05.025.

[80] N. T. Saidy *et al.*, “Spatially Heterogeneous Tubular Scaffolds for In Situ Heart Valve Tissue Engineering Using Melt Electrowriting,” *Adv. Funct. Mater.*, vol. 32, no. 21, 2022, doi: 10.1002/adfm.202110716.

[81] S. Arjunon, S. Rathan, H. Jo, and A. P. Yoganathan, "Aortic valve: Mechanical environment and mechanobiology," *Ann. Biomed. Eng.*, vol. 41, no. 7, pp. 1331–1346, 2013, doi: 10.1007/s10439-013-0785-7.

[82] L. Sun, S. Chandra, and P. Sucosky, "Ex Vivo Evidence for the Contribution of Hemodynamic Shear Stress Abnormalities to the Early Pathogenesis of Calcific Bicuspid Aortic Valve Disease," *PLoS One*, vol. 7, no. 10, 2012, doi: 10.1371/journal.pone.0048843.

[83] M. K. Rausch, W. Bothe, J. P. E. Kvitting, S. Göktepe, D. Craig Miller, and E. Kuhl, "In vivo dynamic strains of the ovine anterior mitral valve leaflet," *J. Biomech.*, vol. 44, no. 6, pp. 1149–1157, 2011, doi: 10.1016/j.jbiomech.2011.01.020.

[84] W. Sun, A. Abad, and M. S. Sacks, "Simulated bioprosthetic heart valve deformation under quasi-static loading," *J. Biomech. Eng.*, vol. 127, no. 6, pp. 905–914, 2005, doi: 10.1115/1.2049337.

[85] Z. He, J. Ritchie, J. S. Grashow, M. S. Sacks, and A. P. Yoganathan, "In vitro dynamic strain behavior of the mitral valve posterior leaflet," *J. Biomech. Eng.*, vol. 127, no. 3, pp. 504–511, 2005, doi: 10.1115/1.1894385.

[86] C. H. Yap, H. S. Kim, K. Balachandran, M. Weiler, R. Haj-Ali, and A. P. Yoganathan, "Dynamic deformation characteristics of porcine aortic valve leaflet under normal and hypertensive conditions," *Am. J. Physiol. - Hear. Circ. Physiol.*, vol. 298, no. 2, pp. 395–405, 2010, doi: 10.1152/ajpheart.00040.2009.

[87] M. Weiler, C. Hwai Yap, K. Balachandran, M. Padala, and A. P. Yoganathan, "Regional analysis of dynamic deformation characteristics of native aortic valve leaflets," *J. Biomech.*, vol. 44, no. 8, pp. 1459–1465, 2011, doi: 10.1016/j.jbiomech.2011.03.017.

[88] W. Zhang, G. Rossini, D. Kamensky, T. Bui-Thanh, and M. S. Sacks, "Isogeometric finite element-based simulation of the aortic heart valve: Integration of neural network structural material model and structural tensor fiber architecture representations," *Int. j. numer. method. biomed. eng.*, vol. 37, no. 4, pp. 1–28, 2021, doi: 10.1002/cnm.3438.

[89] W. Zhang, S. Motiwale, M. C. Hsu, and M. S. Sacks, "Simulating the time evolving geometry, mechanical properties, and fibrous structure of bioprosthetic heart valve leaflets under cyclic loading," *J. Mech. Behav. Biomed. Mater.*, vol. 123, no. December 2020, p. 104745, 2021, doi: 10.1016/j.jmbbm.2021.104745.

[90] T. A. Pawade, D. E. Newby, and M. R. Dweck, "Calcification in Aortic Stenosis," *J. Am. Coll. Cardiol.*, vol. 66, no. 5, pp. 561–577, Aug. 2015, doi: 10.1016/j.jacc.2015.05.066.

[91] M. Thubrikar, *The Aortic Valve*, First. New York, NY: Informa Healthcare, 2011.

[92] R. Haj-Ali, G. Marom, S. Ben Zekry, M. Rosenfeld, and E. Raanani, "A general three-dimensional parametric geometry of the native aortic valve and root for biomechanical modeling," *J. Biomech.*, vol. 45, no. 14, pp. 2392–2397, 2012, doi: 10.1016/j.jbiomech.2012.07.017.

[93] G. Marom, R. Halevi, R. Haj-Ali, M. Rosenfeld, H. J. Schäfers, and E. Raanani, "Numerical model of the aortic root and valve: Optimization of graft size and sinotubular junction to annulus ratio," *J. Thorac. Cardiovasc. Surg.*, vol. 146, no. 5, pp. 1227–1231, 2013, doi: 10.1016/j.jtcvs.2013.01.030.

[94] S. Morganti *et al.*, "Aortic root 3D parametric morphological model from 2D-echo images," *Comput. Biol. Med.*, vol. 43, no. 12, pp. 2196–2204, 2013, doi: 10.1016/j.compbiomed.2013.09.015.

[95] M. Abbasi and A. N. Azadani, "A geometry optimization framework for transcatheter heart valve leaflet design," *J. Mech. Behav. Biomed. Mater.*, vol. 102, no. October 2019, p. 103491, 2020, doi: 10.1016/j.jmbbm.2019.103491.

[96] H. T. Bui, A. Ishrat, S. P. James, and L. P. Dasi, "Design consideration of a novel polymeric transcatheter heart valve through computational modeling," *J. Mech. Behav. Biomed. Mater.*, vol. 135, no. June, p. 105434, 2022, doi: 10.1016/j.jmbbm.2022.105434.

[97] S. Loerakker, G. Argento, C. W. J. Oomens, and F. P. T. Baaijens, "Effects of valve geometry and tissue anisotropy on the radial stretch and coaptation area of tissue-engineered heart valves," *J. Biomech.*, vol. 46, no. 11, pp. 1792–1800, Jul. 2013, doi: 10.1016/j.jbiomech.2013.05.015.

[98] S. E. Motta *et al.*, "Geometry influences inflammatory host cell response and remodeling in tissue-engineered heart valves in-vivo," *Sci. Rep.*, vol. 10, no. 1, pp. 1–14, 2020, doi: 10.1038/s41598-020-76322-9.

[99] H. L. Leo, L. P. Dasi, J. Carberry, H. A. Simon, and A. P. Yoganathan, "Fluid dynamic assessment of three polymeric heart valves using particle image velocimetry," *Ann. Biomed. Eng.*, vol. 34, no. 6, pp. 936–952, 2006, doi: 10.1007/s10439-006-9117-5.

[100] L. Ge, L. P. Dasi, F. Sotiropoulos, and A. P. Yoganathan, "Characterization of hemodynamic forces induced by mechanical heart valves: Reynolds vs. viscous stresses," *Ann. Biomed. Eng.*, vol. 36, no. 2, pp. 276–297, 2008, doi: 10.1007/s10439-007-9411-x.

[101] H. Hatoum, F. Heim, and L. P. Dasi, "Stented valve dynamic behavior induced by polyester fiber leaflet material in transcatheter aortic valve devices," *J. Mech. Behav. Biomed. Mater.*, vol. 86, no. June, pp. 232–239, 2018, doi: 10.1016/j.jmbbm.2018.06.038.

[102] H. Hatoum, A. Yousefi, S. Lilly, P. Maureira, J. Crestanello, and L. P. Dasi, "An in vitro evaluation of turbulence after transcatheter aortic valve implantation," *J. Thorac. Cardiovasc. Surg.*, vol. 156, no. 5, pp. 1837–1848, 2018, doi: 10.1016/j.jtcvs.2018.05.042.

[103] H. Hatoum, S. Lilly, P. Maureira, J. Crestanello, and L. P. Dasi, "The hemodynamics of transcatheter aortic valves in transcatheter aortic valves," *J. Thorac. Cardiovasc. Surg.*, vol. 161, no. 2, pp. 565-576.e2, 2021, doi: 10.1016/j.jtcvs.2019.09.174.

[104] C. Del Gaudio, P. L. Gasbarroni, and G. P. Romano, "Experimental investigations on the fluid-mechanics of an electrospun heart valve by means of particle image velocimetry," *J.*

Mech. Behav. Biomed. Mater., vol. 64, pp. 229–239, 2016, doi: 10.1016/j.jmbbm.2016.07.030.

[105] B. Mirani, S. P. Nejad, and C. A. Simmons, "Recent Progress Toward Clinical Translation of Tissue-Engineered Heart Valves," *Can. J. Cardiol.*, vol. 37, no. 7, pp. 1064–1077, 2021, doi: 10.1016/j.cjca.2021.03.022.

[106] E. S. Fioretta, P. E. Dijkman, M. Y. Emmert, and S. P. Hoerstrup, "The future of heart valve replacement: recent developments and translational challenges for heart valve tissue engineering," *J. Tissue Eng. Regen. Med.*, vol. 12, no. 1, pp. e323–e335, Jan. 2018, doi: 10.1002/term.2326.

[107] E. S. Fioretta *et al.*, "Next-generation tissue-engineered heart valves with repair, remodelling and regeneration capacity," *Nat. Rev. Cardiol.*, vol. 18, no. 2, pp. 92–116, 2021, doi: 10.1038/s41569-020-0422-8.

[108] B. Weber *et al.*, "Prenatally engineered autologous amniotic fluid stem cell-based heart valves in the fetal circulation," *Biomaterials*, vol. 33, no. 16, pp. 4031–4043, Jun. 2012, doi: 10.1016/j.biomaterials.2011.11.087.

[109] C. K. Breuer *et al.*, "Tissue engineering lamb heart valve leaflets," *Biotechnol. Bioeng.*, vol. 50, no. 5, pp. 562–567, Jun. 1996, doi: 10.1002/(SICI)1097-0290(19960605)50:5<562::AID-BIT11>3.0.CO;2-L.

[110] R. Sodian *et al.*, "Early In Vivo Experience With Tissue-Engineered Trileaflet Heart Valves," *Circulation*, vol. 102, no. suppl_3, pp. 22–29, Nov. 2000, doi: 10.1161/circ.102.suppl_3.III-22.

[111] S. P. Hoerstrup *et al.*, "Functional Living Trileaflet Heart Valves Grown In Vitro," *Circulation*, vol. 102, no. suppl_3, Nov. 2000, doi: 10.1161/circ.102.suppl_3.III-44.

[112] U. A. Stock *et al.*, "Tissue-engineered valved conduits in the pulmonary circulation," *J. Thorac. Cardiovasc. Surg.*, vol. 119, no. 4, pp. 732–740, Apr. 2000, doi: 10.1016/S0022-5223(00)70008-0.

[113] S. P. Hoerstrup *et al.*, "Tissue Engineering of Functional Trileaflet Heart Valves From Human Marrow Stromal Cells," *Circulation*, vol. 106, no. 12_suppl_1, pp. 143–150, Sep. 2002, doi: 10.1161/01.cir.0000032872.55215.05.

[114] D. Gottlieb *et al.*, "In vivo monitoring of function of autologous engineered pulmonary valve," *J. Thorac. Cardiovasc. Surg.*, vol. 139, no. 3, pp. 723–731, Mar. 2010, doi: 10.1016/j.jtcvs.2009.11.006.

[115] D. Schmidt *et al.*, "Minimally-Invasive Implantation of Living Tissue Engineered Heart Valves," *J. Am. Coll. Cardiol.*, vol. 56, no. 6, pp. 510–520, Aug. 2010, doi: 10.1016/j.jacc.2010.04.024.

[116] C. E. Eckert *et al.*, "Three-Dimensional Quantitative Micromorphology of Pre- and Post-

Implanted Engineered Heart Valve Tissues," *Ann. Biomed. Eng.*, vol. 39, no. 1, pp. 205–222, Jan. 2011, doi: 10.1007/s10439-010-0162-8.

[117] M. Y. Emmert *et al.*, "Stem Cell–Based Transcatheter Aortic Valve Implantation," *JACC Cardiovasc. Interv.*, vol. 5, no. 8, pp. 874–883, Aug. 2012, doi: 10.1016/j.jcin.2012.04.010.

[118] E. S. Fioretta *et al.*, "Differential Leaflet Remodeling of Bone Marrow Cell Pre-Seeded Versus Nonseeded Bioresorbable Transcatheter Pulmonary Valve Replacements," *JACC Basic to Transl. Sci.*, vol. 5, no. 1, pp. 15–31, Jan. 2020, doi: 10.1016/j.jacbts.2019.09.008.

[119] D. K. Hildebrand, Z. J. Wu, J. E. Mayer, Jr., and M. S. Sacks, "Design and Hydrodynamic Evaluation of a Novel Pulsatile Bioreactor for Biologically Active Heart Valves," *Ann. Biomed. Eng.*, vol. 32, no. 8, pp. 1039–1049, Aug. 2004, doi: 10.1114/B:ABME.0000036640.11387.4b.

[120] A. Mol, N. J. B. Driessen, M. C. M. Rutten, S. P. Hoerstrup, C. V. C. Bouten, and F. P. T. Baaijens, "Tissue Engineering of Human Heart Valve Leaflets: A Novel Bioreactor for a Strain-Based Conditioning Approach," *Ann. Biomed. Eng.*, vol. 33, no. 12, pp. 1778–1788, Dec. 2005, doi: 10.1007/s10439-005-8025-4.

[121] Z. H. Syedain and R. T. Tranquillo, "Controlled cyclic stretch bioreactor for tissue-engineered heart valves," *Biomaterials*, vol. 30, no. 25, pp. 4078–4084, Sep. 2009, doi: 10.1016/j.biomaterials.2009.04.027.

[122] G. L. Converse *et al.*, "Design and efficacy of a single-use bioreactor for heart valve tissue engineering," *J. Biomed. Mater. Res. Part B Appl. Biomater.*, vol. 105, no. 2, pp. 249–259, Feb. 2017, doi: 10.1002/jbm.b.33552.

[123] M. Namiri *et al.*, "Improving the biological function of decellularized heart valves through integration of protein tethering and three-dimensional cell seeding in a bioreactor," *J. Tissue Eng. Regen. Med.*, vol. 12, no. 4, pp. e1865–e1879, Apr. 2018, doi: 10.1002/term.2617.

[124] M. C. VeDepo, E. E. Buse, A. Paul, G. L. Converse, and R. A. Hopkins, "Non-physiologic Bioreactor Processing Conditions for Heart Valve Tissue Engineering," *Cardiovasc. Eng. Technol.*, vol. 10, no. 4, pp. 628–637, Dec. 2019, doi: 10.1007/s13239-019-00438-x.

[125] S. Parvin Nejad, M. C. Blaser, J. P. Santerre, C. A. Caldarone, and C. A. Simmons, "Biomechanical conditioning of tissue engineered heart valves: Too much of a good thing?," *Adv. Drug Deliv. Rev.*, vol. 96, pp. 161–175, 2016, doi: 10.1016/j.addr.2015.11.003.

[126] K. Hayashida, K. Kanda, H. Yaku, J. Ando, and Y. Nakayama, "Development of an in vivo tissue-engineered, autologous heart valve (the biovalve): Preparation of a prototype model," *J. Thorac. Cardiovasc. Surg.*, vol. 134, no. 1, pp. 152–159, 2007, doi: 10.1016/j.jtcvs.2007.01.087.

[127] M. Yamanami *et al.*, "Development of a Completely Autologous Valved Conduit With the Sinus of Valsalva Using In-Body Tissue Architecture Technology," *Circulation*, vol. 122,

no. 11_suppl_1, pp. 5–7, Sep. 2010, doi: 10.1161/CIRCULATIONAHA.109.922211.

[128] S. Kishimoto *et al.*, "Sutureless aortic valve replacement using a novel autologous tissue heart valve with stent (stent biovalve): proof of concept," *J. Artif. Organs*, vol. 18, no. 2, pp. 185–190, Jun. 2015, doi: 10.1007/s10047-015-0817-1.

[129] H. Sumikura, Y. Nakayama, K. Ohnuma, S. Kishimoto, Y. Takewa, and E. Tatsumi, "In vitro hydrodynamic evaluation of a biovalve with stent (tubular leaflet type) for transcatheter pulmonary valve implantation," *J. Artif. Organs*, vol. 18, no. 4, pp. 307–314, Dec. 2015, doi: 10.1007/s10047-015-0851-z.

[130] Y. Miyazaki *et al.*, "Acute performance of a novel restorative transcatheter aortic valve: preclinical results," *EuroIntervention*, vol. 13, no. 12, pp. e1410–e1417, Dec. 2017, doi: 10.4244/EIJ-D-17-00554.

[131] S. E. Motta *et al.*, "Development of an Off-the-Shelf Tissue-Engineered Sinus Valve for Transcatheter Pulmonary Valve Replacement: a Proof-of-Concept Study," *J. Cardiovasc. Transl. Res.*, vol. 11, no. 3, pp. 182–191, Jun. 2018, doi: 10.1007/s12265-018-9800-6.

[132] G. Bennink *et al.*, "A novel restorative pulmonary valved conduit in a chronic sheep model: Mid-term hemodynamic function and histologic assessment," *J. Thorac. Cardiovasc. Surg.*, vol. 155, no. 6, pp. 2591-2601.e3, 2018, doi: 10.1016/j.jtcvs.2017.12.046.

[133] M. Y. Emmert *et al.*, "Computational modeling guides tissue-engineered heart valve design for long-term in vivo performance in a translational sheep model," *Sci. Transl. Med.*, vol. 10, no. 440, p. eaan4587, May 2018, doi: 10.1126/scitranslmed.aan4587.

[134] V. Lintas *et al.*, "Development of a Novel Human Cell-Derived Tissue-Engineered Heart Valve for Transcatheter Aortic Valve Replacement: an In Vitro and In Vivo Feasibility Study," *J. Cardiovasc. Transl. Res.*, vol. 11, no. 6, pp. 470–482, Dec. 2018, doi: 10.1007/s12265-018-9821-1.

[135] S. E. Motta *et al.*, "Human cell-derived tissue-engineered heart valve with integrated Valsalva sinuses: towards native-like transcatheter pulmonary valve replacements," *npj Regen. Med.*, vol. 4, no. 1, p. 14, Jun. 2019, doi: 10.1038/s41536-019-0077-4.

[136] G. N. Coyan *et al.*, "In vivo functional assessment of a novel degradable metal and elastomeric scaffold-based tissue engineered heart valve," *J. Thorac. Cardiovasc. Surg.*, vol. 157, no. 5, pp. 1809–1816, 2019, doi: 10.1016/j.jtcvs.2018.09.128.

[137] G. N. Coyan *et al.*, "Acute In Vivo Functional Assessment of a Biodegradable Stentless Elastomeric Tricuspid Valve," *J. Cardiovasc. Transl. Res.*, vol. 13, no. 5, pp. 796–805, 2020, doi: 10.1007/s12265-020-09960-z.

[138] Z. H. Syedain *et al.*, "Pediatric tri-tube valved conduits made from fibroblast-produced extracellular matrix evaluated over 52 weeks in growing lambs," *Sci. Transl. Med.*, vol. 13, no. 585, pp. 1–16, 2021, doi: 10.1126/scitranslmed.abb7225.

[139] B. J. De Kort *et al.*, “Inflammatory and regenerative processes in bioresorbable synthetic pulmonary valves up to two years in sheep–Spatiotemporal insights augmented by Raman microspectroscopy,” *Acta Biomater.*, vol. 135, pp. 243–259, 2021, doi: 10.1016/j.actbio.2021.09.005.

[140] B. Weber *et al.*, “Off-the-shelf human decellularized tissue-engineered heart valves in a non-human primate model,” *Biomaterials*, vol. 34, no. 30, pp. 7269–7280, Oct. 2013, doi: 10.1016/j.biomaterials.2013.04.059.

[141] A. Driessen-Mol *et al.*, “Transcatheter Implantation of Homologous ‘Off-the-Shelf’ Tissue-Engineered Heart Valves With Self-Repair Capacity,” *J. Am. Coll. Cardiol.*, vol. 63, no. 13, pp. 1320–1329, Apr. 2014, doi: 10.1016/j.jacc.2013.09.082.

[142] Z. Syedain *et al.*, “6-Month aortic valve implantation of an off-the-shelf tissue-engineered valve in sheep,” *Biomaterials*, vol. 73, pp. 175–184, Dec. 2015, doi: 10.1016/j.biomaterials.2015.09.016.

[143] J. Reimer, Z. Syedain, B. Haynie, M. Lahti, J. Berry, and R. Tranquillo, “Implantation of a Tissue-Engineered Tubular Heart Valve in Growing Lambs,” *Ann. Biomed. Eng.*, vol. 45, no. 2, pp. 439–451, Feb. 2017, doi: 10.1007/s10439-016-1605-7.

[144] O. Soliman *et al.*, “Midterm performance of a novel restorative pulmonary valved conduit: preclinical results,” *EuroIntervention*, vol. 13, no. 12, pp. e1418–e1427, Dec. 2017, doi: 10.4244/EIJ-D-17-00553.

[145] B. Sanders *et al.*, “Improved Geometry of Decellularized Tissue Engineered Heart Valves to Prevent Leaflet Retraction,” *Ann. Biomed. Eng.*, vol. 44, no. 4, pp. 1061–1071, Apr. 2016, doi: 10.1007/s10439-015-1386-4.

[146] B. L. Zhang, R. W. Bianco, and F. J. Schoen, “Preclinical Assessment of Cardiac Valve Substitutes: Current Status and Considerations for Engineered Tissue Heart Valves,” *Front. Cardiovasc. Med.*, vol. 6, no. June, pp. 1–9, Jun. 2019, doi: 10.3389/fcvm.2019.00072.

[147] M. Uiterwijk, D. C. van der Valk, R. van Vliet, I. J. de Brouwer, C. R. Hooijmans, and J. Kluin, “Pulmonary valve tissue engineering strategies in large animal models,” *PLoS One*, vol. 16, no. 10, p. e0258046, Oct. 2021, doi: 10.1371/journal.pone.0258046.

[148] S. E. Ahlberg *et al.*, “Animal Models for Cardiac Valve Research,” in *Heart Valves*, 2nd ed., P. A. Iaizzo, M. Griselli, T. L. Iles, and J. D. St. Louis, Eds. Cham: Springer International Publishing, 2023, pp. 509–524.

[149] S. T. Rashid, H. J. Salacinski, G. Hamilton, and A. M. Seifalian, “The use of animal models in developing the discipline of cardiovascular tissue engineering: a review,” *Biomaterials*, vol. 25, no. 9, pp. 1627–1637, Apr. 2004, doi: 10.1016/S0142-9612(03)00522-2.

[150] P. J. Marascalco, S. P. Ritchie, T. A. Snyder, and M. V. Kameneva, “Development of standard tests to examine viscoelastic properties of blood of experimental animals for pediatric mechanical support device evaluation,” *ASAIO J.*, vol. 52, no. 5, pp. 567–574,

2006, doi: 10.1097/01.mat.0000242248.66083.48.

[151] J. M. Siller-Matula, R. Plasenzotti, A. Spiel, P. Quehenberger, and B. Jilma, “Interspecies differences in coagulation profile,” *Thromb. Haemost.*, vol. 100, no. 09, pp. 397–404, Nov. 2008, doi: 10.1160/TH08-02-0103.

[152] M. Y. Esmail and D. Lee-Parritz, “Animal Surgery and Care of Animals,” in *Biomaterials Science*, Fourth Ed., W. R. Wagner, S. E. Sakiyama-Elbert, G. Zhang, and M. J. Yaszemnski, Eds. Elsevier, 2020, pp. 899–915.

[153] A. Trantina-Yates, C. Weissenstein, P. Human, and P. Zilla, “Stentless bioprosthetic heart valve research: Sheep versus primate model,” *Ann. Thorac. Surg.*, vol. 71, no. 5 SUPPL., pp. 0–5, 2001, doi: 10.1016/S0003-4975(01)02502-4.

[154] G. Steinhoff *et al.*, “Tissue Engineering of Pulmonary Heart Valves on Allogenic Acellular Matrix Conduits,” *Circulation*, vol. 102, no. suppl_3, Nov. 2000, doi: 10.1161/circ.102.suppl_3.III-50.

[155] A. C. Biermann *et al.*, “Impact of T-cell-mediated immune response on xenogeneic heart valve transplantation: short-term success and mid-term failure,” *Eur. J. Cardio-Thoracic Surg.*, vol. 53, no. 4, pp. 784–792, Apr. 2018, doi: 10.1093/ejcts/ezx396.

[156] S. Dekker, D. van Geemen, A. J. van den Bogaerdt, A. Driessen-Mol, E. Aikawa, and A. I. P. M. Smits, “Sheep-Specific Immunohistochemical Panel for the Evaluation of Regenerative and Inflammatory Processes in Tissue-Engineered Heart Valves,” *Front. Cardiovasc. Med.*, vol. 5, no. August, pp. 1–19, Aug. 2018, doi: 10.3389/fcvm.2018.00105.

[157] P. Herijgers *et al.*, “Calcification characteristics of porcine stentless valves in juvenile sheep,” *Eur. J. Cardio-Thoracic Surg.*, vol. 15, no. 2, pp. 134–142, Feb. 1999, doi: 10.1016/S1010-7940(98)00313-3.

[158] S. Ozaki, P. Herijgers, and W. Flameng, “A new model to test the calcification characteristics of bioprosthetic heart valves.,” *Ann. Thorac. Cardiovasc. Surg.*, vol. 10, no. 1, pp. 23–8, Feb. 2004, [Online]. Available: http://www.ncbi.nlm.nih.gov/pubmed/15008695.

[159] M. F. Ogle, S. J. Kelly, R. W. Bianco, and R. J. Levy, “Calcification resistance with aluminum-ethanol treated porcine aortic valve bioprostheses in juvenile sheep,” *Ann. Thorac. Surg.*, vol. 75, no. 4, pp. 1267–1273, Apr. 2003, doi: 10.1016/S0003-4975(02)04489-2.

[160] M. C. V. B. Braile-Sternieri *et al.*, “In vivo evaluation of Vivere bovine pericardium valvular bioprosthesis with a new anti-calcifying treatment,” *Artif. Organs*, vol. 44, no. 11, pp. E482–E493, Nov. 2020, doi: 10.1111/aor.13718.

[161] E. Bodnar, “The Medtronic Parallel valve and the lessons learned.,” *J. Heart Valve Dis.*, vol. 5, no. 6, pp. 572–3, Nov. 1996, [Online]. Available: http://www.ncbi.nlm.nih.gov/pubmed/8953433.

[162] M. Gallo *et al.*, "The Vietnamese pig as a translational animal model to evaluate tissue engineered heart valves: promising early experience," *Int. J. Artif. Organs*, vol. 40, no. 4, pp. 142–149, 2017, doi: 10.5301/ijao.5000568.

[163] S. Numata, T. Fujisato, K. Niwaya, H. Ishibashi-Ueda, T. Nakatani, and S. Kitamura, "Immunological and histological evaluation of decellularized allograft in a pig model: Comparison with cryopreserved allograft," *J. Heart Valve Dis.*, vol. 13, no. 6, pp. 984–990, 2004.

[164] M. Griselli, R. K. Ameduri, and M. L. Rigby, "Congenital Heart Defects Which Include Cardiac Valve Abnormalities," in *Heart Valves*, 2nd ed., P. A. Iaizzo, M. Griselli, T. L. Iles, and J. D. St. Louis, Eds. Cham: Springer International Publishing, 2023, pp. 45–55.

[165] T. Z. Choudhury and V. Garg, "Molecular genetic mechanisms of congenital heart disease," *Curr. Opin. Genet. Dev.*, vol. 75, p. 101949, 2022, doi: 10.1016/j.gde.2022.101949.

[166] T. P. Graham, D. J. Driscoll, W. M. Gersony, J. W. Newburger, A. Rocchini, and J. A. Towbin, "Task Force 2: Congenital heart disease," *J. Am. Coll. Cardiol.*, vol. 45, no. 8, pp. 1326–1333, Apr. 2005, doi: 10.1016/j.jacc.2005.02.009.

[167] J. R. G. Etnel *et al.*, "Outcome after aortic valve replacement in children: A systematic review and meta-analysis," *J. Thorac. Cardiovasc. Surg.*, vol. 151, no. 1, pp. 143-152.e3, 2016, doi: 10.1016/j.jtcvs.2015.09.083.

[168] G. D. Hill, S. Ginde, R. Rios, P. C. Frommelt, and K. D. Hill, "Surgical Valvotomy Versus Balloon Valvuloplasty for Congenital Aortic Valve Stenosis: A Systematic Review and Meta-Analysis," *J. Am. Heart Assoc.*, vol. 5, no. 8, 2016, doi: 10.1161/JAHA.116.003931.

[169] V. Hraška *et al.*, "The Long-Term Outcome of Open Valvotomy for Critical Aortic Stenosis in Neonates," *Ann. Thorac. Surg.*, vol. 94, no. 5, pp. 1519–1526, Nov. 2012, doi: 10.1016/j.athoracsur.2012.03.056.

[170] J. Siddiqui *et al.*, "Surgical Valvotomy and Repair for Neonatal and Infant Congenital Aortic Stenosis Achieves Better Results Than Interventional Catheterization," *J. Am. Coll. Cardiol.*, vol. 62, no. 22, pp. 2134–2140, Dec. 2013, doi: 10.1016/j.jacc.2013.07.052.

[171] J. Pan, "Unicuspid Aortic Valve: A Rare Congenital Anomaly," *Cardiology*, vol. 147, no. 2, pp. 207–215, 2022, doi: 10.1159/000521623.

[172] J. A. A. E. Cuypers, M. Witsenburg, D. van der Linde, and J. W. Roos-Hesselink, "Pulmonary stenosis: update on diagnosis and therapeutic options," *Heart*, vol. 99, no. 5, pp. 339–347, Mar. 2013, doi: 10.1136/heartjnl-2012-301964.

[173] L. J. Schulte *et al.*, "Evolution of Pulmonary Valve Management During Repair of Tetralogy of Fallot: A 14-year Experience," *Ann. Thorac. Surg.*, vol. 115, no. 2, pp. 462–469, Feb. 2023, doi: 10.1016/j.athoracsur.2022.05.063.

[174] M. G. Earing, H. M. Connolly, J. A. Dearani, N. M. Ammash, M. Grogan, and C. A. Warnes,

"Long-term Follow-up of Patients After Surgical Treatment for Isolated Pulmonary Valve Stenosis," *Mayo Clin. Proc.*, vol. 80, no. 7, pp. 871–876, Jul. 2005, doi: 10.4065/80.7.871.

[175] A. Voet *et al.*, "Long-term outcome after treatment of isolated pulmonary valve stenosis," *Int. J. Cardiol.*, vol. 156, no. 1, pp. 11–15, Apr. 2012, doi: 10.1016/j.ijcard.2010.10.038.

[176] F. D. A. da Costa *et al.*, "Decellularized Versus Standard Pulmonary Allografts in the Ross Procedure: Propensity-Matched Analysis," *Ann. Thorac. Surg.*, vol. 105, no. 4, pp. 1205–1213, 2018, doi: 10.1016/j.athoracsur.2017.09.057.

[177] R. Henaine, F. Roubertie, M. Vergnat, and J. Ninet, "Valve replacement in children: A challenge for a whole life," *Arch. Cardiovasc. Dis.*, vol. 105, no. 10, pp. 517–528, Oct. 2012, doi: 10.1016/j.acvd.2012.02.013.

[178] J. P. da Silva *et al.*, "The cone reconstruction of the tricuspid valve in Ebstein's anomaly. The operation: early and midterm results," *J. Thorac. Cardiovasc. Surg.*, vol. 133, no. 1, pp. 215–223, Jan. 2007, doi: 10.1016/j.jtcvs.2006.09.018.

[179] A. E. Wood, D. G. Healy, L. Nolke, D. Duff, P. Oslizlok, and K. Walsh, "Mitral valve reconstruction in a pediatric population: Late clinical results and predictors of long-term outcome," *J. Thorac. Cardiovasc. Surg.*, vol. 130, no. 1, pp. 66–73, Jul. 2005, doi: 10.1016/j.jtcvs.2005.03.025.

[180] P. S. Naimo *et al.*, "Truncus arteriosus repair: A 40-year multicenter perspective," *J. Thorac. Cardiovasc. Surg.*, vol. 161, no. 1, pp. 230–240, Jan. 2021, doi: 10.1016/j.jtcvs.2020.04.149.

[181] S. A. Husain and J. W. Brown, "When Reconstruction Fails or is Not Feasible: Valve Replacement Options in the Pediatric Population," *Semin. Thorac. Cardiovasc. Surg. Pediatr. Card. Surg. Annu.*, vol. 10, no. 1, pp. 117–124, Jan. 2007, doi: 10.1053/j.pcsu.2007.01.012.

[182] Y. Xue *et al.*, "Age-related enhanced degeneration of bioprosthetic valves due to leaflet calcification, tissue crosslinking, and structural changes," *Cardiovasc. Res.*, vol. 119, no. 1, pp. 302–315, Mar. 2023, doi: 10.1093/cvr/cvac002.

[183] B. Alsoufi, "Aortic valve replacement in children: Options and outcomes," *J. Saudi Hear. Assoc.*, vol. 26, no. 1, pp. 33–41, Jan. 2014, doi: 10.1016/j.jsha.2013.11.003.

[184] L. J. Zühlke *et al.*, "Group A Streptococcus, Acute Rheumatic Fever and Rheumatic Heart Disease: Epidemiology and Clinical Considerations," *Curr. Treat. Options Cardiovasc. Med.*, vol. 19, no. 2, p. 15, Feb. 2017, doi: 10.1007/s11936-017-0513-y.

[185] L. Zühlke *et al.*, "Characteristics, complications, and gaps in evidence-based interventions in rheumatic heart disease: The Global Rheumatic Heart Disease Registry (the REMEDY study)," *Eur. Heart J.*, vol. 36, no. 18, pp. 1115–1122, 2015, doi: 10.1093/eurheartj/ehu449.

[186] B. Iung, "Global threat of rheumatic heart disease: do not forget children!," *Heart*, vol. 108,

no. 8, pp. 582–583, Apr. 2022, doi: 10.1136/heartjnl-2021-320673.

[187] P. Zilla, R. M. Bolman III, P. Boateng, and K. Sliwa, “A glimpse of hope: cardiac surgery in low- and middle-income countries (LMICs),” *Cardiovasc. Diagn. Ther.*, vol. 10, no. 2, pp. 336–349, Apr. 2020, doi: 10.21037/cdt.2019.11.03.

[188] M. Zimmerman *et al.*, “Clinical outcomes of children with rheumatic heart disease,” *Heart*, vol. 108, no. 8, pp. 633–638, Apr. 2022, doi: 10.1136/heartjnl-2021-320356.

[189] D. Vervoort, M. Ouzounian, and B. Yanagawa, “Mitral valve surgery for rheumatic heart disease: Replace, repair, retrain?,” *Curr. Opin. Cardiol.*, vol. 36, no. 2, pp. 179–185, 2021, doi: 10.1097/HCO.0000000000000826.

[190] G. A. Roth *et al.*, “Global Burden of Cardiovascular Diseases and Risk Factors, 1990-2019: Update From the GBD 2019 Study,” *J. Am. Coll. Cardiol.*, vol. 76, no. 25, pp. 2982–3021, 2020, doi: 10.1016/j.jacc.2020.11.010.

[191] D. Kehl, B. Weber, and S. P. Hoerstrup, “Bioengineered living cardiac and venous valve replacements: current status and future prospects,” *Cardiovasc. Pathol.*, vol. 25, no. 4, pp. 300–305, Jul. 2016, doi: 10.1016/j.carpath.2016.03.001.

[192] A. Mookhoek *et al.*, “Ross Procedure in Neonates and Infants: A European Multicenter Experience,” *Ann. Thorac. Surg.*, vol. 100, no. 6, pp. 2278–2284, Dec. 2015, doi: 10.1016/j.athoracsur.2015.08.008.

[193] J. W. Brown, P. M. Patel, J.-H. Ivy Lin, A. S. Habib, M. D. Rodefeld, and M. W. Turrentine, “Ross Versus Non-Ross Aortic Valve Replacement in Children: A 22-Year Single Institution Comparison of Outcomes,” *Ann. Thorac. Surg.*, vol. 101, no. 5, pp. 1804–1810, May 2016, doi: 10.1016/j.athoracsur.2015.12.076.

[194] V. Pergola *et al.*, “The long term results of the Ross procedure: The importance of candidate selection,” *Int. J. Cardiol.*, vol. 320, pp. 35–41, Dec. 2020, doi: 10.1016/j.ijcard.2020.07.009.

[195] S. Sarikouch *et al.*, “Decellularized fresh homografts for pulmonary valve replacement: a decade of clinical experience,” *Eur. J. Cardio-Thoracic Surg.*, vol. 50, no. 2, pp. 281–290, Aug. 2016, doi: 10.1093/ejcts/ezw050.

[196] F. D. A. da Costa *et al.*, “Decellularized Allografts for Right Ventricular Outflow Tract Reconstruction in Children,” *World J. Pediatr. Congenit. Hear. Surg.*, vol. 8, no. 5, pp. 605–612, Sep. 2017, doi: 10.1177/2150135117723916.

[197] L. Iop *et al.*, “Decellularized Allogeneic Heart Valves Demonstrate Self-Regeneration Potential after a Long-Term Preclinical Evaluation,” *PLoS One*, vol. 9, no. 6, p. e99593, Jun. 2014, doi: 10.1371/journal.pone.0099593.

[198] J. R. Paniagua Gutierrez *et al.*, “Regenerative Potential of Low-Concentration SDS-Decellularized Porcine Aortic Valved Conduits In Vivo,” *Tissue Eng. Part A*, vol. 21, no.

1–2, pp. 332–342, Jan. 2015, doi: 10.1089/ten.tea.2014.0003.

[199] I. Tudorache *et al.*, "Decellularized aortic allografts versus pulmonary autografts for aortic valve replacement in the growing sheep model: haemodynamic and morphological results at 20 months after implantation," *Eur. J. Cardio-Thoracic Surg.*, vol. 49, no. 4, pp. 1228–1238, Apr. 2016, doi: 10.1093/ejcts/ezv362.

[200] I. Voges *et al.*, "Adverse results of a decellularized tissue-engineered pulmonary valve in humans assessed with magnetic resonance imaging," *Eur. J. Cardio-Thoracic Surg.*, vol. 44, no. 4, pp. e272–e279, Oct. 2013, doi: 10.1093/ejcts/ezt328.

[201] Z. Prodan *et al.*, "Initial Clinical Trial of a Novel Pulmonary Valved Conduit," *Semin. Thorac. Cardiovasc. Surg.*, vol. 34, no. 3, pp. 985–991, 2022, doi: 10.1053/j.semtcvs.2021.03.036.

[202] D. L. Morales *et al.*, "A Novel Restorative Pulmonary Valve Conduit: Early Outcomes of Two Clinical Trials," *Front. Cardiovasc. Med.*, vol. 7, no. March, pp. 1–9, Mar. 2021, doi: 10.3389/fcvm.2020.583360.

[203] M. Ibrahim *et al.*, "A Novel Low-Profile Self-Expanding Biodegradable Percutaneous Heart Valve Frame That Grows with a Child," *Coatings*, vol. 13, no. 1, p. 184, Jan. 2023, doi: 10.3390/coatings13010184.

[204] P. Bonhoeffer *et al.*, "Percutaneous replacement of pulmonary valve in a right-ventricle to pulmonary-artery prosthetic conduit with valve dysfunction," *Lancet*, vol. 356, no. 9239, pp. 1403–1405, Oct. 2000, doi: 10.1016/S0140-6736(00)02844-0.

[205] S. M. Emani *et al.*, "Concept of an expandable cardiac valve for surgical implantation in infants and children," *J. Thorac. Cardiovasc. Surg.*, vol. 152, no. 6, pp. 1514–1523, Dec. 2016, doi: 10.1016/j.jtcvs.2016.08.040.

[206] F. Caldaroni, C. P. Brizard, and Y. D'Udekem, "Replacement of the Mitral Valve Under One Year of Age: Size Matters," *Semin. Thorac. Cardiovasc. Surg. Pediatr. Card. Surg. Annu.*, vol. 24, pp. 57–61, 2021, doi: 10.1053/j.pcsu.2021.03.006.

[207] "Draper Advances Growth-Adaptive Pediatric Heart Valve with Sutureless Adhesive," 2023. https://www.draper.com/press-release/draper-advances-growth-adaptive-pediatric-heart-valve-sutureless-adhesive-0 (accessed Aug. 08, 2023).

[208] M. S. Sacks and F. J. Schoen, "Collagen fiber disruption occurs independent of calcification in clinically explanted bioprosthetic heart valves," *J. Biomed. Mater. Res.*, vol. 62, no. 3, pp. 359–371, 2002, doi: 10.1002/jbm.10293.

[209] R. Zakerzadeh, M. C. Hsu, and M. S. Sacks, "Computational methods for the aortic heart valve and its replacements," *Expert Rev. Med. Devices*, vol. 14, no. 11, pp. 849–866, 2017, doi: 10.1080/17434440.2017.1389274.

[210] H. Jiang, G. Campbell, and R. Canas, "Leaflet geometry extraction and parametric

representation of a pericardial artificial heart valve," *Proc. Inst. Mech. Eng. Part H J. Eng. Med.*, vol. 219, no. 2, pp. 143–152, 2005, doi: 10.1243/095441105X9183.

[211] Y. Hong, J. Guan, K. L. Fujimoto, R. Hashizume, A. L. Pelinescu, and W. R. Wagner, "Tailoring the degradation kinetics of poly(ester carbonate urethane)urea thermoplastic elastomers for tissue engineering scaffolds," *Biomaterials*, vol. 31, no. 15, pp. 4249–4258, 2010, doi: 10.1016/j.biomaterials.2010.02.005.

[212] M. S. Sacks, "Biaxial mechanical evaluation of planar biological materials," *J. Elast.*, vol. 61, no. 1–3, pp. 199–246, 2000, doi: 10.1023/A:1010917028671.

[213] T. Courtney, M. S. Sacks, J. Stankus, J. Guan, and W. R. Wagner, "Design and analysis of tissue engineering scaffolds that mimic soft tissue mechanical anisotropy," *Biomaterials*, vol. 27, no. 19, pp. 3631–3638, 2006, doi: 10.1016/j.biomaterials.2006.02.024.

[214] J. P. Vande Geest, M. S. Sacks, and D. A. Vorp, "A planar biaxial constitutive relation for the luminal layer of intra-luminal thrombus in abdominal aortic aneurysms," *J. Biomech.*, vol. 39, no. 13, pp. 2347–2354, 2006, doi: 10.1016/j.jbiomech.2006.05.011.

[215] A. D'Amore, J. A. Stella, W. R. Wagner, and M. S. Sacks, "Characterization of the complete fiber network topology of planar fibrous tissues and scaffolds," *Biomaterials*, vol. 31, no. 20, pp. 5345–5354, 2010, doi: 10.1016/j.biomaterials.2010.03.052.

[216] Z. Zhang, "A flexible new technique for camera calibration," *IEEE Trans. Pattern Anal. Mach. Intell.*, vol. 22, no. 11, pp. 1330–1334, 2000, doi: 10.1109/34.888718.

[217] J. Heikkila and O. Silven, "A four-step camera calibration procedure with implicit image correction," in *Proceedings of IEEE Computer Society Conference on Computer Vision and Pattern Recognition*, 1997, pp. 1106–1112, doi: 10.1109/CVPR.1997.609468.

[218] N. J. Amoroso, A. D'Amore, Y. Hong, W. R. Wagner, and M. S. Sacks, "Elastomeric electrospun polyurethane scaffolds: The interrelationship between fabrication conditions, fiber topology, and mechanical properties," *Adv. Mater.*, vol. 23, no. 1, pp. 106–111, 2011, doi: 10.1002/adma.201003210.

[219] N. J. Amoroso, A. D'Amore, Y. Hong, C. P. Rivera, M. S. Sacks, and W. R. Wagner, "Microstructural manipulation of electrospun scaffolds for specific bending stiffness for heart valve tissue engineering," *Acta Biomater.*, vol. 8, no. 12, pp. 4268–4277, 2012, doi: 10.1016/j.actbio.2012.08.002.

[220] C. M. Hobson *et al.*, "Fabrication of elastomeric scaffolds with curvilinear fibrous structures for heart valve leaflet engineering," *J. Biomed. Mater. Res. - Part A*, vol. 103, no. 9, pp. 3101–3106, 2015, doi: 10.1002/jbm.a.35450.

[221] M. S. Sacks and C. J. Chuong, "Orthotropic mechanical properties of chemically treated bovine pericardium," *Ann. Biomed. Eng.*, vol. 26, no. 5, pp. 892–902, 1998, doi: 10.1114/1.135.

[222] T. Pham, F. Sulejmani, E. Shin, D. Wang, and W. Sun, "Quantification and comparison of the mechanical properties of four human cardiac valves," *Acta Biomater.*, vol. 54, pp. 345–355, 2017, doi: 10.1016/j.actbio.2017.03.026.

[223] H. Sugimoto and M. S. Sacks, "Effects of Leaflet Stiffness on In Vitro Dynamic Bioprosthetic Heart Valve Leaflet Shape," *Cardiovasc. Eng. Technol.*, vol. 4, no. 1, pp. 2–15, Mar. 2013, doi: 10.1007/s13239-013-0117-y.

[224] S. Morganti *et al.*, "Patient-specific isogeometric structural analysis of aortic valve closure," *Comput. Methods Appl. Mech. Eng.*, vol. 284, pp. 508–520, 2015, doi: 10.1016/j.cma.2014.10.010.

[225] F. Xu *et al.*, "A framework for designing patient-specific bioprosthetic heart valves using immersogeometric fluid–structure interaction analysis," *Int. j. numer. method. biomed. eng.*, vol. 34, no. 4, pp. 1–25, 2018, doi: 10.1002/cnm.2938.

[226] M. C. Hsu *et al.*, "Dynamic and fluid–structure interaction simulations of bioprosthetic heart valves using parametric design with T-splines and Fung-type material models," *Comput. Mech.*, vol. 55, no. 6, pp. 1211–1225, 2015, doi: 10.1007/s00466-015-1166-x.

[227] E. Kouhi and Y. S. Morsi, "A parametric study on mathematical formulation and geometrical construction of a stentless aortic heart valve," *J. Artif. Organs*, vol. 16, no. 4, pp. 425–442, 2013, doi: 10.1007/s10047-013-0719-z.

[228] K. Li and W. Sun, "Simulated transcatheter aortic valve deformation: A parametric study on the impact of leaflet geometry on valve peak stress," *Int. j. numer. method. biomed. eng.*, vol. 33, no. 3, pp. 1–14, 2017, doi: 10.1002/cnm.2814.

[229] S. K. Luketich *et al.*, "Engineering in-plane mechanics of electrospun polyurethane scaffolds for cardiovascular tissue applications," *J. Mech. Behav. Biomed. Mater.*, vol. 128, no. January, p. 105126, 2022, doi: 10.1016/j.jmbbm.2022.105126.

[230] J. H. Lee *et al.*, "Fluid–Structure Interaction Models of Bioprosthetic Heart Valve Dynamics in an Experimental Pulse Duplicator," *Ann. Biomed. Eng.*, vol. 48, no. 5, pp. 1475–1490, 2020, doi: 10.1007/s10439-020-02466-4.

[231] N. Saikrishnan, L. Mirabella, and A. P. Yoganathan, "Bicuspid aortic valves are associated with increased wall and turbulence shear stress levels compared to trileaflet aortic valves," *Biomech. Model. Mechanobiol.*, vol. 14, no. 3, pp. 577–588, 2015, doi: 10.1007/s10237-014-0623-3.

[232] A. Yousefi, D. L. Bark, and L. P. Dasi, "Effect of Arched Leaflets and Stent Profile on the Hemodynamics of Tri-Leaflet Flexible Polymeric Heart Valves," *Ann. Biomed. Eng.*, vol. 45, no. 2, pp. 464–475, 2017, doi: 10.1007/s10439-016-1674-7.

[233] M. Barakat, D. Dvir, and A. N. Azadani, "Fluid Dynamic Characterization of Transcatheter Aortic Valves Using Particle Image Velocimetry," *Artif. Organs*, vol. 42, no. 11, pp. E357–E368, 2018, doi: 10.1111/aor.13290.

[234] G. Zhu, Y. Wei, Q. Yuan, L. Cai, M. Nakao, and J. H. Yeo, “In vitro Assessment of the Impacts of Leaflet Design on the Hemodynamic Characteristics of ePTFE Pulmonary Prosthetic Valves,” *Front. Bioeng. Biotechnol.*, vol. 7, no. January, pp. 1–11, 2020, doi: 10.3389/fbioe.2019.00477.

[235] D. D. Pedersen, S. Kim, A. D’Amore, and W. R. Wagner, “Cardiac valve scaffold design: Implications of material properties and geometric configuration on performance and mechanics,” *J. Mech. Behav. Biomed. Mater.*, vol. 146, no. July, Jul. 2023, doi: 10.1016/j.jmbbm.2023.106043.

[236] W. Thielicke and E. J. Stamhuis, “PIVlab – Towards User-friendly, Affordable and Accurate Digital Particle Image Velocimetry in MATLAB,” *J. Open Res. Softw.*, vol. 2, 2014, doi: 10.5334/jors.bl.

[237] W. Thielicke and R. Sonntag, “Particle Image Velocimetry for MATLAB: Accuracy and enhanced algorithms in PIVlab,” *J. Open Res. Softw.*, vol. 9, pp. 1–14, 2021, doi: 10.5334/JORS.334.

[238] A. Tsuji *et al.*, “Intravascular hemolysis in aortic stenosis,” *Intern. Med.*, vol. 43, no. 10, pp. 935–938, 2004, doi: 10.2169/internalmedicine.43.935.

[239] K. Vahidkhah *et al.*, “Flow-Induced Damage to Blood Cells in Aortic Valve Stenosis,” *Ann. Biomed. Eng.*, vol. 44, no. 9, pp. 2724–2736, 2016, doi: 10.1007/s10439-016-1577-7.

[240] K. N. Morshed, D. Bark, M. Forleo, and L. P. Dasi, “Theory to predict shear stress on cells in turbulent blood flow,” *PLoS One*, vol. 9, no. 8, 2014, doi: 10.1371/journal.pone.0105357.

[241] C. S. Jhun *et al.*, “Determination of Reynolds shear stress level for hemolysis,” *ASAIO J.*, vol. 64, no. 1, pp. 63–69, 2017, doi: 10.1097/MAT.0000000000000615.

[242] C. Binter *et al.*, “Turbulent Kinetic Energy Assessed by Multipoint 4-Dimensional Flow Magnetic Resonance Imaging Provides Additional Information Relative to Echocardiography for the Determination of Aortic Stenosis Severity,” *Circ. Cardiovasc. Imaging*, vol. 10, no. 6, pp. 1–8, 2017, doi: 10.1161/CIRCIMAGING.116.005486.

[243] A. Hudani, J. A. White, S. C. Greenway, and J. Garcia, “Whole-Heart Assessment of Turbulent Kinetic Energy in the Repaired Tetralogy of Fallot,” *Appl. Sci.*, vol. 12, no. 21, 2022, doi: 10.3390/app122110946.

[244] J. D. Hellums, “1993 Whitaker lecture: Biorheology in thrombosis research,” *Ann. Biomed. Eng.*, vol. 22, no. 5, pp. 445–455, 1994, doi: 10.1007/BF02367081.

[245] V. O. Kheyfets *et al.*, “4D magnetic resonance flow imaging for estimating pulmonary vascular resistance in pulmonary hypertension,” *J. Magn. Reson. Imaging*, vol. 44, no. 4, pp. 914–922, Oct. 2016, doi: 10.1002/jmri.25251.

[246] A. Hudani *et al.*, “4D-Flow MRI Characterization of Pulmonary Flow in Repaired Tetralogy of Fallot,” *Appl. Sci.*, vol. 13, no. 5, 2023, doi: 10.3390/app13052810.

[247] N. Tsuchiya *et al.*, "Circulation derived from 4D flow MRI correlates with right ventricular dysfunction in patients with tetralogy of Fallot," *Sci. Rep.*, vol. 11, no. 1, pp. 1–12, 2021, doi: 10.1038/s41598-021-91125-2.

[248] M. Crago, D. S. Winlaw, S. Farajikhah, F. Dehghani, and S. Naficy, "Pediatric pulmonary valve replacements: Clinical challenges and emerging technologies," *Bioeng. Transl. Med.*, no. October 2022, pp. 1–21, 2023, doi: 10.1002/btm2.10501.

[249] J. L. R. Romeo *et al.*, "Outcome after surgical repair of tetralogy of Fallot: A systematic review and meta-analysis," *J. Thorac. Cardiovasc. Surg.*, vol. 159, no. 1, pp. 220-236.e8, Jan. 2020, doi: 10.1016/j.jtcvs.2019.08.127.

[250] D. Bobylev *et al.*, "5-Year results from the prospective European multi-centre study on decellularized homografts for pulmonary valve replacement ESPOIR Trial and ESPOIR Registry data," *Eur. J. Cardio-Thoracic Surg.*, vol. 62, no. 5, Oct. 2022, doi: 10.1093/ejcts/ezac219.

[251] A. K. Armstrong *et al.*, "Association between patient age at implant and outcomes after transcatheter pulmonary valve replacement in the multicenter Melody valve trials," *Catheter. Cardiovasc. Interv.*, vol. 94, no. 4, pp. 607–617, Oct. 2019, doi: 10.1002/ccd.28454.

[252] P. M. Patel, J. L. Herrmann, M. D. Rodefeld, M. W. Turrentine, and J. W. Brown, "Bovine jugular vein conduit versus pulmonary homograft in the Ross operation," *Cardiol. Young*, vol. 30, no. 3, pp. 323–327, Mar. 2020, doi: 10.1017/S1047951119003007.

[253] S. Loerakker, G. Argento, C. W. J. Oomens, and F. P. T. Baaijens, "Effects of valve geometry and tissue anisotropy on the radial stretch and coaptation area of tissue-engineered heart valves," *J. Biomech.*, vol. 46, no. 11, pp. 1792–1800, 2013, doi: 10.1016/j.jbiomech.2013.05.015.

[254] J. B. Carleton, G. J. Rodin, and M. S. Sacks, "Layered Elastomeric Fibrous Scaffolds: An In-Silico Study of the Achievable Range of Mechanical Behaviors," *ACS Biomater. Sci. Eng.*, vol. 3, no. 11, pp. 2907–2921, Nov. 2017, doi: 10.1021/acsbiomaterials.7b00308.

[255] G. Argento, M. Simonet, C. W. J. Oomens, and F. P. T. Baaijens, "Multi-scale mechanical characterization of scaffolds for heart valve tissue engineering," *J. Biomech.*, vol. 45, no. 16, pp. 2893–2898, Nov. 2012, doi: 10.1016/j.jbiomech.2012.07.037.

[256] A. D'Amore *et al.*, "From single fiber to macro-level mechanics: A structural finite-element model for elastomeric fibrous biomaterials," *J. Mech. Behav. Biomed. Mater.*, vol. 39, pp. 146–161, Nov. 2014, doi: 10.1016/j.jmbbm.2014.07.016.

[257] J. B. Carleton, A. D'Amore, K. R. Feaver, G. J. Rodin, and M. S. Sacks, "Geometric characterization and simulation of planar layered elastomeric fibrous biomaterials," *Acta Biomater.*, vol. 12, no. 1, pp. 93–101, Jan. 2015, doi: 10.1016/j.actbio.2014.09.049.

[258] A. D'Amore *et al.*, "Meso-scale topological cues influence extracellular matrix production

in a large deformation, elastomeric scaffold model," *Soft Matter*, vol. 14, no. 42, pp. 8483–8495, 2018, doi: 10.1039/C8SM01352G.

[259] S. Domaschke, M. Zündel, E. Mazza, and A. E. Ehret, "A 3D computational model of electrospun networks and its application to inform a reduced modelling approach," *Int. J. Solids Struct.*, vol. 158, pp. 76–89, Feb. 2019, doi: 10.1016/j.ijsolstr.2018.08.030.

[260] D. E. Caballero, F. Montini-Ballarin, J. M. Gimenez, and S. A. Urquiza, "Multiscale constitutive model with progressive recruitment for nanofibrous scaffolds," *J. Mech. Behav. Biomed. Mater.*, vol. 98, no. June, pp. 225–234, Oct. 2019, doi: 10.1016/j.jmbbm.2019.06.017.

[261] S. Domaschke *et al.*, "Predicting the macroscopic response of electrospun membranes based on microstructure and single fibre properties," *J. Mech. Behav. Biomed. Mater.*, vol. 104, no. July 2019, p. 103634, Apr. 2020, doi: 10.1016/j.jmbbm.2020.103634.

[262] D. E. Caballero *et al.*, "Reduced kinematic multiscale model for tissue engineering electrospun scaffolds," *Mech. Mater.*, vol. 166, no. January, p. 104214, Mar. 2022, doi: 10.1016/j.mechmat.2022.104214.

[263] E. A. Sander, T. Stylianopoulos, R. T. Tranquillo, and V. H. Barocas, "Image-based multiscale modeling predicts tissue-level and network-level fiber reorganization in stretched cell-compacted collagen gels," *Proc. Natl. Acad. Sci.*, vol. 106, no. 42, pp. 17675–17680, Oct. 2009, doi: 10.1073/pnas.0903716106.

[264] A. D'Amore, S. K. Luketich, R. Hoff, S. H. Ye, and W. R. Wagner, "Blending Polymer Labile Elements at Differing Scales to Affect Degradation Profiles in Heart Valve Scaffolds," *Biomacromolecules*, vol. 20, no. 7, pp. 2494–2505, 2019, doi: 10.1021/acs.biomac.9b00189.

[265] J. M. Szafron *et al.*, "Immuno-driven and Mechano-mediated Neotissue Formation in Tissue Engineered Vascular Grafts," *Ann. Biomed. Eng.*, vol. 46, no. 11, pp. 1938–1950, Nov. 2018, doi: 10.1007/s10439-018-2086-7.

[266] J. M. Szafron, A. B. Ramachandra, C. K. Breuer, A. L. Marsden, and J. D. Humphrey, "Optimization of Tissue-Engineered Vascular Graft Design Using Computational Modeling," *Tissue Eng. Part C Methods*, vol. 25, no. 10, pp. 561–570, Oct. 2019, doi: 10.1089/ten.tec.2019.0086.

[267] G. M. Bernacca, B. O'Connor, D. F. Williams, and D. J. Wheatley, "Hydrodynamic function of polyurethane prosthetic heart valves: influences of Young's modulus and leaflet thickness," *Biomaterials*, vol. 23, no. 1, pp. 45–50, Jan. 2002, doi: 10.1016/S0142-9612(01)00077-1.

[268] M. A. J. van Kelle, P. J. A. Oomen, W. J. T. Janssen-van den Broek, R. G. P. Lopata, S. Loerakker, and C. V. C. Bouten, "Initial scaffold thickness affects the emergence of a geometrical and mechanical equilibrium in engineered cardiovascular tissues," *J. R. Soc. Interface*, vol. 15, no. 148, p. 20180359, Nov. 2018, doi: 10.1098/rsif.2018.0359.

[269] T. E. Claiborne, J. Sheriff, M. Kuetting, U. Steinseifer, M. J. Slepian, and D. Bluestein, “In Vitro Evaluation of a Novel Hemodynamically Optimized Trileaflet Polymeric Prosthetic Heart Valve,” *J. Biomech. Eng.*, vol. 135, no. 2, pp. 1–8, Feb. 2013, doi: 10.1115/1.4023235.

[270] J. A. Stella, W. R. Wagner, and M. S. Sacks, “Scale-dependent fiber kinematics of elastomeric electrospun scaffolds for soft tissue engineering,” *J. Biomed. Mater. Res. Part A*, vol. 9999A, no. 3, p. NA-NA, 2009, doi: 10.1002/jbm.a.32593.

[271] P. Mela and A. D’Amore, “In Situ Heart Valve Tissue Engineering,” *JACC Basic to Transl. Sci.*, vol. 5, no. 12, pp. 1207–1209, Dec. 2020, doi: 10.1016/j.jacbts.2020.11.009.

[272] P. Thayer *et al.*, “The effects of combined cyclic stretch and pressure on the aortic valve interstitial cell phenotype,” *Ann. Biomed. Eng.*, vol. 39, no. 6, pp. 1654–1667, 2011, doi: 10.1007/s10439-011-0273-x.

[273] J. E. McBane, L. A. Matheson, S. Sharifpoor, J. P. Santerre, and R. S. Labow, “Effect of polyurethane chemistry and protein coating on monocyte differentiation towards a wound healing phenotype macrophage,” *Biomaterials*, vol. 30, no. 29, pp. 5497–5504, Oct. 2009, doi: 10.1016/j.biomaterials.2009.07.010.

[274] K. G. Battiston, R. S. Labow, C. A. Simmons, and J. P. Santerre, “Immunomodulatory polymeric scaffold enhances extracellular matrix production in cell co-cultures under dynamic mechanical stimulation,” *Acta Biomater.*, vol. 24, pp. 74–86, Sep. 2015, doi: 10.1016/j.actbio.2015.05.038.

[275] H. Krynauw *et al.*, “Tissue Ingrowth Markedly Reduces Mechanical Anisotropy and Stiffness in Fibre Direction of Highly Aligned Electrospun Polyurethane Scaffolds,” *Cardiovasc. Eng. Technol.*, vol. 11, no. 4, pp. 456–468, Aug. 2020, doi: 10.1007/s13239-020-00475-x.

[276] K. Takanari *et al.*, “Abdominal wall reconstruction by a regionally distinct biocomposite of extracellular matrix digest and a biodegradable elastomer,” *J. Tissue Eng. Regen. Med.*, vol. 10, no. 9, pp. 748–761, Sep. 2016, doi: 10.1002/term.1834.

[277] K. Takanari *et al.*, “Skeletal muscle derived stem cells microintegrated into a biodegradable elastomer for reconstruction of the abdominal wall,” *Biomaterials*, vol. 113, pp. 31–41, Jan. 2017, doi: 10.1016/j.biomaterials.2016.10.029.

[278] N. Poulis, M. Martin, S. P. Hoerstrup, M. Y. Emmert, and E. S. Fioretta, “Macrophage-extracellular matrix interactions: Perspectives for tissue engineered heart valve remodeling.,” *Front. Cardiovasc. Med.*, vol. 9, no. September, p. 952178, 2022, doi: 10.3389/fcvm.2022.952178.

[279] H. N. SABBAH, M. S. HAMID, and P. D. STEIN, “Mechanical Factors in the Degeneration of Porcine Bioprosthetic Valves: An Overview,” *J. Card. Surg.*, vol. 4, no. 4, pp. 302–309, Dec. 1989, doi: 10.1111/j.1540-8191.1989.tb00294.x.

[280] D. P. Howsmon and M. S. Sacks, “On Valve Interstitial Cell Signaling: The Link Between Multiscale Mechanics and Mechanobiology.,” *Cardiovasc. Eng. Technol.*, vol. 12, no. 1, pp. 15–27, Feb. 2021, doi: 10.1007/s13239-020-00509-4.

[281] Y. Jiang *et al.*, “Micromechanical force promotes aortic valvular calcification.,” *J. Thorac. Cardiovasc. Surg.*, vol. 164, no. 6, pp. e313–e329, Dec. 2022, doi: 10.1016/j.jtcvs.2021.08.014.

[282] G. Li, W. Qiao, W. Zhang, F. Li, J. Shi, and N. Dong, “The shift of macrophages toward M1 phenotype promotes aortic valvular calcification,” *J. Thorac. Cardiovasc. Surg.*, vol. 153, no. 6, pp. 1318-1327.e1, Jun. 2017, doi: 10.1016/j.jtcvs.2017.01.052.

[283] H. Z. E. Greenberg, G. Zhao, A. M. Shah, and M. Zhang, “Role of oxidative stress in calcific aortic valve disease and its therapeutic implications,” *Cardiovasc. Res.*, vol. 118, no. 6, pp. 1433–1451, May 2022, doi: 10.1093/cvr/cvab142.

[284] L. Shu, Z. Yuan, F. Li, and Z. Cai, “Oxidative stress and valvular endothelial cells in aortic valve calcification,” *Biomed. Pharmacother.*, vol. 163, no. April, p. 114775, Jul. 2023, doi: 10.1016/j.biopha.2023.114775.

[285] P. A. Shiekh, A. Singh, and A. Kumar, “Engineering Bioinspired Antioxidant Materials Promoting Cardiomyocyte Functionality and Maturation for Tissue Engineering Application,” *ACS Appl. Mater. Interfaces*, vol. 10, no. 4, pp. 3260–3273, 2018, doi: 10.1021/acsami.7b14777.

[286] P. A. Shiekh, A. Singh, and A. Kumar, “Exosome laden oxygen releasing antioxidant and antibacterial cryogel wound dressing OxOBand alleviate diabetic and infectious wound healing,” *Biomaterials*, vol. 249, no. January, p. 120020, 2020, doi: 10.1016/j.biomaterials.2020.120020.

[287] A. Singh, P. A. Shiekh, I. Qayoom, E. Srivastava, and A. Kumar, “Evaluation of polymeric aligned NGCs and exosomes in nerve injury models in diabetic peripheral neuropathy condition,” *Eur. Polym. J.*, vol. 146, no. December 2020, p. 110256, Mar. 2021, doi: 10.1016/j.eurpolymj.2020.110256.

[288] J. R. Martin *et al.*, “A porous tissue engineering scaffold selectively degraded by cell-generated reactive oxygen species,” *Biomaterials*, vol. 35, no. 12, pp. 3766–3776, Apr. 2014, doi: 10.1016/j.biomaterials.2014.01.026.

[289] M. A. P. McGough *et al.*, “Poly(Thioketal Urethane) Autograft Extenders in an Intertransverse Process Model of Bone Formation,” *Tissue Eng. - Part A*, vol. 25, no. 13–14, pp. 949–963, 2019, doi: 10.1089/ten.tea.2018.0223.

[290] M. A. P. McGough *et al.*, “Nanocrystalline Hydroxyapatite–Poly(thioketal urethane) Nanocomposites Stimulate a Combined Intramembranous and Endochondral Ossification Response in Rabbits,” *ACS Biomater. Sci. Eng.*, vol. 6, no. 1, pp. 564–574, Jan. 2020, doi: 10.1021/acsbiomaterials.9b01378.

[291] B. Rahmani *et al.*, "In Vitro Hydrodynamic Assessment of a New Transcatheter Heart Valve Concept (the TRISKELE)," *J. Cardiovasc. Transl. Res.*, vol. 10, no. 2, pp. 104–115, Apr. 2017, doi: 10.1007/s12265-016-9722-0.

[292] S. H. Im, Y. Jung, and S. H. Kim, "Current status and future direction of biodegradable metallic and polymeric vascular scaffolds for next-generation stents," *Acta Biomater.*, vol. 60, pp. 3–22, Sep. 2017, doi: 10.1016/j.actbio.2017.07.019.

[293] N. Sezer, Z. Evis, S. M. Kayhan, A. Tahmasebifar, and M. Koç, "Review of magnesium-based biomaterials and their applications," *J. Magnes. Alloy.*, vol. 6, no. 1, pp. 23–43, Mar. 2018, doi: 10.1016/j.jma.2018.02.003.

[294] K. Kumar, R. S. Gill, and U. Batra, "Challenges and opportunities for biodegradable magnesium alloy implants," *Mater. Technol.*, vol. 33, no. 2, pp. 153–172, Jan. 2018, doi: 10.1080/10667857.2017.1377973.